CHARACTERIZING MOUSE V1 OPTOGENETIC-MEDIATED REBOUND EFFECTS

by

Jared T. Shapiro

Submitted in partial fulfilment of the requirements
for the degree of Master of Science.

at

Dalhousie University
Halifax, Nova Scotia
August 2023

Dalhousie University is located in Mi'kma'ki, the
ancestral and unceded territory of the Mi'kmaq.
We are all Treaty people.

TABLE OF CONTENTS

LIST OF TABLES

LIST OF FIGURES

ABSTRACT

Cortical circuits comprise excitatory pyramidal (Pyr) cells and inhibitory interneurons that work together to perform neural computations. Optogenetic studies in mouse primary visual cortex (V1) have focused on (i) sketching the connectivity between Pyr cells and distinct interneuron subtypes that express parvalbumin (Pvalb+), somatostatin (SOM+) and vasoactive intestinal peptide (VIP+), and (ii) examining how photostimulating these inhibitory interneuron subtypes shape Pyr cell receptive field properties. Rebound effects have been reported after the optogenetic light source is turned off, but no systematic analysis of rebounds has been performed. Here, we sought to characterize optogenetic-mediated rebound effects and investigate whether network features like V1 activity and connectivity can affect rebound magnitude. We found converging evidence that coupling interneuron photostimulation with visual stimuli producing the strongest V1 responses also produced stronger rebound effects that were more prevalent across Pyr cell and interneuron populations. Importantly, Pyr cell and interneuron rebound effects differed in directionality and timing. We also report rebound effects were strongest and most prevalent when we coupled visual stimuli with Pvalb+ photostimulation rather than activating SOM+ or VIP+ interneurons. Overall, these results provide insight on experimental paradigms most conducive for producing optogenetic-mediated rebound effects in mouse V1, including coupling strong bottom-up visual stimulation with optogenetic activation of Pvalb+ cells in this circuit.

LIST OF ABREVIATIONS AND SYMBOLS USED

ACh	Acetylcholine.
Arch	Archaerhodopsin.
cGMP	Cyclic guanosine monophosphate.
ChR2	Channelrhodopsin-2.
CRF	Contrast response function.
E-I	Excitatory-inhibitory.
EPSP	Excitatory post-synaptic potential.
GABA	γ-Aminobutyric acid.
Glute	Gluteamatergic.
GTP	Guanosine triphosphate.
HCN	Hyperpolarization-activated cyclic nucleotide-gated channel.
Hi	High.
I_h	Hyperpolarization-activated.
IPSP	Inhibitory post-synaptic potential.
ISN	Inhibition stabilized network.
LGN	Lateral geniculate nucleus.
Lo	Low.
Neg-	Negative.
NpHR	Halorhodopsin.
PDE	phosphodiesterase.
PIR	Post-inhibitory rebound.
Pvalb+	Parvalbumin-expressing.
Pyr	Pyramidal cell.
RF	Receptive field.
RGC	Retinal ganglion cell.
SDF	Spike density function.
SOM+	Somatostatin-expressing.
TC	Thalamocortical.
VIP+	Vasoactive intestinal peptide-expressing.
V1	Primary visual cortex.

ACKNOWLEDGEMENTS

I want to acknowledge all the amazing people in my life that helped me along the way of my journey during my masters. First, my parents Garry Shapiro and Sun Young Yoon, siblings Shawn, Evan, Kate, Hartley, and their partners Tsun, Shawna Shapiro, Haley, Heather for always supporting me even when they did not fully understand my journey. Second, my amazing friends in Halifax and Toronto including Gloria, Niva, Alex, Robbie, Melissa, Matt, Kasey, Peter, James, Norris, Scott, Bri, Elise, Mike, Nicole and so many more for making these past several years more enjoyable and lessening my discomfort. Third, Shawna Shapiro's family including Cam, Ardith, Peter, and Ashley MacDonald, who were my Nova Scotian family while doing my honors thesis and master's degree, including during the COVID-19 pandemic. Fourth, my incredibly supportive partner Shawna Smith who has always supported and believed in me. Fifth, my supervisor Nathan Crowder, and key figures in the Psychology and Neuroscience department like Shelley Adamo who were incredibly understanding of my personal struggles during the COVID-19 pandemic and encouraged me to take a leave of absence from my master's degree to restore my mental health. Sixth, to Shelley Adamo, Bill Baldridge, and Tamara Franklin for being part of my defense on short notice. Seventh, all my past and current lab mates who contributed to my research, including Nicole, Jill, Cheryl, Alexander, Emily. Finally, Nathan Crowder for supervising both my honors and master's projects – without you this research would not be possible.

I appreciate you all,

Jared T. Shapiro

1. CHAPTER 1: INTRODUCTION

Chapter 1 will summarize neuroscience theory and relevant literature to prepare readers for the data presented in manuscript-formatted chapter 2 data. First, a summary of the visual system will outline what is known about the geniculo-striate pathway based on primate data using classical methods (Section 1.1). Second, a description of cortical circuits will explain how these networks function and the neurons that comprise them (Section 1.2). Third, a description of transgenic mice and optogenetic tools used in this animal model (Section 1.3) will prime readers for a literature review on optogenetic work in mouse V1 (section 1.4). Finally, a literature review will outline past research investigating rebound effects in non-optogenetic and optogenetic studies (section 1.5).

1.1 The Geniculo-Striate Pathway

The geniculo-striate pathway is the stream of the visual system that spans the retina, lateral geniculate nucleus (LGN) of the visual thalamus, to primary visual cortex (V1). Section 1.1 will cover the anatomy and physiology of this pathway based on primate data to describe the first steps in visual processing.

1.1.1 The Retina

1.1.1.1 Retinal Circuitry

Vision starts in the eye wherein light enters the pupil and is focused by the lens and cornea onto photosensitive neural tissue called the retina. The retina contains photoreceptors that express light-activated opsin proteins, which use photons of light to initiate a cascade of cellular events leading to altered neurotransmission of glutamate (Glute). During dark conditions, opsin proteins are bound with an inactive 11-cis-retinal that allows nearby Na^+ channels to remain open, leading to depolarization of the cell via Na^+ influx and continual release of Glute [1]. However, in light conditions opsin proteins absorb photons resulting in 11-cis-retinal to be photoisomerized to all-trans-retinal, which detaches and through a cascade of cellular events leads to metabolization of cyclic

guanosine monophosphate (cGMP), closing of cGMP-gated Na^+ channels, and decreased release of Glute [1]. Photoreceptors can be subdivided into cones and rods. There are three main types of cones that are each sensitive to peak short, medium, and long wavelengths of light [1] that mediate high acuity colour eyesight known as photopic vision [2,3]. Conversely, rods are used for low light conditions and mediate scotopic vision [2,4]. The center of the retina called the fovea is almost entirely made of cones, whereas peripheral regions of the retina are more dominated by rods [5]. Cones and rods both form parallel pathways within retinal circuits that use several intermediate cell-types to process their signal [6].

Light information coded by photoreceptors is further processed within retinal circuits, starting with bipolar cells. When photoreceptors are illuminated thereby decreasing neurotransmission, decreased glutamate in the synaptic cleft depolarizes on-bipolar cells with their sign-inverting synapses using metabotropic glutamate receptor 6 (mGluR6), but rather hyperpolarizes off-bipolar cells with their sign-conserving synapses using ionotropic receptors [7]. Next, bipolar activity is modulated by the lateral connections of horizontal and amacrine cells. Horizontal cells generate lateral inhibition in the network, whereby once activated by photoreceptors themselves they provide subsequent non-recurrent GABAergic input to neighbouring bipolar cell dendrites [8–10]. Conversely, Amacrine cells provide their input to bipolar cell axonal terminals, and in rod pathways AII Amacrine cells project rod-bipolar cell signals to cone-bipolar cells for later activation of retinal relay neurons [11,12]. Cone-bipolar cells ultimately transmit light information from both rod- and cone-pathways to retinal ganglion cells (RGCs), which form the optic nerve and provide afferent input to visual areas of the thalamus [6].

1.1.1.2 RGC Receptive Field (RF)

RGC activity is driven by their receptive field (RF), the area in visual space that when stimulated with a stimulus elicits a response from these neurons measured in spikes. Seminal research showed the RFs of RGCs are somewhat circular with an antagonistic centre-surround configuration [13]. In such RFs, the centre is either 'on' or 'off' depending on whether it is stimulated by a luminance increment or decrement, respectively (Figure 1a). Conversely, the surrounding region of centre is antagonistic, so on-centres are encircled by off-surround and off-centres are encircled by on-surround (Figure 1a). The formation of the centre-surround RF is driven by the underlying retinal circuits that connect to RGCs; the RF centre is driven by on- or off-bipolar cells, and lateral inhibition derived from horizonal cells is needed for forming the RFs antagonistic surround [6]. RGCs can be selective for visual stimuli features, preferentially responding to specific spatial frequencies and contrast levels [14]. There are many RGC sub-types that exhibit varying response properties [15–17], but the most prevalent are midget and parasol cells. Midget cells are smaller, less contrast sensitive, and exhibit colour-opponent RFs, compared to the achromatic parasol cells [18–20]. Each RGC samples visual information from a small region of visual space within its RF, neighbouring RGCs exhibit adjacent RFs, and all RGCs form RF mosaics to gather information within an organism's visual field (Figure 1b)[15]. These RGCs amongst other sub-types form the initial stages of parallel processing pathways for vision [21].

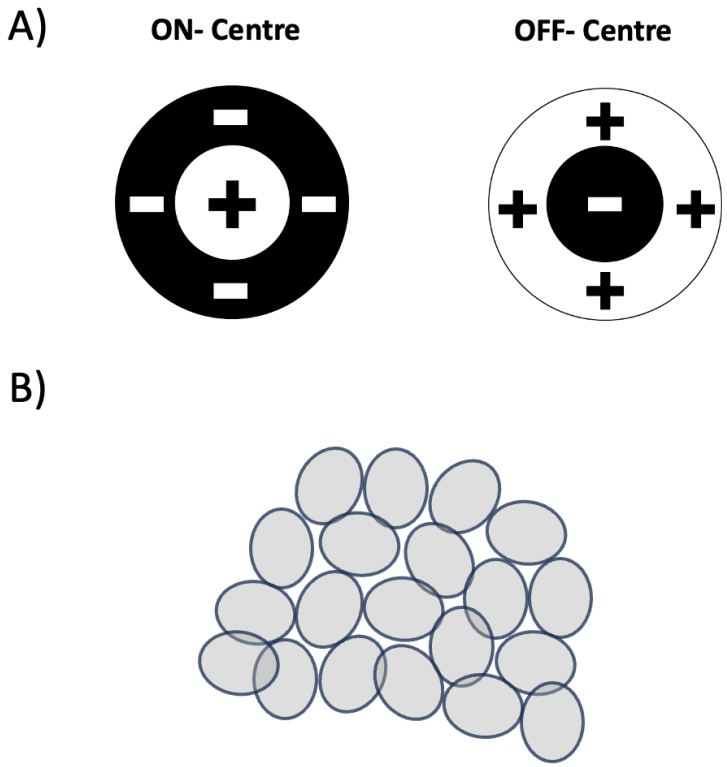

Figure 1: RGC RF formation.

(A) Spatial configuration of On- and Off-centre RGC RFs. Plus (+) signs indicate areas of the RF that are activated by a luminance increment, whereas minus (-) signs indicate areas of the RF that are activated by a luminance decrement. (B) Many neighboring neurons that exhibit adjacent RFs form RF mosaics, gathering information from a broad area in visual space. Grey Ovals indicate a single RF.

1.1.2 The Lateral Geniculate Nucleus (LGN)

The primary target of RGC axons is Thalamocortical (TC) neurons in the LGN. The LGN's main role is to relay light information from the retina to V1, however it also receives feedback from thalamic nuclei (e.g., reticular, pulvinar) and layer 6 of V1 [1,22]. The primate LGN contains 6 distinct layers, arranged into magnocellular and parvocellular laminae that are highly anatomically organized. In general, magnocellular laminae (layers 1-2) contain physically larger TC neurons and receive afferent input from parasol RGCs, whereas parvocellular laminae (layers 3-6) contain physically smaller TC neurons and receive afferent input from midget RGCs [1]. The RF properties of TC neurons in magnocellular and parvocellular laminae match properties of pre-synaptic parasol and midget RGCs, respectively [23–25]. LGN laminae are also divided by intermediate koniocellular layers that receive afferent input from small bistratified RGCs, however the function of these layers is more mysterious [1]. Each LGN layer only receives monocular inputs and RGC axons are organized into specific layers based on where they originate in the retina; LGN layers 2,3,5 receive input from axons originating in the ipsilateral eye, whereas layers 1,4,6 receive input from axons originating in the contralateral eye [1]. The LGN is also retinotopically organized, with neighbouring RGCs in the retina providing synaptic input to neighbouring cells in the LGN [26] and each segment of the visual field being represented in distinct regions of the LGN [27].

1.1.3 The Visual Cortex (V1)

1.1.3.1 V1 Laminar Organization

TC neurons originating in the LGN project their axons to V1, the first cortical region for visual processing. Neighbouring TC neurons in the LGN provide synaptic input to neighbouring V1 neurons, upholding retinotopic organization [28]. V1 contains 6 layers arranged vertically (Figure 2), with layer 4 being the principal recipient layer for TC axons [29,30]. However, layer 4 can be sub-divided based on where TC input originated from in the LGN. TC axons projecting from parvocellular laminae target V1 layer 4Cβ and the upper region of layer 6; TC axons projecting from magnocellular laminae target V1 layer 4Cα and the lower region of layer 6; TC axons projecting from koniocellular inter-laminae target layer 4A and superficial regions (Figure 2)[31]. V1 neurons in layers 4Cα and 4Cβ then project their axons to superficial and deeper layers [29,30] for propagating visual information and amplifying this signal within V1. Lastly, V1 neurons in layers 5-6 provide feedback to subcortical regions like the thalamus, whereas V1 neurons in superficial layers project their axons to higher order visual cortices [17,31].

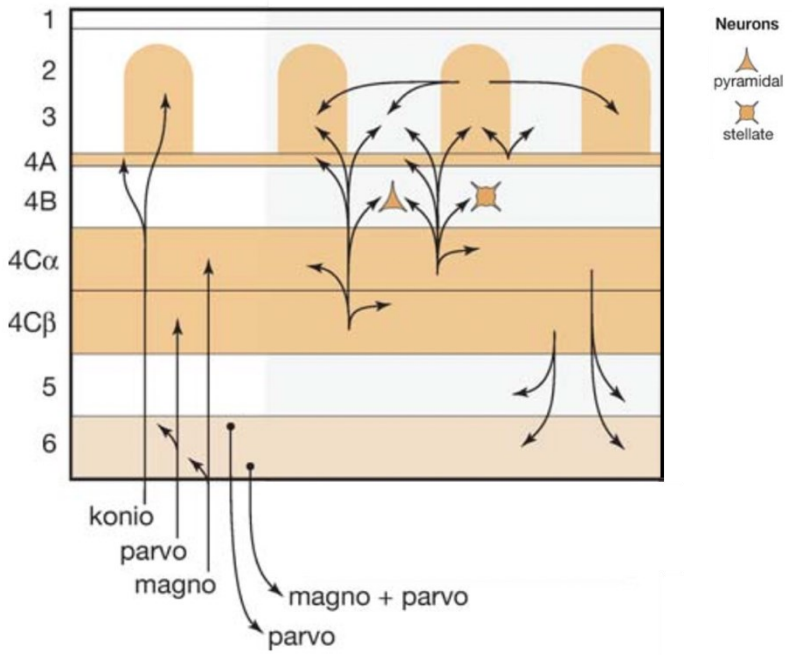

Figure 2: Laminar organization of V1 (Adapted from Sincich & Horton, 2005 [ref. 31]).

V1 is divided into 6 layers, with layer 4 being sub-divided into 4A, 4B, 4Cα and 4Cβ. In general, layer 4 is the principal recipient layer for TC axons, superficial layers provide cortico-cortical input, and deeper layers provide feedback to subcortical regions [17,29–31]. As afferent input from the LGN stimulates V1, recipient neurons in layer 4 provide intracortical connections to superficial and deeper V1 neurons to amplify cortical signals.

1.1.3.2 Orientation Selectivity

Nobel laureates Hubel and Wiesel demonstrated V1 neurons can be orientation tuned, meaning they preferentially respond when visual stimuli with elongated contours of a specific orientation are presented within their RF (Figure 3a-b)[32–34]. Hubel and Wiesel measured cat V1 neuron spiking with extracellular recordings while stimulating and mapping the neurons' RF with bars of light. Visual neuroscientists now use sinusoidal grating stimuli varying in orientation to stimulate V1 neurons for recording its spikes to each orientation (Figure 3a). Afterwards, the cell's firing rate can be calculated in spikes per second to make orientation tuning curves, which creates a function displaying its response selectivity across orientations (Figure 3b). V1 neuron RFs are approximately circular like the RFs of RGCs and TC neurons but can uniquely exhibit elongated On or Off subfields (Figure 3c). V1 neurons are classified as either simple (Figure 3c) or complex cells (Figure 3d) based on the presence of these subfields. Both simple and complex cells respond to bars of light in a particular orientation and are sometimes selective for direction of motion too (Figure 3a)[32–34], but simple cell RFs contain distinct 'on' and 'off' subfields and use these regions to encode stimulus luminance linearly from being stimulated with the light and dark sections of sinusoidal gratings (described in section *1.1.3.3*) in a wave-like pattern (Figure 3c)[35]. Conversely, complex cells do not contain distinct 'on' and 'off' subfields and do not produce a linear response to sinusoidal gratings (Figure 3d)[36]. V1 neurons are organized into iso-orientation domains wherein neurons selective for the same orientation are clustered together into a single domain of cortical space, and all domains converge onto a pinwheel center where neighbouring neurons prefer different orientations and have slightly broader tuning (Figure 3e)[37,38] . Remarkably, orientation selectivity is a computational operation potentially arising within V1. LGN neurons are poorly tuned to stimulus orientation [39] and so various models have aimed to explain how untuned TC inputs are transformed in the cortex. Feedforward models posit that input from various adjacent TC neurons converge onto single V1 neurons to construct their elongated RFs that detect orientation (Figure 3f black axons)[40]. Alternatively, lateral inhibition models suggest inhibitory cells in V1 that are either broadly tuned for orientation [41] or tuned to various orientations converge onto single V1 neurons for sharpening their orientation tuning (Figure 3f red axons)[40,42].

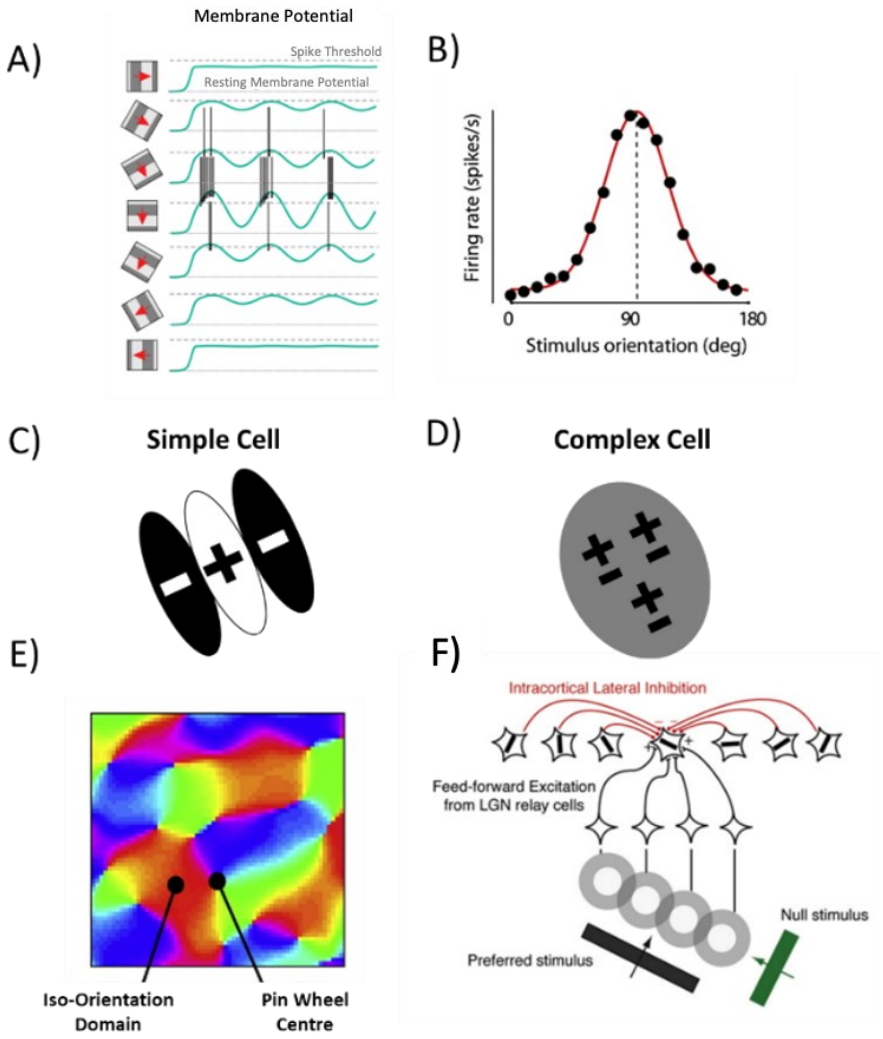

Figure 3: Orientation selectivity in V1 neurons.

(A) In orientation selective neurons, the membrane potential is preferentially increased by specific stimuli orientations that if increased above the spike threshold drive spike trains (adapted from Niell & Scanziani, 2021 [ref. 88]). (B) orientation tuning curve displaying a neuron's firing rate measured in spikes/s across stimulus orientations (adapted from Nauhaus et al. 2008 [ref. 38]). (C) V1 Simple cell RF segregated into distinct on and off regions. (D) V1 Complex cell RFs do not contain distinct on and off regions and thus are activated by both luminance increments and decrements. (E) Orientation map across V1 cortical surface. Neurons within a single iso-orientation domain (red, blue, green regions) all prefer the same orientation, whereas neurons within pin wheel centers (where iso-orientation domains converge) each prefer different orientations and are more broadly tuned (adapted from Nauhaus et al. 2008 [ref. 38]). (F) Feedforward and lateral inhibition theories explaining how orientation tuning arises in V1 neurons (adapted from Priebe & Ferster, 2008 [ref. 40]).

1.1.3.3 Contrast Sensitivity

Visual contrast is the difference in luminance of regions across visual space. Visual neuroscientists use sinusoidal gratings for measuring neuronal contrast responses, which consist of altering light and dark strips (Figure 4a). Sinusoidal gratings can be presented within the RF as a statically flashed stimulus or as a periodically drifting stimulus. Additionally, the alternating light and dark strips of sinusoidal gratings (Figure 4a) can be manipulated to express different contrast levels, orientations, spatial and temporal frequencies to test how visual neurons respond to these stimulus features.

Contrast is coded by neurons in lower stages of visual processing like the retina and LGN [14,18–20], and this coded sensory information is projected to the cortex. V1 neurons increase their response to higher levels of visual contrast[43–48], and this property is represented as contrast response functions (CRFs) that plot a neuron's firing across contrast levels (Figure 4b). Contrast sensitivity in V1 neurons is affected by other features like grating spatial or temporal frequency[43,44]. Additionally, V1 neurons can adapt to grating stimuli, producing characteristic downward shifts in their CRFs after being previously stimulated with high contrast stimuli [45,47].

1.1.3.4 Extra-Classical RF

Research investigating the responsivity of V1 neurons with sinusoidal gratings [35,36,43–48] or bars of light [32–36] usually placed visual stimuli within the neurons classical RF. However, placing stimuli outside of it in the extra-classical RF can affect neuronal activity too [49]. A primary example of this is surround suppression, which can decrease neuron firing to sinusoidal gratings when another stimulus is added to the extra-classical RF in various positions [50].

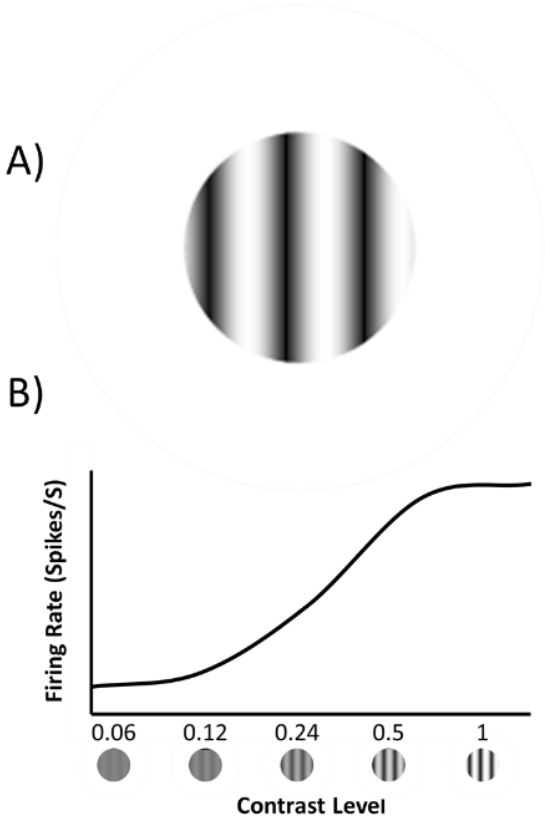

Figure 4: Contrast sensitivity in V1 neurons.

(A) sinusoidal grating consisting of alternating light and dark strips are used to stimulate V1 neurons via superimposing them over V1 RFs. (B) Contrast response function (CRF) representing a neuron's response measured in firing rate, across contrast levels. V1 neurons generally produce small responses to low contrast stimuli and greater responses to high contrast stimuli.

1.2 Cell-Types of the Cortex

1.2.1 Cortical Circuits

1.2.1.1 Canonical Circuity

The cortex is made up of various adjacent networks of densely packed neurons called cortical circuits. Cortical circuits are canonical, exhibiting stereotypical patterns of connectivity, laminar organization, and neuronal cell-types incorporated into the network [51–53]. The cortex spans 6 layers with each one serving specific functions (e.g., Figure 2). TC axons project to cortical layer 4 [29,30,51,52], however this surprisingly makes up a small proportion of all synapses in this layer [54,55]. Instead, the cortex uses intracortical connections to amplify the relatively weak input from TC cells [53]. Cortical neurons belong to two broad classes, excitatory and inhibitory cells that form recognized patterns of connectivity [51,52] , providing unique functions within circuits and must be in balance for proper cortical functioning [42].

1.2.1.2 Excitatory vs. Inhibitory Neurons

Excitatory and inhibitory neurons provide opposing functions in the cortex based on differences in neurotransmission. Excitatory neurons are mainly glutamatergic pyramidal cells (Pyr); when their membrane potential is depolarized enough to surpass the spike threshold, Pyr cells fire action potentials and through a cascade of cellular events release the neurotransmitter glutamate. Glutamate released from these Pyr cells binds to post-synaptic glutamate receptors, subsequently generating excitatory post-synaptic potentials (EPSPs) that can lead to increased post-synaptic spiking. However, cortex layer 4 also contains spiny stellate cells that receive TC input and then activate Pyr cells across cortical laminae [51]. Conversely, inhibitory cortical neurons are mainly GABAergic interneurons; when their membrane potential is depolarized enough to surpass the spike threshold, interneurons fire action potentials and through a cascade of cellular events release the neurotransmitter GABA. GABA released from these interneurons bind to post-synaptic GABA receptors, subsequently generating inhibitory post-synaptic potentials (IPSPs) that can lead to decreased post-synaptic spiking. Beyond producing opposing post-synaptic effects, Pyr cells and interneurons differ in morphology, laminar organization, and connectivity within cortical circuitry.

1.2.2 Pyramidal (Pyr) Cells

Pyr cells align vertically in the cortex and receive synaptic input to their dendritic, perisomatic, and axonal regions from interneurons and other Pyr cells. These inputs generate EPSPs and IPSPs within Pyr cells that summate to influence temporal aspects of neuronal spiking (e.g., spike timing and burst firing)[56], and shape selectivity to sensory stimuli [42]. Pyr cell axons use chemical synapses to form various feedforward and feedback connections in the cortex. Pyr cells from local and distal circuits provide feedforward input to Pyr cells (Figure 5ai – feedforwarded excitation) to push-forward cortical computations [42]. However, these Pyr cells also provide feedforward input to interneurons that can result in these GABAergic cells inhibiting their post-synaptic targets (Figure 5aii – feedforwarded inhibition)[42]. Additionally, when Pyr cells receive GABAergic input from local cortical interneurons, they can provide recurrent connections back to these same interneurons, reciprocally connecting excitatory and inhibitory cells (Figure 5b – recurrent feedback)[42]. In V1, Pyr cells receive TC input and use intracortical connections to process and amplify the inherited sensory signals from the LGN, then push it forward to downstream brain regions for further processing. However, as alluded to interneurons uphold a critical inhibitory function within cortical circuits for regulating these mentioned processes.

1.2.3 Inhibitory Interneurons

1.2.3.1 Interneuron Functional Connectivity

Early anatomists like Ramon y Cajal identified differences in morphological structure between pyramidal and non-pyramidal cells with short-axons, coined interneurons [57]. Cortical interneurons are intermediate cells that use short distanced synaptic connections to provide inhibitory input to other neurons within local circuits. Interneurons of the same cell-type use electrical synapses to synchronize activation of like interneurons and pool inhibitory drive from many cells [58–60]. Interneurons also form chemical synapses onto post-synaptic neurons to dampen their activity by generating IPSPs that reduces firing (Figure 5a-c). In cortical circuits, interneurons use feedback inhibition to regulate local excitation whereby Pyr cells first activated by thalamic input thereafter excite local

GABAergic interneurons [42], but this can be conducted in two ways: recurrent and lateral inhibition (Figure 5b). When interneurons are activated by local Pyr cells, they can send inhibitory input to local Pyr cells that did not previously activate them (Figure 5bi – lateral inhibition)[56] or provide recurrent feedback to these same populations of Pyr cells (Figure 5bii, recurrent inhibition)[56]. Another crucial function of cortical interneurons is disinhibition, whereby driven interneurons provide inhibitory input to other local interneurons for dampening inhibition to downstream Pyr cells (Figure 5c)[56].

1.2.3.2 Excitatory-Inhibitory (E-I) Balance

Interneurons only account for ~20% of cortical neurons [61], however they are a critical aspect of cortical circuits for providing a braking system to dampen local excitation (Figure 5b), inhibition (Figure 5c), and maintain excitatory-inhibitory (E-I) balance within the cortex[42]. First, cortical inhibition prevents runaway excitation that can destabilize activity in the cortex [62,63]. Dysfunctional cortical interneurons can consequently disrupt E-I balance, which is believed to underly several neurological disorders and trigger seizures [64–67]. Therefore, the cortex may function as an inhibition stabilized network (ISN), which posits local excitation within cortical circuits are unstable due to fluctuations in activity generated from feedforward excitatory inputs (Figure 5a) and is stabilized within the cortex by regulating local inhibition (Figure 5a-b) [63,68–70]. Second, cortical inhibition is important for shaping Pyr cell selectivity to stimuli in sensory cortices[42]. Pyr cells summate EPSPs and IPSPs generated from pre-synaptic inputs, which affects their own membrane potential and if above the spike threshold generate action potentials. Importantly, the neuron's spike threshold filters its broadly tuned membrane potential to sharpen its firing rate across a stimulus feature, producing an iceberg effect on neuronal firing (Figure 6)[40,71,72]. Generally, interneurons are more broadly tuned to sensory stimuli than Pyr cells[41], which sculpts Pyr cell tuning (Figure 6)[42].

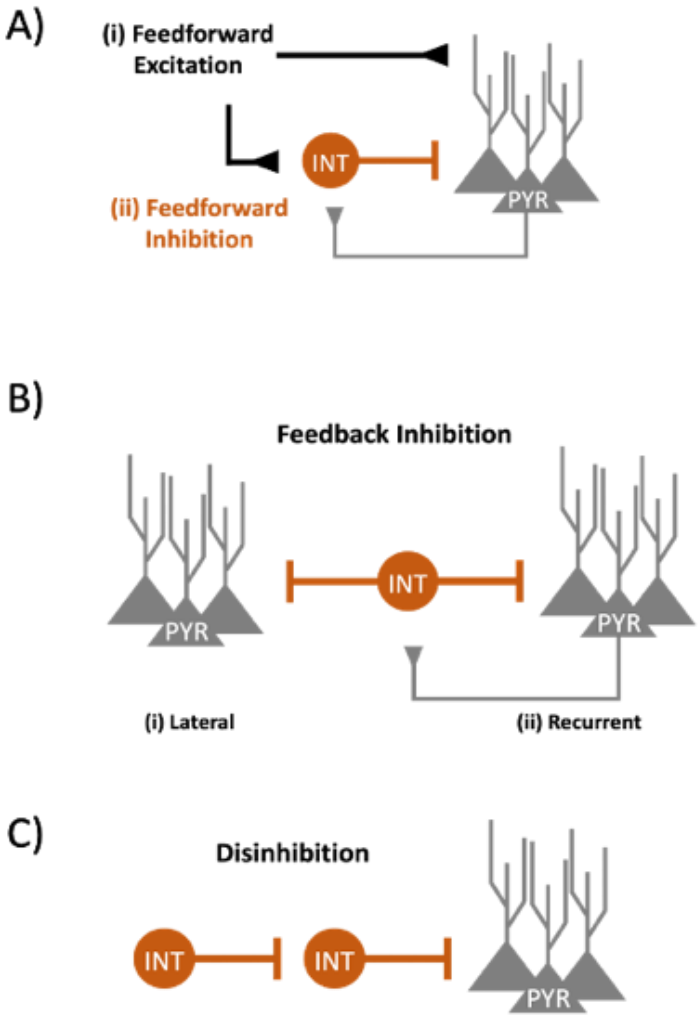

Figure 5: Types of synaptic connections used within cortical circuits.

(A) Pyr cells from other cortical regions (black) provide feedforward excitation (Ai) to activate both interneurons (red) and Pyr cells (grey). Feedforward excitation of interneurons results in interneurons then providing feedforward inhibition to post-synaptic Pyr cells too (Aii). Interneurons imbedded within circuits provide feedback inhibition to local Pyr cells, which can occur via lateral inhibition (Bi) or recurrent inhibition (Bii). (C) Some interneurons inhibit other interneurons producing disinhibition of Pyr cells.

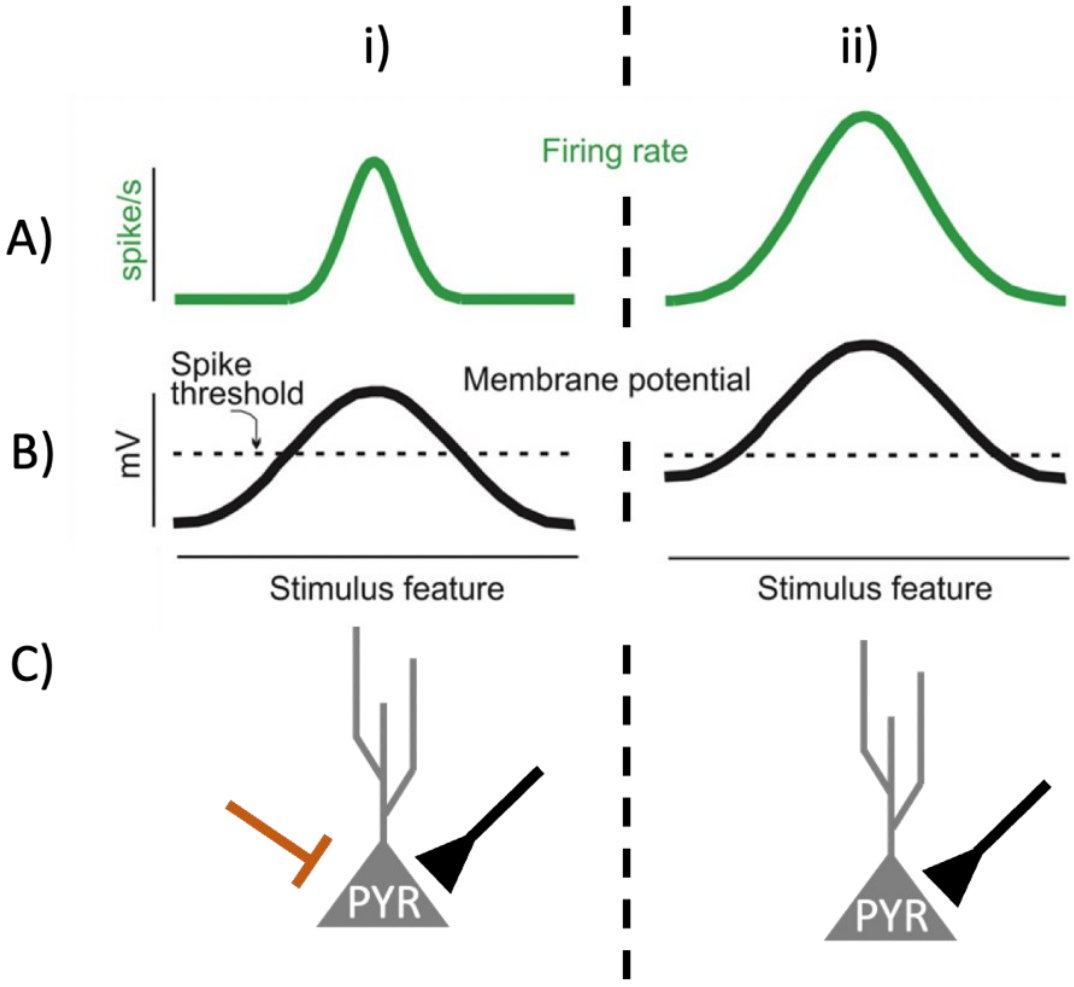

Figure 6: Pyr cell responses are shaped by interneuron-mediated inhibition (Adapted from Isaacson & Scanziani, 2011 [ref. 42]).

Pyr cell stimulus selectivity (spikes/s) can be sharper (Ai) or broader (Aii) based on the neuron's underlying membrane potential. For sharply tuned Pyr cells, (Bi) the neuron's membrane potential only reaches threshold for preferred or near-preferred stimuli (Ci) when visual stimulation increases both excitatory (black) and inhibitory inputs (red) to these neurons because both excitatory and inhibitory conductance's are summed. However, for broader tuned Pyr cells (Bii) the neurons membrane potential reaches the spike threshold for both preferred and non-preferred stimuli (Cii) when the inhibitory input and conductance is removed.

1.2.3.3 Interneuron Heterogeneity

Interneurons are quite heterogeneous, varying in gene expression, biophysical properties, morphological structure, laminar organization [56,73], and early prevailing theories proposed they could likely be divided into distinct groups based on features such as axonal arborizations (e.g. double-bouquet, basket, chandelier) and spiking patterns (fast-spiking and non-fast-spiking interneurons)[52,57,73]. However, gene expression provided a robust characterization for dividing interneurons differing in morphological structure and spiking patterns into three non-overlapping subclasses of parvalbumin (Pvalb+), somatostatin (SOM+), and vasointestinal peptide (VIP+) expressing cells [56,74].

1.3 Transgenic Mice

1.3.1 Transgenic Mice in Visual Neuroscience

The development of novel transgenic mouse lines has provided neuroscientists experimental tools capable of examining V1 in ways not possible in past animal models used in visual neuroscience (e.g. primates, cats). The mouse visual system is undeniably less anatomically sophisticated than that of primates or cats, exhibiting worse visual acuity and lacking clear iso-orientation domains in mouse V1 (Table 1, Figure 7)[75–77]. Still, past research has demonstrated primate, cat, and mouse visual systems share meaningful similarities: all three exhibit the same broad wiring (e.g., geniculo-striate pathway and higher order visual cortex), incorporating parallel afferent inputs from the retina to V1, visual cortices exhibiting retinotopic organization, and monocular and binocular visual fields[77,78]. Furthermore, Mouse V1 neurons can be tuned to visual stimulus features [79], and adapt to visual stimuli (e.g., Contrast adaptation)[80,81]. Therefore, despite mouse visual acuity being measurably worse than cats and primates (Table 1.1, Figure 7), the mouse visual system does share enough similarities with these past animal models to conduct similar visual experiments in mice. Novel genetic tools now available with transgenic mice have aided visual neuroscientists in the pursuit of dissecting the anatomical and functional connectivity of Pvalb+, SOM+, and VIP+ interneurons in mouse V1.

Table 1: Mouse vs non-human primate vision (Adapted from Baker 2013 [ref. 75])

	Mouse Vision	Primate Vision
Total neurons in cortex	14 million	1,400 million
Total neurons in V1	0.2 million	300 million
Proportion of cortex involved in vision.	~10%	~50%
Information routed from eyes to cortex.	< 30%	≥ 90%
Total cortical areas involved in vision	~10	~30

Note: The mouse visual system contains much fewer neurons and is much simpler than the primate visual system.

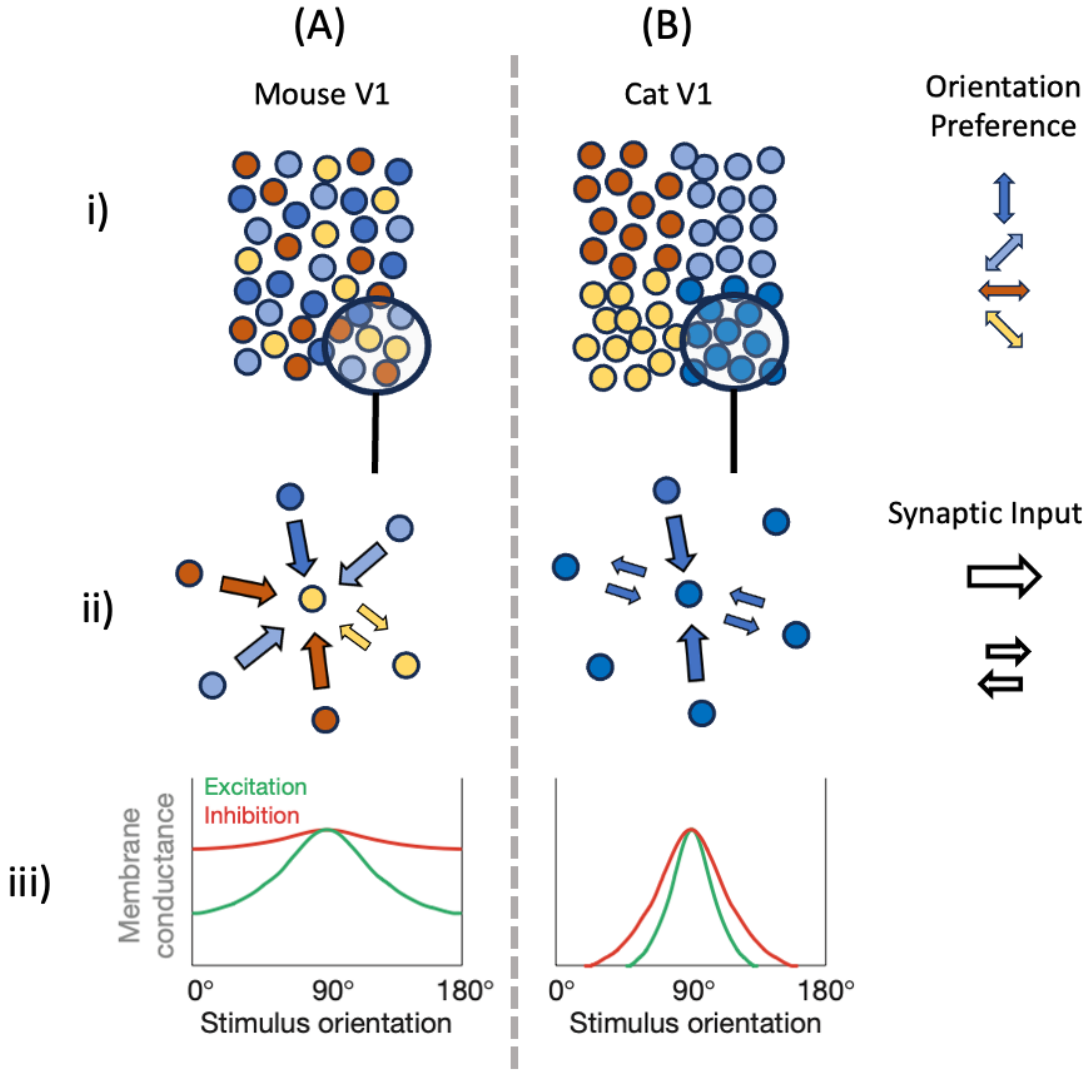

Figure 7: Mouse V1 is much less orientation selective than primate V1 (Adapted from Harris and Mrsic-Flogel, 2013 [ref. 76]).

(Ai) Mouse V1 orientation maps are arranged in a "salt and pepper" organization with adjacent neurons exhibiting different orientation preferences. (Aii) Differentially tuned inputs pool onto single V1 neurons. However, this pooling is denser and more unselective for interneurons than Pyr cells[76], resulting in (Aiii) broadly tuned excitation and even broader inhibition. Conversely, (Bi) cat V1 contains clear iso-orientation domains (also see Figure 3e), with adjacent neurons in each domain exhibiting very similar tuning preferences. (Bii) Similarly tuned inputs pool onto V1 neurons, which again is denser and more unselective for interneurons than Pyr cells[76], resulting in (Biii) more sharply tuned excitation than inhibition, which are both more selective than conductances in mouse V1.

1.3.2 Optogenetics

One of the most revolutionary experimental tools applied in transgenic mice is optogenetics, which can control and perturb neuronal activity *in vitro* or *in vivo* with spatiotemporal precision and reversibility that past methods (e.g., electrical, physical, pharmaceutical perturbation) could not provide[82]. Optogenetics requires light-gated proteins (e.g. ion channels, ion pumps, G-protein coupled receptors) to be genetically inserted into a distinct neuronal cell-type within brain tissue for subsequent light-mediated control of neuronal spiking. Light-mediated optogenetic control of neuronal spiking occurs on a millisecond timescale in neurons expressing optogenetic proteins [83]. A variety of optogenetic proteins have been engineered that differ in (i) the effective light wavelength required to activate the protein, (ii) type of receptor (ion channels, ion pumps, G-protein coupled receptors) and (iii) ion permeability, which can be used to either potentiate, attenuate, or even completely silence genetically manipulated neurons[84]. Arguably the most widely used optogenetic protein is channelrhodopsin-2 (*ChR2*), a nonspecific cation channel that is sensitive to blue light (~480nm light). Photostimulating *ChR2*-expressing neurons with blue light opens these ion channels for cation influx, depolarizing the cells membrane potential for increasing spike output [82,84]. Conversely, inhibitory optogenetic proteins like halorhodopsin (*NpHR*) chloride pumps or archaerhodopsin (*Arch*) proton pumps are sensitive to yellow light (~590nm light). Photoinhibiting neurons expressing *NpHR* or *Arch* with yellow light activates these proteins for Cl^- influx or proton efflux, respectively, which hyperpolarizes the cells membrane potential for reducing spike output [82,84]. Neuroscientists worldwide have utilized optogenetic tools in mice to characterize how cortical Pvalb+, SOM+, or VIP+ interneurons shape sensory processing, including in mouse V1 [85].

1.4 Mouse V1

1.4.1 Mouse V1 Circuitry

V1 circuit mapping has helped progress the understanding of how Pvalb+, SOM+, or VIP+ interneurons function in this network. Initial TC input to mouse V1 targets Pyr and Pvalb+ cells[56], providing little input to SOM+ and VIP+ interneurons [86]. Still, increasing V1 excitation generates proportional increases in local V1 inhibition [87,88]. Within V1 circuitry, each interneuron cell-type has a unique pattern of connectivity: Pvalb+ cells inhibit all neuron subtypes including themselves; SOM+ cells inhibit all neuron subtypes excluding themselves; and VIP+ cells mainly inhibit SOM+ cells but can also inhibit or excite each other weakly (Figure 8)[89,90]. It is noteworthy that mouse V1 does contain a small proportion of other interneuron subtypes that fall outside of these three categories [90]. The distribution of Pvalb+, SOM+, and VIP+ interneurons vary across V1 laminae [91]. Despite Pvalb+ and SOM+ interneurons both providing direct inhibitory input to Pyr cells (Figure 8)[89,90], they differ slightly. Pvalb+ and SOM+ cells bias their input to Pyr cell perisomatic and dendritic regions, respectively (Figure 8)[90]. Work in hippocampus suggests perisomatic-targeted inhibition affects spike timing, whereas dendritic targeted inhibition affects burst firing [56,92,93]. Pvalb+ and SOM+ cells also summate excitatory inputs differently [56,94–96]. Some Pvalb+ cells in layer 6 of mouse V1 also regulate excitatory activity throughout the cortex by arborizing into every cortical layer [97]. Conversely, VIP+ cells function in opposition to Pvalb+ and SOM+ interneurons, providing the cortex its primary source of disinhibition (Figure 5c) by inhibiting SOM+ interneurons (Figure 8)[56,90,98]. Finally, V1 Pyr cells provide recurrent feedback to local interneurons (Figure 8)[90], which is used to regulate inhibition strength within the local circuit for E-I balance [42]. Together, Pvalb+, SOM+, and VIP+ cells form the main groups of interneurons in V1 that shape visual processing in this network.

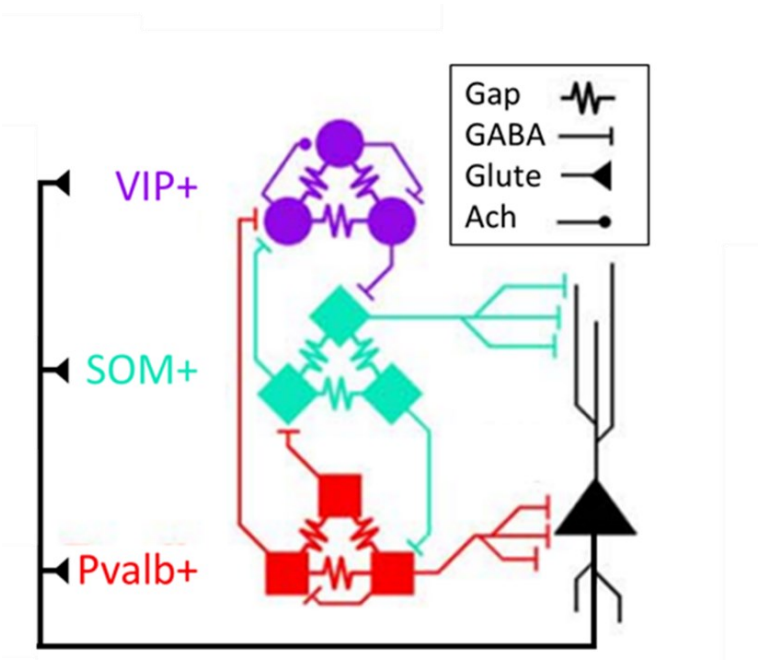

Figure 8: Proposed mouse V1 circuitry from in vitro studies.

Pvalb+ cells (red squares) inhibit all neuron subtypes including themselves; SOM+ cells (green diamonds) inhibit all neuron subtypes excluding themselves; and VIP+ cells (purple circles) mainly inhibit SOM+ cells but can also inhibit or excite each other weakly [89,90]. Interneurons of a single class use electrical (Gap) and cholinergic (Ach) chemical synapses to activate each other. All Interneurons use GABAergic (GABA) chemical synapses to inhibit post-synaptic Pyr cells. Pyr cells use glutamatergic (Glute) chemical synapses to activate local interneurons for feedback inhibition.

1.4.2 Interneurons Shape Visual Processing

1.4.2.1 Pvalb+ vs. SOM+ Interneurons

Both Pvalb+ and SOM+ interneurons directly inhibit Pyr cells (Figure 8), but considering the difference outlined above they are likely to have different functions. A collection of research targeted Pvalb+ and SOM+ cells with optogenetic proteins to modulate their activity for investigating how they contribute to RF properties [85]. Optogenetic activation of *ChR2*-expressing Pvalb+ or SOM+ interneurons both suppress the magnitude of Pyr cell responses to stimuli and depending on light intensity and timing both interneuron subtypes have been shown to maintain Pyr selectivity for visual features like orientation [99–102], which may be driven via the iceberg effect (Figure 6)[100,103,104]. There was debate if Pvalb+ and SOM+ cells each provide distinct inhibitory operations within V1 paralleling subtractive or divisive mathematical operations [102,104,105], but both interneuron subtypes can perform both operations depending on the context [105,106]. Yet, Pvalb+ and SOM+ cells do exhibit key differences in function: SOM+ cells uniquely provide surround suppression for V1 neurons [107,108] and are more orientation selective than Pvalb+ cells [109], but Pvalb+ and not SOM+ cells match excitatory input to layer 2/3 for balancing excitation with inhibition[110].

1.4.2.2 VIP+ Interneurons

The effects of VIP+-mediated disinhibition on basic visual response properties have garnered less attention than Pvalb+ and SOM+ interneurons because VIP+ activity has mainly been linked with specific behavioral states. Locomotion [111] and attention [112] provide top-down modulation of visual responsiveness by activating VIP+ cells in mouse V1. Yet, other studies have indicated VIP+ cells can regulate mouse V1 responsiveness independent of behavioural state, including during locomotion, non-locomotion, visual stimulation, and anesthesia [113]. Photostimulating *ChR2*-expressing VIP+ cells can produce excitation that potentiates the magnitude of V1 neuron responses in awake [111] or anesthetized mice [106]. Surprisingly, in some instances optogenetic activation of *ChR2*-expressing VIP+ cells can inhibit Pyr cells, reminiscent of Pvalb+ and SOM+ interneurons' suppression of Pyr cells [106].

1.5 Rebound Effects

The use of optogenetic modulation of Pyr and interneurons to study cortical circuits has forged new connections to a disparate subfield of systems neuroscience that explores post-inhibitory rebounds.

1.5.1 Post-Inhibitory Rebound (PIR) Effect

Hyperpolarization of a neuron's membrane potential can evoke excess spiking after the inhibitory stimulus is terminated, a phenomenon termed a post-inhibitory rebound (PIR) effect. Functionally, PIRs are proposed to support rhythmic activity in oscillatory circuits or central pattern generators [114–119] via recurrently activating local circuits after bouts of strong inhibition [120]. The cycle of neuronal hyperpolarization generating PIRs is quite fast, occurring in milliseconds [121] to tens or hundreds of milliseconds after hyperpolarization [122,123]. Much of this work has been conducted *in vitro* to identify the underlying ionic currents that produce PIR spikes, such as hyperpolarization-activated (I_h) or low-threshold Ca^{2+} currents [122,124–132]. When a neuron is strongly hyperpolarized (e.g., current injection) this activates I_h currents initiating neuronal depolarization, which then activates low-threshold Ca^{2+} currents to generate rebound depolarization and spiking (Figure 9) [118,119,133]. The rebound firing itself is produced via this low-threshold Ca^{2+} spike depolarizing the cell (Figure 9iii) to activate voltage-gated Na^+ channels (near -55mV), then high-voltage Ca^{2+} channels (near -40mV) but can produce an afterhyperpolarization from increased intracellular Ca^{2+} activating K^+ channels [134]. Membrane hyperpolarization below -65 mV is required for a neuron to generate rebound spiking through this I_h current mediated pathway [118,134]. The intensity of inhibition driving hyperpolarization seems to affect PIR spiking probability and latency [135]. Despite rebound spiking being observed or studied *in vivo* [136–138], some research indicated rebound spiking may be quite rare in intact circuits [139]. Yet, this discrepancy may be explained by PIRs preferentially occurring during distinct brain states such as theta oscillations [121]. Now, research investigating PIRs uses a combination of *in vivo*, *in vitro*, and computational simulations to better investigate how rebound spiking affects other brain functions like sensory processing [128,140–142] or behaviors like spatial navigation [129].

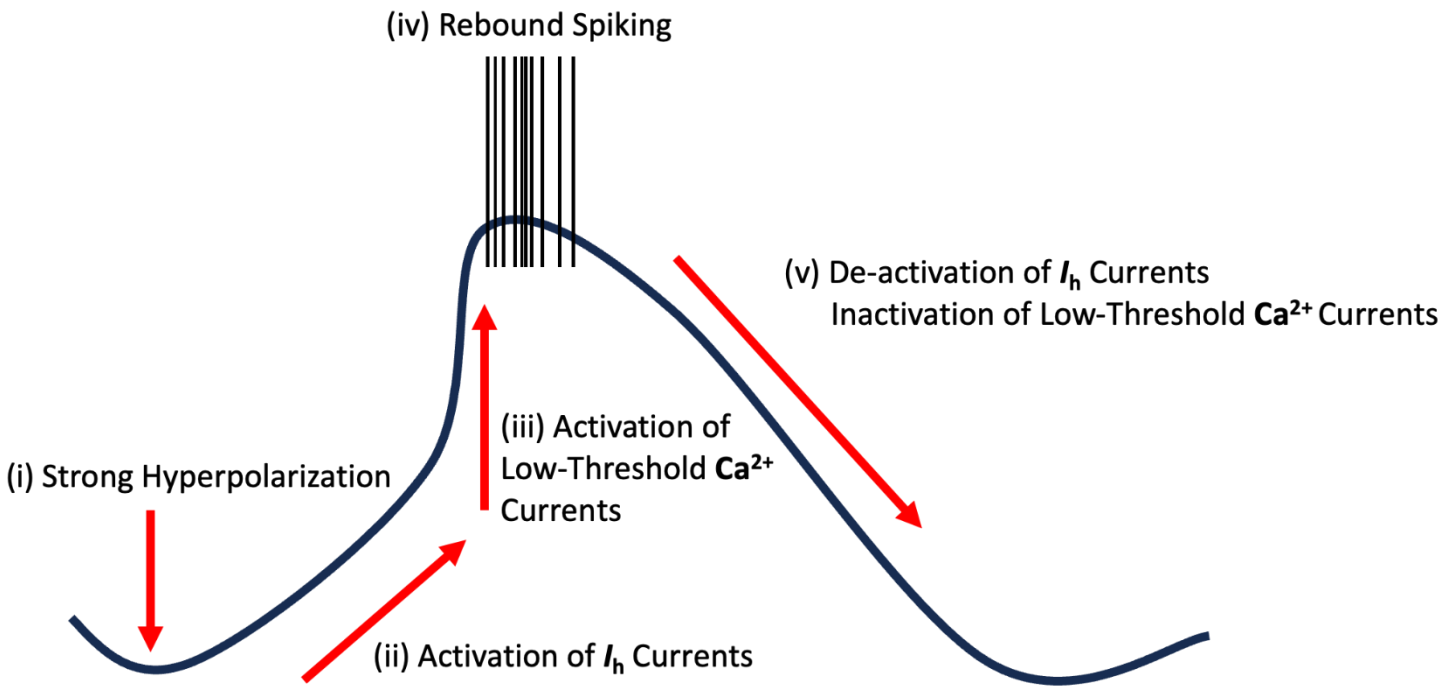

Figure 9: Cellular model for post-inhibitory rebound spiking from in vitro studies (Adapted from Wahl-Schott & Biel, 2009 [ref. 118]).

Black curve represents a cells membrane potential. (i) When a neuron is strongly hyperpolarized below -65mV this (ii) activates hyperpolarization-activated (I_h) currents that begin to depolarize the cell. (iii) I_h currents sequentially activates low threshold Ca^{2+} currents, producing a Ca^{2+} spike in the cell that (iv) drives rebound spiking. (v) A depolarized membrane potential above the spike threshold then de-activates and inactivates I_h and low threshold Ca^{2+} currents, respectively[118,134].

1.5.2 Optogenetic-Mediated Rebound Effects

1.5.2.1 Rebound Effects in Optogenetics Literature.

Rebound spiking has been observed in optogenetic studies too [143–158]. Like PIRs, optogenetic-mediated rebound effects can be I_h dependent [151], which may also affect behavior [155,156,159]. Optogenetic studies have been particularly useful for studying rebound effect-based hypotheses [145] and demonstrating a role for rebound spiking in neurological disorders like epilepsy [143,158,160,161]. Optogenetic-mediated rebounds can arise following several circumstances that produce inhibition. First, inhibitory optogenetic proteins producing direct hyperpolarization by yellow light (e.g., *NpHR* or *Arch*) can produce rebound effects in these same cells (Figure 10a), which has been shown in cortical pyramidal cells [144,148,154] and interneurons [157,161], thalamocortical projections within the cortex [150], tyrosine-hydroxylase-expressing neurons in the locus coeruleus [153], and orexin-expressing neurons in the lateral hypothalamic area [152]. Second, when interneurons express excitatory optogenetic proteins (e.g., *ChR2*), activating them with blue light sends inhibition to post-synaptic neurons, which can elicit rebound spikes in the post-synaptic cells after light offset (Figure 10b)[143,146,147,151,158]. After light offset, previously suppressed neurons can show higher resting membrane potentials than prior to light onset [162] , which may make it easier for these cells to fire post-photostimulation spikes. Furthermore, increasing light power output or photostimulation duration can increase rebound magnitude [147]. However, optogenetic-mediated rebound effects have generally been considered a nuisance, prompting the use of ramp-like light offsets to avoid rebound spiking in cortical pyramidal cells or thalamocortical projections in the cortex [144,150]. Therefore, deliberate work rigorously examining this phenomenon with optogenetics are scant.

1.5.2.2 Thesis Research

Optogenetic-mediated rebound effects have been noted in studies of V1 [144,157] and higher visual areas [146], but we wanted to characterize V1 rebounds more thoroughly to gain insights into cortical function. In this thesis, we used interneuron photostimulation to investigate two network features likely to affect rebound magnitude: 1) activity, probed by examining rebounds against the backdrop of different levels of visually evoked afferent input; and 2) connectivity, probed by stimulating Pvalb+, SOM+, or VIP+ interneurons then measuring ensuing rebounds.

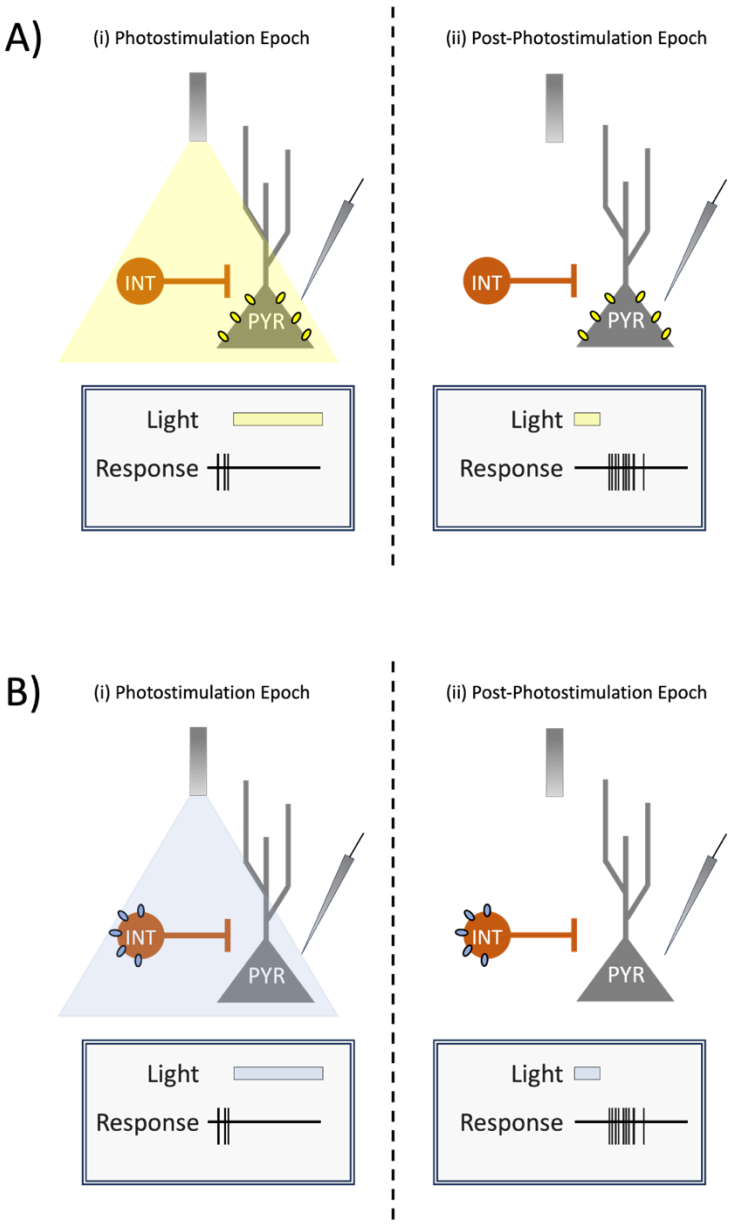

Figure 10: Optogenetic proteins that can drive rebound effects.

(Ai) When inhibitory optogenetic proteins (yellow ovals) are expressed in a neuron (e.g., Pyr cell), photostimulation generates direct inhibition that suppresses its firing. (Aii) At light offset, this can drive rebound spikes in these same neurons. Conversely, (Bi) when excitatory optogenetic proteins (blue ovals) are expressed in GABAergic interneurons, photostimulation drives its firing, increasing IPSPs that suppresses post-synaptic Pyr cell firing. (Bii) At light offset, this can drive rebound spikes in post-synaptic Pyr cells.

2. CHAPTER 2: PUBLICATION FORMAT DATA CHAPTER

Chapter 2 is a publication format data chapter and so it includes its own introduction, methods, results, discussion sections. This research paper has not been submitted to journals yet but has been prepared as a draft for eventual submission to *Journal of Physiology* or *Cerebral Cortex*.

2.1 Introduction

A fundamental aim of systems neuroscience is to determine how neural circuits constructed with different excitatory and inhibitory neurons process information. The mouse primary visual cortex (V1) has become a critical brain area for studying cortical circuits, wherein activity of GABAergic interneurons has been modulated using light-sensitive optogenetic proteins to investigate how they contribute to specific receptive field (RF) properties [85]. *In vitro* studies have described a V1 circuit constructed with excitatory pyramidal cells and several distinct GABAergic interneuron subtypes that differ in morphology, functional connectivity, and distribution across cortical layers that can be segregated into 3 families based on parvalbumin (Pvalb+), somatostatin (SOM+), and vasointestinal peptide (VIP+) expression [56,74]. Most *in vivo* investigations into the potential functions of Pvalb+, SOM+, or VIP+ cells in V1 have focused on how the visual response properties of pyramidal cells can be altered while a particular interneuron subtype is being optogenetically photostimulated [85,99–102,104–106]. However, optogenetic modulations can also elicit excess spikes after light offset compared to control conditions, producing a so-called rebound of neuronal activity during the post-photostimulation epoch [143–145,147,148,150–154,156,158,161]. The occurrence of rebound effects has been briefly noted in studies of V1 [144,157] and higher visual areas [146], but we wanted to characterize optogenetic rebounds in V1 more thoroughly to gain insights into cortical function.

Before the advent of optogenetics, the field of cellular neuroscience studied post-inhibitory rebounds (PIRs) because of the critical role rebound spikes are proposed to serve in oscillatory circuits or central pattern generators [118–120], which have been implicated in sustaining biological rhythms, sensory processing, and behaviours like spatial navigation [114–117,119,120,123,128,129,141,142]. Much of this work has been conducted *in*

vitro to identify the underlying ionic currents that produce PIR spikes, such as hyperpolarization-activated (I_h) or low-threshold Ca^{2+} currents [122,124–132]. When a neuron is strongly hyperpolarized (e.g., current injection) this activates I_h currents that depolarize the neuron, which sequentially activates low-threshold Ca^{2+} currents to generate rebound depolarization and spikes [118,119,133,134]. The rebound firing itself can be driven by low-threshold Ca^{2+} spikes depolarizing the cell to activate some voltage-gated Na^+ channels (near -55mV) and later high-voltage Ca^{2+} channels (near -40mV) but can produce an afterhyperpolarization from increased intracellular Ca^{2+} activating K^+ channels [134]. The intensity of inhibitory drive hyperpolarizing neurons seems to affect PIR spiking probability and latency [135]. Similarly, optogenetic-mediated rebound effects have shown to be I_h dependent [151] and may affect behavior too [155,156,159]. Optogenetic-mediated rebounds can arise following several circumstances that produce inhibition. First, inhibitory optogenetic proteins (e.g., halorhodopsin, archaerhodopsin) producing direct hyperpolarization by light have been shown to trigger rebound spikes after light offset when they are expressed in cortical pyramidal cells [144,148,154] or interneurons [157,161], thalamocortical projections within the cortex [150], tyrosine-hydroxylase-expressing neurons in the locus coeruleus [153], and orexin-expressing neurons in the lateral hypothalamic area [152]. Second, when interneurons express excitatory optogenetic proteins (e.g., channelrhodopsin), activating these interneurons sends inhibition to post-synaptic neurons, which can elicit rebound spikes in the post-synaptic cells after light offset [143,146,147,151,158]. After light offset, previously suppressed neurons can show higher resting membrane potentials than prior to light onset [162], which may make it easier for these cells to fire post-photostimulation spikes. Furthermore, increasing light power output or photostimulation duration can increase rebound magnitude [147]. Despite these insights, optogenetic-mediated rebound effects have generally been considered a nuisance, prompting the use of ramp-like light offsets to avoid rebound spiking in cortical pyramidal cells or thalamocortical projections in the cortex [144,150], and so deliberate work rigorously examining the properties of rebounds with optogenetics is scant.

V1 is an ideal testing ground to explore how cellular and network mechanisms work together to produce optogenetic-mediated rebounds. In the present study, we used Pvalb+, SOM+, or VIP+ photostimulation to investigate two network features that are

likely to impact rebound magnitude: activity and connectivity. We first manipulated local network activity within V1 by presenting visual stimuli that produced strong or weak afferent drive due to specific feed-forward connections from thalamus [40]. Therefore, rebounds elicited by a particular level of interneuron photostimulation were measured against the backdrop of different levels of ongoing network activity. If optogenetic-mediated rebounds in pyramidal cells are primarily produced by membrane hyperpolarization below the spike threshold triggering activation of I_h currents [118,151], then visual stimuli producing excitation and driving spikes should counteract this hyperpolarization and reduce rebounds. Alternatively, if rebound size depends more on the total amount of inhibition impinging on a neuron, combining a set level of interneuron photostimulation with visual stimuli that more strongly drive V1 pyramidal cells should produce stronger rebound effects by increasing feedback inhibition in the local circuit whereby pyramidal cells first activated by thalamic input thereafter excite GABAergic interneurons that then inhibit these same pyramidal cells [42]. Second, we explored the importance of network connectivity on rebound magnitude by photostimulating the three different interneuron subtypes in V1. These subtypes form a well-characterized neural circuit: Pvalb+ cells inhibit all neuron subtypes including themselves; SOM+ cells inhibit all neuron subtypes excluding themselves; and VIP+ cells mainly inhibit SOM+ cells but can also inhibit or excite each other weakly (Figure 11a)[56,89,90]. There are also differences between interneuron subtypes in the thalamocortical input they receive [86], how they summate excitatory inputs [94–96], and regions of pyramidal cells their synapses target (Figure 11a)[56,90]. Therefore, we reasoned that photostimulating each interneuron subtype individually may produce distinct rebound effects. We were surprised to find that photostimulating each interneuron subtype separately could produce rebound effects both within the directly activated interneurons themselves and the post-synaptic pyramidal cells receiving inhibition from them. Rebound size and prevalence were highly variable across all datasets, but overall Pvalb+ photostimulation generally produced the largest rebounds. Most importantly, we found converging evidence from multiple experiments that coupling interneuron photostimulation with visual stimuli that produced higher levels of afferent drive to V1 neurons elicited larger rebounds in more cells.

2.2 Methods

2.2.1 Animals

All experiments were conducted in accordance with the guidelines of the Canadian Council on Animal Care and were approved by the Dalhousie University Committee on Laboratory Animals. Transgenic mice for optogenetic experiments were produced by crossbreeding Ai32 (JAX stock # 012569) mice with Pvalb-IRES-Cre (JAX stock # 008069), Sst-IRES- Cre (Jax Stock #013044), or Vip-IRES-Cre (Jax Stock #010908) mice from The Jackson Laboratory (Bar Harbor, ME, USA). Transgenic mice offspring exclusively expressed Channelrhodopsin 2 (ChR2[H134R]-EYFP) in Pvalb+ (Pvalb-Ai32 mice), SOM+ (Som-Ai32 mice), or VIP+ cells (Vip-Ai32 mice), which allowed for precise photoactivation of these interneuron subtypes *in vivo*. We ensured crossbreeding accuracy by genotyping with standard polymerase chain reaction testing. Part of this study involved reanalyzing data we previously published [103,106], which consisted of electrophysiological recordings from a total of 31 (16 female) Pvalb-Ai32, 13 (5 female) SOM-Ai32, and 8 (5 female) Vip-Ai32 transgenic mice. Novel data for the present study was collected from 11 (6 female) Pvalb-Ai32 mice. All mice were 2–9 months old and weighed between 20-30 g.

2.2.2 In Vivo Electrophysiology

Mice were sedated with chlorprothixene (Sigma Aldrich, 5 mg / kg, i.p.) and subsequently placed into a custom facemask for anesthesia with isoflurane in oxygen, which was continually administered throughout the entirety of the experiment (2.5% isoflurane during induction, 1.5% during surgery and 0.5% during recording; Pharmaceutical Partners of Canada). Chlorprothixene top-up doses were administered every 4 hours. A heating pad was used to ensure body temperature was held at 37.5 °C for the entirety of the experiment. Anesthetic depth was tested with the withdrawal toe-pinch reflex, and surgical procedures were performed only when mice reached anesthetic surgical plane. Once in surgical plane, the scalp was retracted, and the skull was immobilized by attaching a head-post with dental epoxy. We identified V1 with stereotaxic coordinates (0.8 mm anterior and 2.3 mm lateral from lambda [163] and exposed it with a small craniotomy (~1 mm^2) for later electrophysiological recordings and

optogenetic photostimulation. We surrounded the craniotomy edge with petroleum jelly, forming a well that was filled with saline to prevent dehydration of cortical tissue. We protected the corneas with frequent application of optically neutral silicone oil (30,000 cSt, Sigma Aldrich). Mouse eye movements under anesthesia have been shown to be negligible [78,79,164], therefore eyes were not immobilized, and pupils were not dilated to maintain a large depth of focus.

Initial extracellular recordings were performed using a glass micropipette (tip diameter of 2–5 μm filled with 2 M NaCl) to localize the monocular retinotopic portions of V1 (~30–90° azimuth and 10–40° elevation). We then inserted a tetrode for multi-channel recordings (Teflon coated NiCr wire with gold plated tips; impedance ~300 kΩ). Electrode or tetrode recordings were made by vertical electrode penetrations 100-650 μm below the cortical surface via a micromanipulator (FHC). Electrophysiological signals were bandpass filtered (50-2000 Hz) and sampled (25 kHz) with a CED 1401 digitizer and Spike2 software (Cambridge Electronic Designs), and online analyses were performed in Spike2 from triggered transistor–transistor logic (TTL) pulses from a window discriminator (Cornerstone by Dagan). Offline spike sorting was conducted with Spike2 software using a supervised template-matching algorithm. Single units were identified in multi-unit recordings by generating templates that displayed unique spike-waveforms and spike-patterning across tetrode channels, and isolation was confirmed using principal component analysis and inter-spike interval histograms.

2.2.3 Optogenetic Photostimulation

For all experiments we optogenetically activated either Pvalb+, SOM+, or VIP+ interneurons using a 470-nm fiber-coupled LED (0.4-mm diameter; 0.39 NA; Thor Labs) situated ~0.2– 0.5 mm above the exposed V1 surface. The CED 1401 synchronized the timing of LED activation and visual stimulus presentation. We used a MATLAB (MathWorks) Monte Carlo modeling toolbox to estimate the light intensity at a given cortical depth based on our LED power output of 0.002-2.1 mW [165], which can generate photocurrents in layer 6 ChR2(H134R)-EYFP expressing GABAergic interneurons [165,166]. Our LED power output for photostimulating V1 interneurons was sufficiently strong to

silence V1 pyramidal cell visual responses [99,167], therefore at each recording site we examined multiple light intensities used to induce suppression of multi-unit responses to visual stimuli online. After multiple attempts, we then selected a light intensity that produced moderate suppression for the experimental protocols (0.06–0.44 mW/mm^2 at the cortical surface; median = 0.18 mW/mm^2). This dim cortical illumination was applied in a continuous block to maintain potentially important temporal features in neuron firing (e.g., onset transients, firing rate decay, phase preference) that may impact ensuing post-photostimulation rebound effects. Finally, at the intensity used, 470 nm light diffuses a few hundred microns laterally from the fiberoptic, though activation travelling through gap junction connected networks of interneurons can reach a radius of ~ 1 mm [147], which encompassed the area of V1 expected to be retinotopically activated by the visual stimuli used in this study.

2.2.4 Visual Stimulus

Visual stimuli were programed in MATLAB using the Psychophysics Toolbox extension (Pelli 1997; Brainard 1997), and during experiments we stimulated mouse V1 neurons by presenting stimuli on a calibrated CRT monitor (LG Flatron 915FT Plus 19-inch display, 100 Hz refresh, 1024 × 768 pixels, mean luminance = 30 cd/m^2) at a viewing distance of 15– 30 cm within monocular retinotopic receptive fields (RFs). Visual stimuli for all experiments were either drifting gratings (Experiments 1 and 3) or flashed vertically oriented bars (Experiment 2).

Drifting gratings were presented in an aperture surrounded by a gray field of mean luminance. All gratings had a spatial frequency (SF) of 0.03 cycles per degree and temporal frequency (TF) of 2 Hz, which approximated mouse V1 neuron population averages [79,168] to elicit strong responses from the majority V1 neurons within multi-unit recordings due to broad spatiotemporal tuning across several octaves of SF and TF [79,81,168,169]. At each recording site, we first performed preliminary analyses of RF size (4–64° diameter apertures) and orientation/direction (22.5° resolution) preferences by constructing online tuning functions using TTL triggering of the best isolated unit, which aided in selecting appropriate stimulus parameters for ensuing experimental recordings.

2.2.4.1 Experiment 1

In experiment 1 we examined rebounds produced when a set level of Pvalb+, SOM+ or VIP+ photostimulation was paired with different levels of afferent drive to V1 from gratings of varying contrasts (reanalysis of Shapiro et al. 2022 data [ref. 106]). Visual grating contrast was defined as:

$$\%\ Michelson\ Contrast = \frac{(L_{max} - L_{min})}{(L_{max} + L_{min})} \times 100 \quad (1)$$

where L_{max} and L_{min} are the maximum and minimum luminance in the grating, respectively. Five grating contrast levels (6, 12, 24, 50, 100%) were presented for 1 s each in random order followed with by a homogeneous grey screen lasting 2 seconds during the interstimulus interval (ISI). Photostimulated trials were randomly interleaved with non-photostimulated control trials. Photostimulation lasted for 1s and completely overlapped in time with the visual stimuli (Fig. 1b-d inset), which produced photostimulation and post-photostimulation epochs to examine optogenetic modulation and rebound effects, respectively. We recorded 8-12 repetitions of each contrast level for both control and photostimulation trials.

2.2.4.2 *Experiment 2*

In experiment 2 we examined rebounds produced when a set level of Pvalb+ photostimulation was paired with single black or white vertically oriented bars flashed inside or outside of the RF to elicit varying levels of afferent drive (reanalysis of Shapiro et al. 2022 data [ref. 103]). During each trial, a single black or white vertically oriented bar was flashed in 1 of 9 randomly selected locations over a homogenous grey background of mean luminance (Figure 29a). The bar appeared at 100ms into each trial then vanished at 600ms, and the grey background remained on the monitor for an additional 400ms before the next trial was initiated. On photostimulated trials, the LED was on for the first 600ms, which produced photostimulation and post-photostimulation epochs to examine optogenetic modulation and rebound effects, respectively. Control and photostimulation trials were randomly interleaved, and all 9 bar locations of each bar type were presented for 20 repetitions each.

2.2.4.3 Experiment 3

In experiment 3 we examined whether rebound magnitude was influenced by afferent drive to V1 during either the pre-photostimulation, photostimulation, or post-photostimulation epochs by varying the timing of Pvalb+ photostimulation relative to the appearance of a drifting grating. The visual stimulus in all conditions was a 100% contrast drifting grating that appeared 500ms into the trial and disappeared at 1500ms. During photostimulated trials, the LED was turned on for 500ms at four different delays to create four distinct conditions named after the level of afferent drive during the photostimulation and post-photostimulation epochs. In the "Lo-Hi" condition, the cortex was illuminated in the first 500ms before the grating appeared, thus there was low afferent drive when the LED was on, but high afferent drive in the post-photostimulation epoch due to the appearance of the grating (Figure 30a). In the "Lo-Lo" condition the cortex was illuminated between 1501 and 2000ms, thus there was low afferent drive in both photostimulation and post-photostimulation epochs because the grating had disappeared before the LED turned on (Figure 30b). In the "Hi-Hi" condition, the cortex was illuminated between 501 and 1000ms, thus there was high afferent drive when the LED was on due to the appearance of the grating, and afferent drive remained high in the post-photostimulation epoch due to the grating's continued presence (Figure 30c). Finally, in the "Hi-Lo" condition, the cortex was illuminated between 1001 and 1500ms, thus there was high afferent drive when the LED was on due to the presence of the drifting grating, but afferent drive was low in the post-photostimulation epoch due to the grating's disappearance at 1500ms (Figure 30d). We recorded 8-12 repetitions of each condition for both control and photostimulation trials.

2.2.5 Data Analysis

Isolated single units collected from all 3 experiments were exported to MATLAB where neuronal responses over time were represented as spike density functions (SDFs) with 1kHz resolution, which were generated by convolving a delta function at each spike arrival time with a Gaussian window. For all data sets, we standardized the magnitude of optogenetic effects by using a Z-score calculation ($Z= [x-\mu]/\sigma$). First, we estimated the mean (μ) and standard deviation (σ) of the difference between photostimulation and

control SDFs during a segment of each trial far removed from photostimulation or rebounds effects (the last 1s of the ISI for experiment 1; last 100ms of the ISI for experiment 2; and last 500ms of the ISI for experiment 3). Then, we calculated x as the difference between photostimulation and control SDFs within the photostimulation and post-photostimulation epochs (Figure 11b-d; top panel). We used Z-score functions to calculate photomodulation latency and sign while accounting for variability of neural firing and used a threshold Z-score of ±2 to determine when the difference between photostimulation and control trails began to differ significantly [103,106]. We distinguished whether each single unit was an optogenteically activated interneuron or photomodulated Pyr cell using calculated photomodulation latency and Z-score sign [103,106]. For population analyses, multiple Z-score functions were represented within a single figure as either an average Z-score function or heatmaps where yellow and blue indicated facilitation or suppression relative to spontaneous firing, respectively.

2.2.6 Statistical Analysis

Parametric tests were used for statistical analyses (specific tests noted in *Results*).

2.3 Results

Prior to searching for optogenetic-driven rebound effects in our electrophysiological recordings, we segregated directly photostimulated interneurons from post-synaptic putative pyramidal (Pyr) cells that receive inhibition. In Pvalb-Ai32, SOM-Ai32, and VIP-Ai32 transgenic mice, photostimulating ChR2(H134R)-EYFP-expressing interneurons generates rapid depolarization in these cells soon after light onset (Figure 11b)[106], which yielded positive Z-scores > 2 indicating facilitation and median photomodulation latencies of 3 ms, 1 ms, and 1 ms in Pvalb-Ai32, SOM-Ai32, and VIP-Ai32 transgenic mice, respectively (Figure 11e-g). Conversely, putative Pyr neurons that receive inhibitory projections from these directly activated interneurons will be modulated after some synaptic delay [106]. Monosynaptic GABAergic projections to Pyr cells produced negative Z-scores < -2 (Figure 11c), with median photomodulation latencies of 85 ms, 79 ms, and 87 ms in Pvalb-Ai32, SOM-Ai32, and VIP-Ai32 transgenic mice, respectively (Figure 11e-g). Pyr cells polysynaptically disinhibited by VIP+ photostimulation produced positive Z-scores > 2 at even longer latencies (Figure 11d), with a median photomodulation latency of 113ms in VIP-Ai32 transgenic mice. Following our previous methods [103,106], units with Z-scores > 2 and photomodulation latency < 30 ms were classified as photostimulated interneurons, and units with photomodulation latency > 30 ms were classified as Pyr cells (Figure 11e-g).

2.3.1 Experiment 1

Our primary goal was to determine if network features like activity or connectivity affect optogenetic-mediated rebound magnitude. To test this here, Pvalb+, SOM+, or VIP+ photostimulation of constant duration and strength was paired with different levels of afferent drive to V1 produced by presenting drifting gratings of different contrast levels. Using the photomodulation latency criteria above, our sample consisted of 157 Pyr_{pvalb} and 54 Pvalb+ cells in Pvalb-Ai32 mice (Figure 11e), 80 Pyr_{som} and 21 SOM+ cells in SOM-Ai32 mice (Figure 11f), and 99 Pyr_{vip} and 13 VIP+ cells in Vip-Ai32 mice that were split according to whether VIP+ photostimulation suppressed (Figure 11c; Pyr_{vip}^{supp}) or disinhibited (Figure 11d; Pyr_{vip}^{facil}) visual responses (Figure 11g).

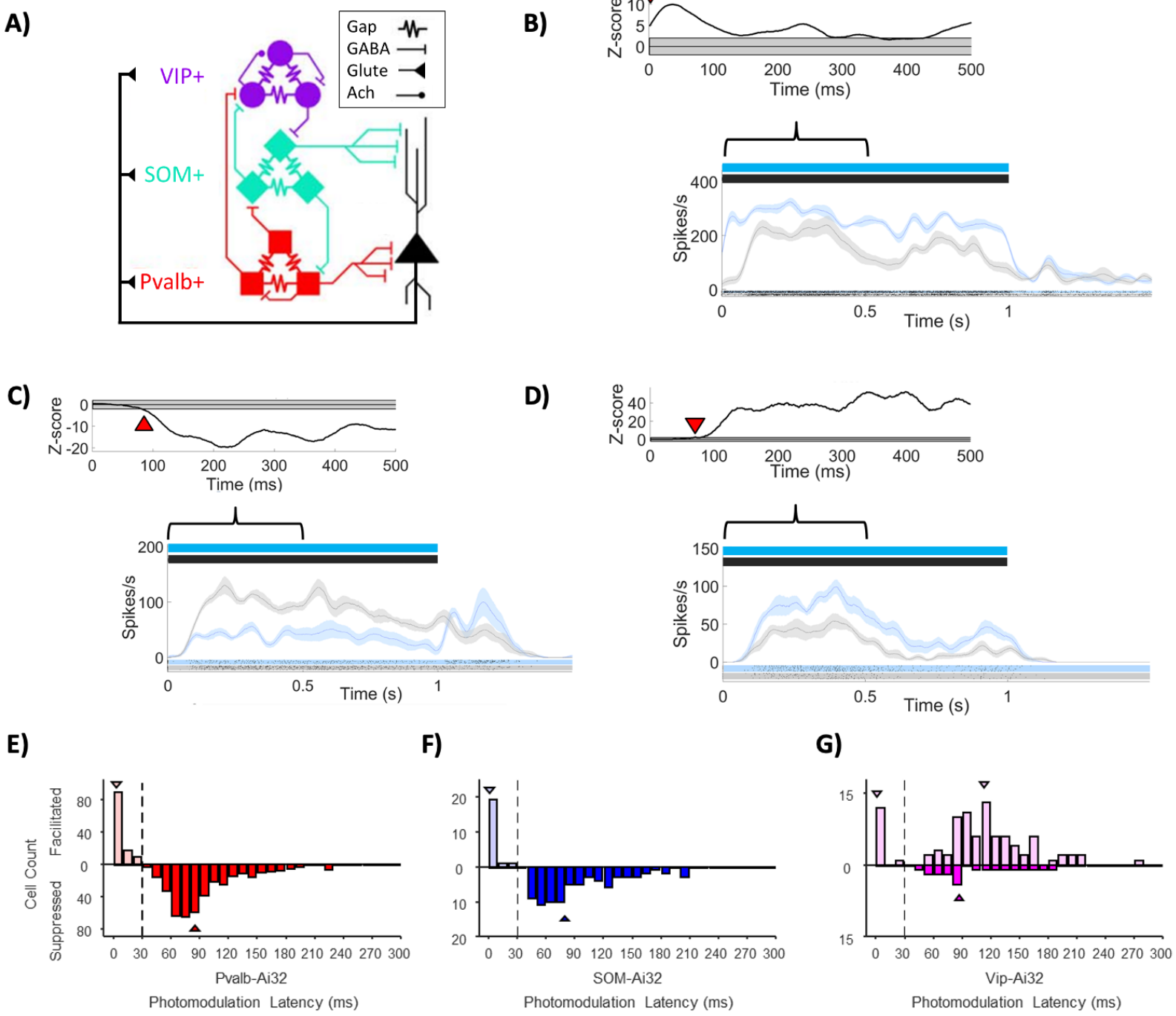
A)
Gap
GABA
Glute
Ach
VIP+
SOM+
Pvalb+
B)
Z-score
Time (ms)
Spikes/s
Time (s)
C)
Z-score
Time (ms)
Spikes/s
Time (s)
D)
Z-score
Time (ms)
Spikes/s
Time (s)
E)
Cell Count
Facilitated
Suppressed
Pvalb-Ai32
Photomodulation Latency (ms)
F)
SOM-Ai32
Photomodulation Latency (ms)
G)
Vip-Ai32
Photomodulation Latency (ms)

Figure 11: Optogenetic photomodulation latencies for mouse V1 neurons.

A) Wiring diagram of mouse V1 circuitry, including Pyr cells and interneurons outlined *in vitro* [89,90]. Pyr cells (black triangles) use glutamatergic (Glute) chemical synapses, whereas Pvalb+ (red squares), SOM+ (teal dimanonds), and VIP+ interneurons (purple circles) use GABAergic (GABA) chemical synapses to excite or inhibit post-synaptic cells, respectively. Interneurons of a single class use electrical synapses (Gap) and cholinergic (Ach) chemical synapses to activate each other. (B) Bottom figure: spike density function (SDF) and raster plot showing a single Pvalb+ cells response to drifting sine wave gratings without (grey line) or with optogenetic activation (blue line). Shading around grey and blue lines indicate standard error of the mean (SEM). Above SDF describes the timing of photostimulation (light blue bar) and visual stimulation (thick black bar). Top figure: Z-score function (black line) indicating the difference in firing between optogenetic and control conditions from SDF below. Shaded area surrounding the zero-line indicates a Z-score of ±2, which was used as a threshold to determine a neurons photomodulation latency. Red triangle indicates when the Z-score function surpassed this threshold for producing a photomodulation. (C) SDF and Z-score function measuring the response of a putative Pyr cell to drifting sine wave grating, recorded in a Pvalb-Ai32 mouse. The format is identical to B. The longer latency (red triangle) and sign of the photomodulation (Z-score < -2) in the Z-score function for this Pyr cell indicates synaptic inhibition. (D) SDF and Z-score function measuring the response of a putative Pyr cell to drifting sine wave grating, recorded in a Vip-Ai32 mouse. The format is identical to (B). The longer latency (red triangle) and sign of the photomodulation (Z-score > 2) in the Z-score function for this Pyr cell recorded in a Vip-Ai32 mouse indicates synaptic disinhibition. (E-G) Histograms plotting all recorded neuron photomodulation latencies from Pvalb-Ai32 (red), Som-Ai32 (blue), and Vip-Ai32 mice (purple). Upward pointing, lightly shaded bins indicate neurons that were facilitated, whereas downward pointing, shaded bins indicate neurons that were suppressed. Following our methods [103,106], we used a threshold of 30 ms to split interneurons from putative Pyr cells (vertical dotted line). Arrows indicate the median photomodulation latency for interneurons or Pyr cell groups recorded from Pvalb-Ai32, Som-Ai32, and Vip-Ai32 mice. Note in (E-F) all recorded Pyr cells from Pvalb-Ai32 and Som-Ai32 mice were suppressed, whereas in (G) recorded Pyr cells from Vip-Ai32 were either suppressed (Pyr_{vip}^{supp}) or facilitated (Pyr_{vip}^{facil}).

2.3.1.1 Pyr Cell Rebound Effects

We first searched for rebound effects in Pyr cells that receive inputs from optogenetically activated interneurons. The example Pyr_{pvalb} cell in figure 12 shows incrementally larger spike rates to higher visual contrasts in control SDFs (black trace), and corresponding increases in suppression at higher contrasts during Pvalb+ photostimulation (blue trace). Directly after cortical illumination is terminated for the three highest contrast levels, the spike rate in the photostimulated SDF increases above the control SDF, signifying rebound spikes (figure 12c-e). When optogenetic modulation is represented as a Z-score function, suppression during the photostimulation epoch is represented as negative Z-scores, and the transiently positive Z-scores in the post-photostimulation epoch indicate a rebound effect (Figure 12f-j). For this Pyr_{pvalb} cell, both inhibitory photomodulations and subsequent rebound effects were largest in the 100% Z-score function (Figure 12j). Very similar rebound effect trends are evident in example Pyr cells pairing high contrast stimuli with inhibition mediated by SOM+ (Figure 13) or VIP+ photostimulation (Figure 14), though only produced rebounds at 100% contrast. However, this rebound effect trend was not produced at high contrast levels when VIP+ photostimulation disinhibited the example Pyr_{vip}^{facil} cell (Figure 15).

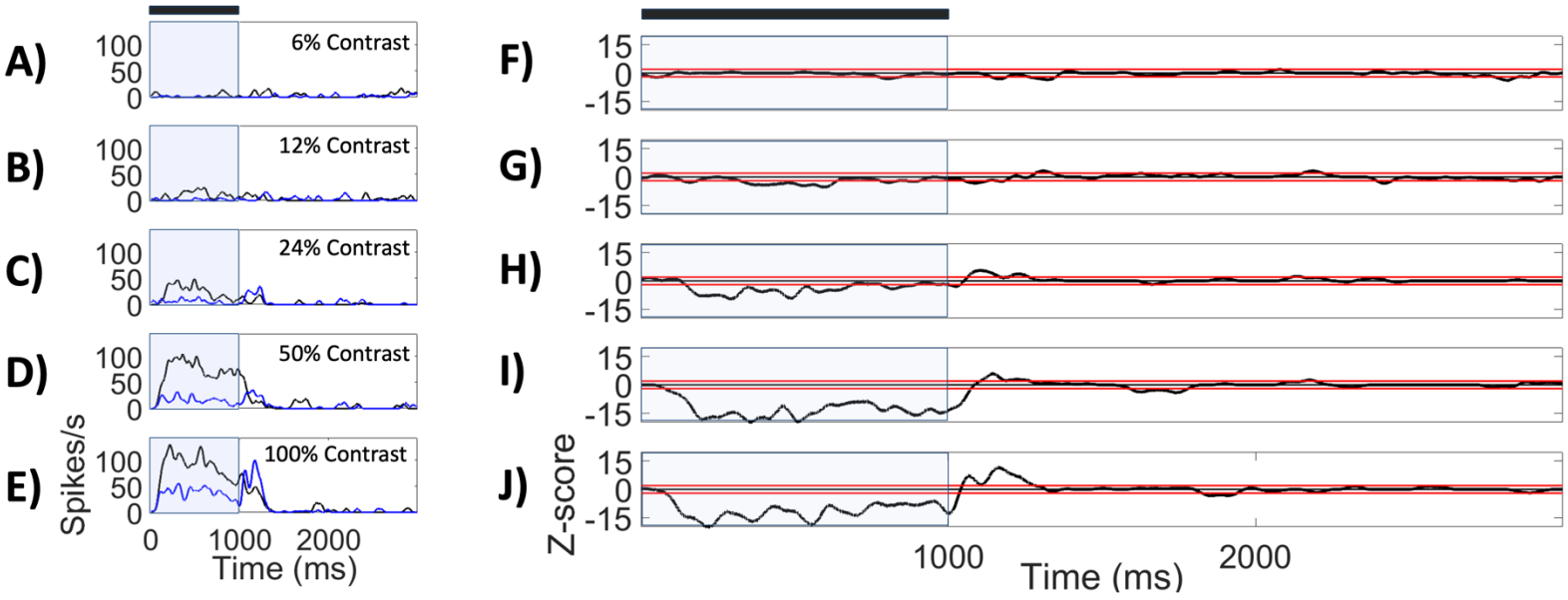

Figure 12: Single Pyr$_{pvalb}$ cell recorded from a Pvalb-Ai32 mouse.

(A-E) SDFs indicating a single Pyr cell's firing during control (black) and optogenetic conditions (blue), spanning 6-100% contrast levels. The blue shaded area (0-1000 ms) superimposed over the SDF indicates the duration of photostimulation, which temporally overlapped with visual stimulation (dark grey bar). The white area (1001-3000 ms) indicates the post-photostimulation epoch. (F-J) Z-score functions (black lines) derived from SDFs at corresponding contrast levels. The horizontal lines (red) below and above the zero-line indicate a Z-score of ±2. The blue shaded area (0-1000 ms) superimposed over the Z-score function indicates the duration of photostimulation, which temporally overlapped with visual stimulation (dark grey bar).

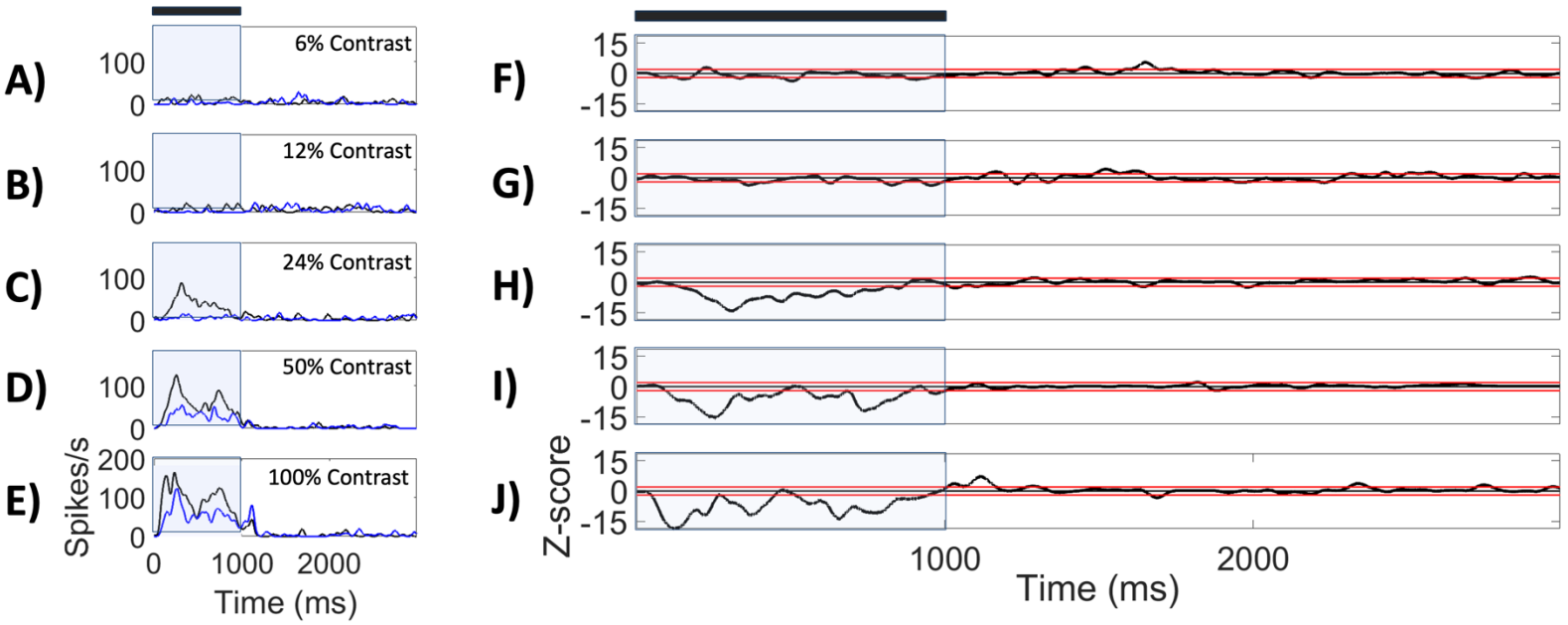

Figure 13: Single Pyr$_{som}$ cell recorded from a Som-Ai32 mouse.

(A-E) Same layout as figure 12, but for a single Pyr$_{som}$ cell.

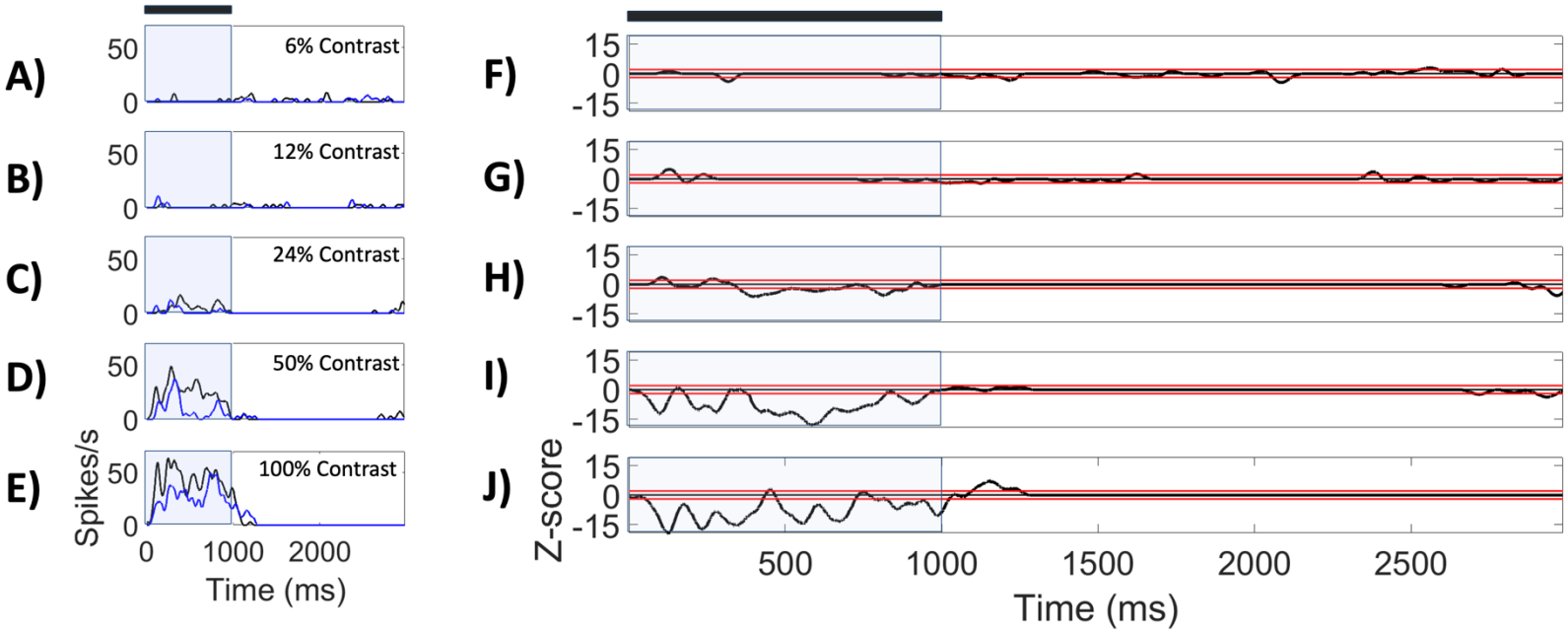

Figure 14: Single Pyr_{vip}^{supp} cell recorded from a Vip-Ai32 mouse.

(A-E) Same layout as figure 12, but for a single Pyr_{vip}^{supp} cell.

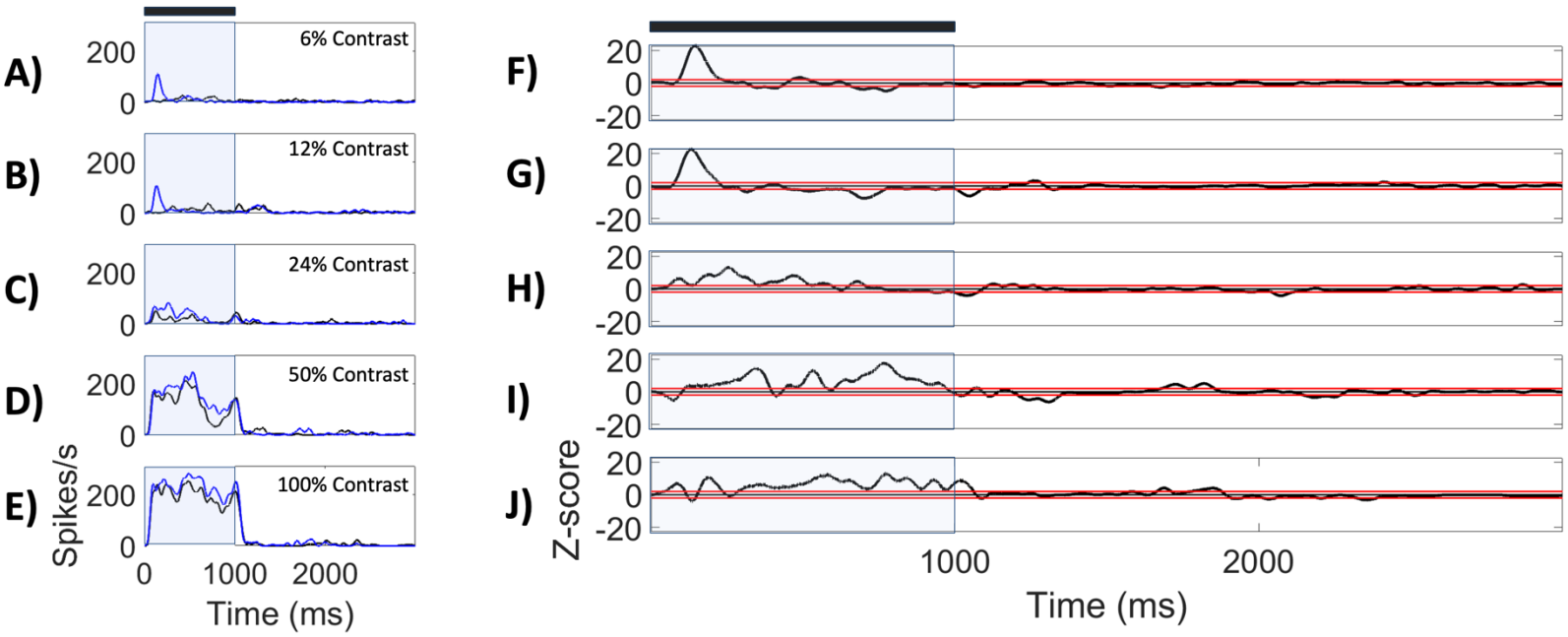

Figure 15: Single Pyr_{vip}^{facil} cell recorded from a Vip-Ai32 mouse.

(A-E) Same layout as figure 12, but for a single Pyr_{vip}^{facil} cell.

We compared rebound effects within and between each Pyr cell dataset by creating population average Z-score functions for Pyr_{pvalb}, Pyr_{som} Pyr_{vip}^{facil}, Pyr_{vip}^{supp} cells that included Z-score traces for each contrast level used (Figure 16a,c,e,g). Pyr_{pvalb}, Pyr_{som}, Pyr_{vip}^{supp} population data exhibited similar trends to the example cells in figures 12-14, with all groups producing visible positive rebounds specifically after being driven by 100% contrast stimuli that generated the most afferent drive in V1 (Figure 16a,c,e). The population average Pyr_{pvalb} cell rebounds to 100% contrast (Figure 16a) appeared to be about twice the size of rebounds in Pyr_{som} and Pyr_{vip}^{supp} cells (Figure 16c,e). Pyr_{pvalb} cells also exhibited small rebounds at 50% contrast that were not produced in Pyr_{som} and Pyr_{vip}^{supp} cell 50% contrast average Z-score traces (Figure 16a,c,e). Conversely, the Pyr_{vip}^{facil} cell dataset produced an entirely different rebound trend compared to suppressed Pyr cell groups; VIP+ photostimulation generally increased Pyr_{vip}^{facil} firing that produced positive Z-scores during the photostimulation epoch, which waned over time at contrast levels ≤ 24% (Figure 16g). In the post-photostimulation epoch, the Pyr_{vip}^{facil} cell population Z-scores appeared to depend on contrast levels shown previously. There was little evidence of rebounds at the population level following high contrast stimuli, whereas for contrast levels ≤ 24% positive Z-scores during photostimulation were followed by more positive Z-scores after light offset to produce an inverted rebound effect (Figure 16g).

Next, we quantified the magnitude of rebounds in individual Pyr_{pvalb}, Pyr_{som}, Pyr_{vip}^{supp}, Pyr_{vip}^{facil} cells by calculating the time-averaged Z-score from 1050-1400ms at each contrast. Figure 16b,d,f,h shows this population data as scatter column plots. Generally, rebound magnitude increased with stimulus contrast, but there was variability in the size of this effect across datasets. We incorporated all Pyr cell datasets into a mixed model ANOVA comparing the effect of contrast level (within group) and mouse type (between groups) on mean rebound size, which showed significant main effects for Pyr cell rebounds differing between contrast levels [$F(4, 12) = 2.99$; $p = 0.018$; $N = 336$] and mouse types [$F(3, 12) = 7.63$; $p = 6.03 \times 10\text{-}5$; $N = 336$], with a significant interaction between contrast levels and mouse types [$F(12) = 7.31$; $p = 3.96 \times 10\text{-}13$; $N = 336$]. Estimated marginal means suggested meaningful differences between various contrast levels within and between Pyr cell datasets (Figure 16i). Post hoc comparisons using

Tukey HSD tests indicated mean rebound size across contrast levels for Pyr_{pvalb} cells significantly differed from Pyr_{som} cells (*MD* = 0.248; *SE* = 0.082; T = 3.033; p_{Tukey} = 0.014; N = 237) and Pyr_{vip}^{supp} cells (*MD* = 0.525; *SE* = 0.141; T = 3.720; p_{Tukey} = 0.001; N = 177) but the Pyr_{som} and Pyr_{vip}^{supp} datasets did not significantly differ from each other (*MD* = 0.277; *SE* = 0.149; T = 1.866; p_{Tukey} = 0.245 N = 100). The overall pattern of rebounds in Pyr_{vip}^{facil} cells differed greatly from the datasets where interneuron photostimulation produced Pyr suppression (Figure 16i), and it is noteworthy that when the ANOVA was re-run excluding the Pyr_{vip}^{facil} dataset both main effects for contrast [F (4, 8) = 7.44; p = 6.63×10^{-6}; N = 257], mouse type [F (2, 8) = 12; p = 1.03×10^{-5}; N = 257], and the interaction [F (8) = 2.81; p = 0.004; N = 257] remained significant. Post hoc comparisons using the Tukey HSD tests indicated mean rebound size across contrast levels for Pyr_{vip}^{facil} cells significantly differed from Pyr_{som} cells (*MD* = -0.273; *SE* = 0.094; T = -2.897; p_{Tukey} = 0.021; N = 159) and Pyr_{vip}^{supp} cells (*MD* = 0.551; *SE* = 0.149; T = 3.699; p_{Tukey} = 0.001; N = 99) but did not significantly differ from Pyr_{pvalb} cells (*MD* = -0.026; *SE* = 0.082; T = -0.310; p_{Tukey} = 0.99; N = 238). V1 neurons produced larger rebounds after interneuron photostimulation was paired with the highest contrast stimuli generating the most afferent drive in V1 (Figures 16a-f), with exception to Pyr_{vip}^{facil} cells that produced paradoxical inverted rebounds at lower contrasts (Figures 16g-h).

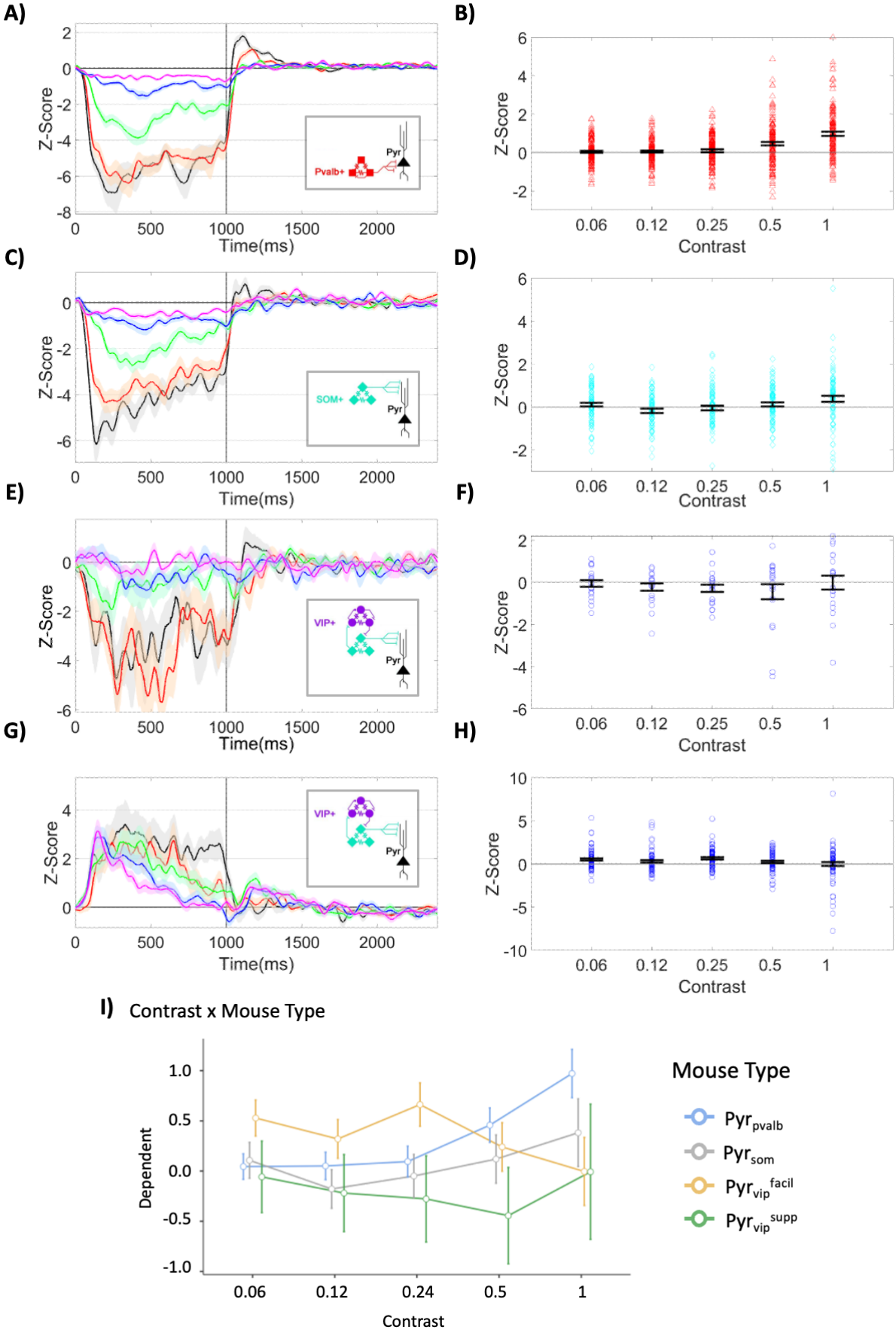
A)
B)
C)
D)
E)
F)
G)
H)
Z-Score
Time(ms)
Contrast
Pvalb+
SOM+
VIP+
Pyr
I) Contrast x Mouse Type
Dependent
Mouse Type
Pyr pvalb
Pyr som
Pyr vip facil
Pyr vip supp

Figure 16: Average Pyr cell rebound effects across mouse types.

(A,C,E,G) Average Z-score functions for (A) Pyr_{pvalb}, (C) Pyr_{som}, (E) Pyr_{vip}^{supp}, (G) Pyr_{vip}^{facil} populations at 6% (magenta line), 12% (blue line), 24% (green line), 50% (red line), and 100% contrast levels (black line). Shading around each Z-score trace indicate SEM. Inset wiring diagram indicates the interneuron photostimulated via the cell-type name written. (B,D,F,H) Time averaged Z-scores across each contrast level for (B) Pyr_{pvalb}, (D) Pyr_{som}, (F) Pyr_{vip}^{supp}, (H) Pyr_{vip}^{facil} populations, respectively. Error bars indicate SEM. (I) Estimated marginal means for rebound size across contrast levels in each Pyr cell population. Blue, grey, green, and yellow colours indicate estimated marginal means for Pyr_{pvalb}, Pyr_{som}, Pyr_{vip}^{supp}, Pyr_{vip}^{facil} populations, respectively. Error bars indicate SEM.

The large dispersion of time-average Z-scores in Figures 16b,d,f,h and large error bars in Figure 16i indicated that rebounds at all contrast levels had highly variable magnitudes. To better visualize variability in rebound size between Pyr cells and across contrasts within a dataset we represented Z-score functions as heatmaps, then sorted all cells within Pyr_{pvalb}, Pyr_{som}, Pyr_{vip}^{supp}, Pyr_{vip}^{facil} populations by the rebound size at 100% contrast (Figures 17a,18a,19a,20a). Each cell number represented an individual Pyr neuron, plotted in a consistent row across the 5 heatmaps for the different contrast stimuli, to depict the within-neuron variability in rebound size between stimulus conditions. Pyr_{pvalb} cells that generated rebounds in the 100% contrast heatmap did not always generate rebounds in 50% contrast heatmaps (Figure 17a), providing evidence for within-neuron variability in rebound magnitude. Pyr_{som} and Pyr_{vip}^{supp} cells produced only weak and inconsistent rebounds at contrast levels $\leq 50\%$ (Figures 18a,19a). To determine if rebound size at one contrast level could predict rebound size at other levels we created a correlation matrix of time-averaged rebound magnitude (1050-1400 ms) for each dataset. All the correlations within the Pyr_{pvalb}, Pyr_{som}, Pyr_{vip}^{supp} datasets were weak, with most being not statistically significant (Figures 17b,18b,19b). However, Pyr_{vip}^{facil} cells showed strong inverted rebounds specifically at lower contrast levels and a moderate correlation between rebound sizes at 6% and 12% contrast (Figure 20b). Across-neuron variability within a dataset was evident over the rows within the heatmap of each stimulus contrast. For 100% contrast, positive rebounds in the post-photostimulation epoch were visible as a yellow streak near the bottom of each heatmap around 1100ms that were especially prevalent in the Pyr_{pvalb} population (Figures 17a,18a,19a,20a). However, corresponding blue streaks near the top of these same heatmaps depict Pyr cells that continued to be suppressed in the post-photostimulation epoch (inverted rebounds; Figure 17a,18a,19a,20a), which provides clear evidence of across-neuron variability. To further visualize across-neuron variability, we split all sorted neurons from 100% contrast heatmaps into 4 quartiles and represented this data as 4 separate average Z-score functions for Pyr_{Pvalb} (Figures 17c-f), Pyr_{som} (Figures 18c-f), Pyr_{vip}^{supp} (Figures 19c-f), and Pyr_{vip}^{facil} populations (Figures 20c-f). All suppressed Pyr cell groups showed strong rebounds of similar strength in quartile 4 (Figures 17f,18f,19f). However, only Pyr_{Pvalb} and Pyr_{som} cells produced visible rebounds in quartile 3 (Figures 17e,18e) and no

suppressed Pyr cell population did so for quartiles ≤ 2 (Figures 17c-d, 18c-d, 19c-d). Interestingly, all suppressed Pyr cell groups showed inverted rebounds in quartile 1 (Figures 17c,18c,19c). For Pyr_{Pvalb} quartile data, suppression during the photostimulation epoch appeared strongest in quartile 4 where Pyr cell rebound effects were also strongest (Figures 17c-f). However, this trend between suppression and rebound size from both epochs at 100% contrast was not observed for Pyr_{som} (Figures 18c-f) or Pyr_{vip}^{supp} cells (Figures 19c-f). To quantify this observation, we correlated the magnitude of suppression during the photostimulation epoch with rebound size during the post-photostimulation epoch. Indeed, there was a significant negative correlation between suppression and rebound magnitude for Pyr_{Pvalb} cells ($r = -0.41$; $p = 1.3 \times 10^{-7}$), but not for Pyr_{som} ($r = 0.02$; $p = 0.86$) or Pyr_{vip}^{supp} cells ($r = 0.34$; $p = 0.14$). Conversely, Pyr_{vip}^{facil} cells produced positive inverted rebounds in quartile 4 (Figure 20f) and negative rebounds in quartile 1 (Figure 20c). However, facilitation during the photostimulation epoch was relatively similar strength for all 4 quartiles (Figures 20c-f), so there was no correlation between facilitation during the photostimulation epoch and rebound size during the post-photostimulation epoch ($r = 0.12$; $p = 0.28$).

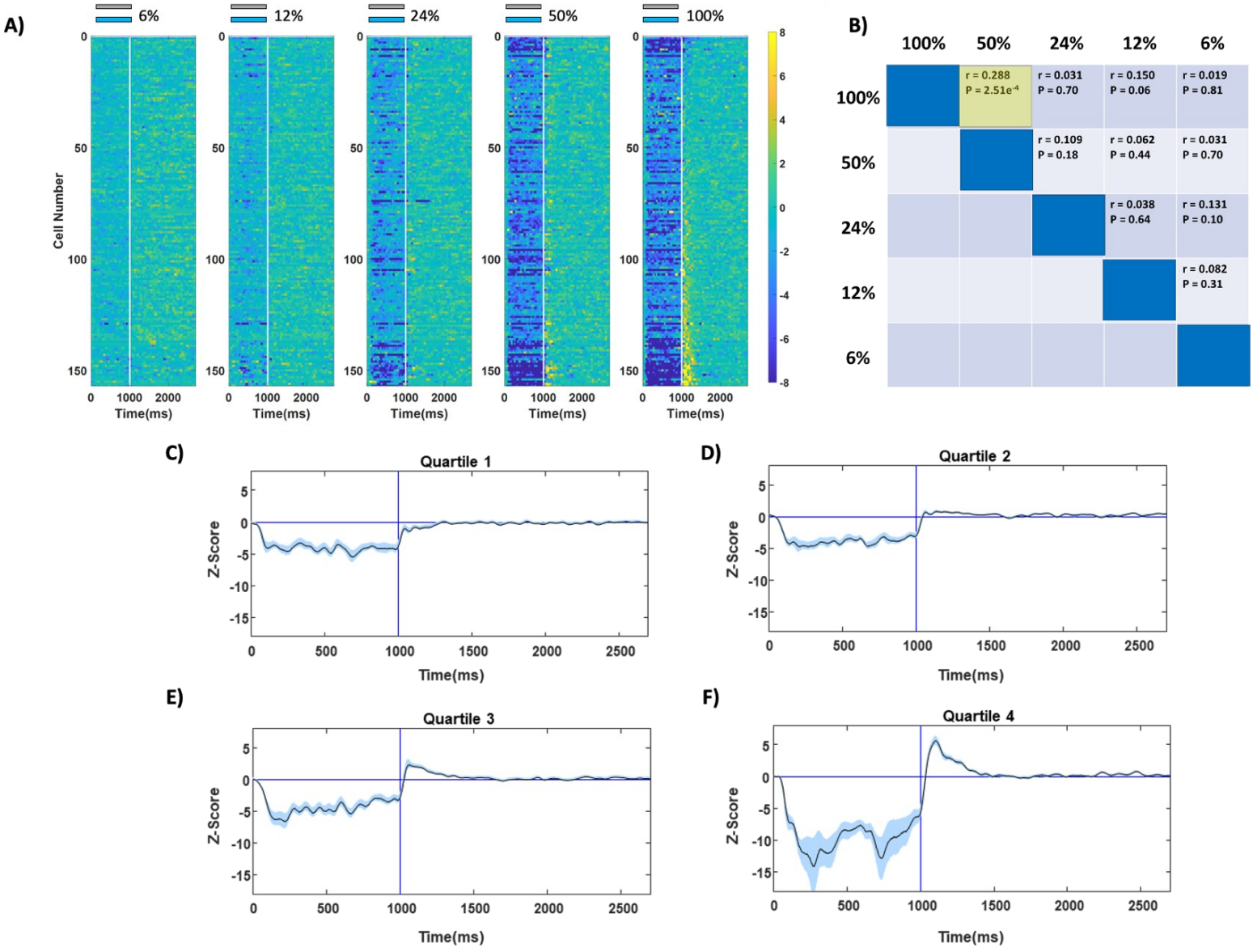

Figure 17: Assessing within- and across-neuron variability of rebound size in Pyr$_{Pvalb}$ cells.

(A) Population heatmaps depicting Pyr cell Z-scores over time for each stimulus. Pyr cells are sorted by rebound magnitude at 100% contrast, so each Z-score row across all five heatmaps belong to a single cell. Z-scores were represented as yellow and blue to indicate facilitation or suppression relative to spontaneous firing, respectively. Grey and blue bars above heatmaps indicate the timing of visual stimulation and photostimulation (B) Correlation matrix comparing the time averaged rebound magnitude between all contrast levels. (C-F) Pyr cell activity (black trace) averaged during photostimulation and post-photostimulation epochs for all neurons belonging to the first (C), second (D), third (E), and fourth quartiles (F) from 100% contrast heatmap in *A*. Blue shading surrounding black trace indicates SEM.

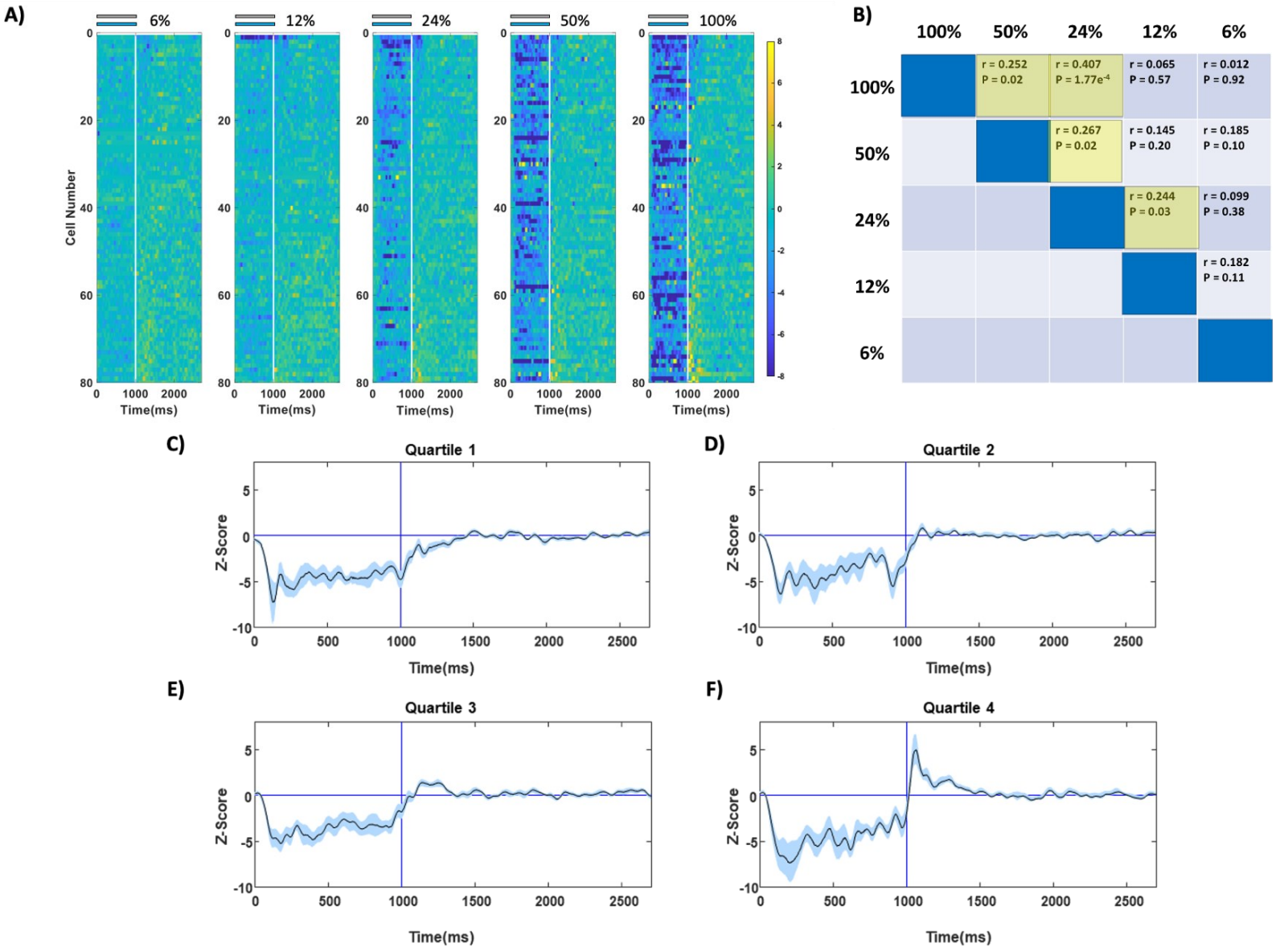

Figure 18: Assessing within- and across-neuron variability of rebound in Pyr_{som} cells.

Description for figures 18a-f is identical to figure 17a-f, but for Pyr_{som} cells.

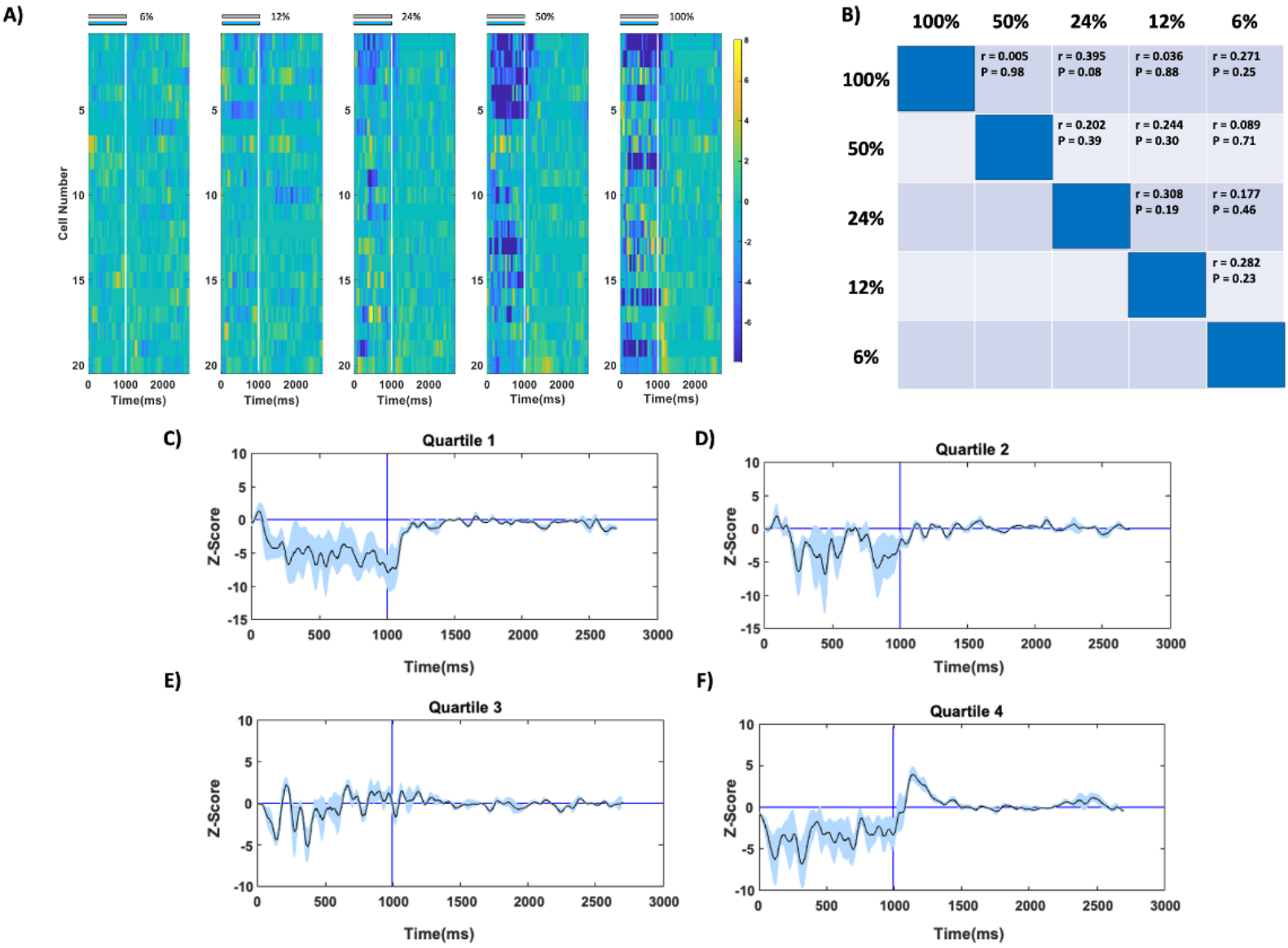

Figure 19: Assessing within- and across-neuron variability of rebound size in Pyr_{vip}^{supp} cells.

Description for figures 19a-f is identical to figure 17a-f, but for Pyr_{vip}^{supp} cells.

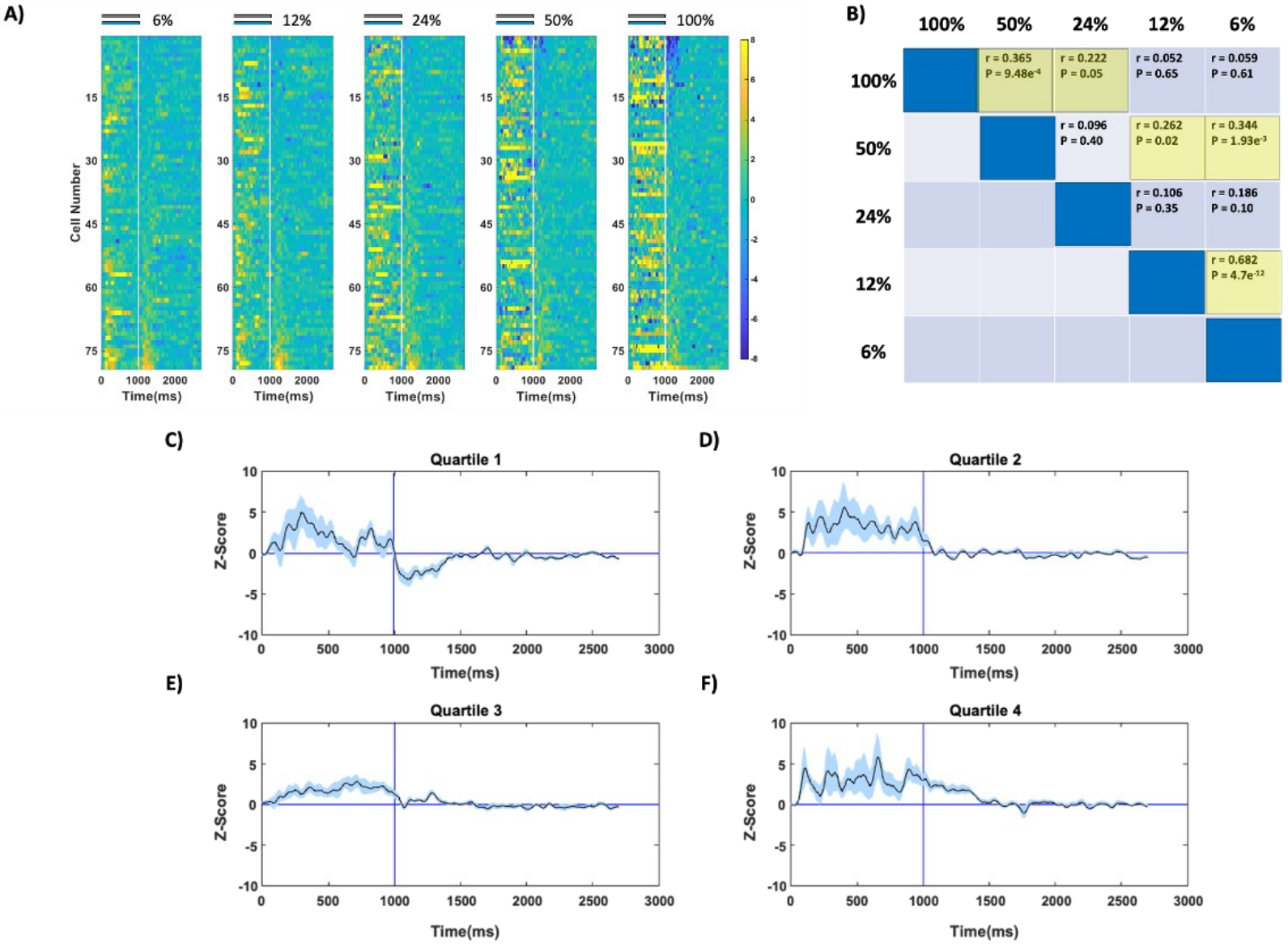

Figure 20: Assessing within- and across-neuron variability of rebound size in Pyr_{vip}^{facil} cells.

Description for figures 20a-f is identical to figure 17a-f, but for Pyr_{vip}^{facil} cells.

2.3.1.2 Interneuron Rebound Effects

The rebounds we observed in our Pyr populations (Figures 12-20) provided an important elaboration on previous work [147], so we applied a similar analysis to the photostimulated *ChR2*-expressing interneurons themselves, which have received relatively little attention regarding rebound effects. Thus, we investigated whether afferent drive level in V1 could elicit rebounds, or affect their magnitude, in the directly photostimulated Pvalb+, SOM+, or VIP+ interneurons recorded during experiment 1. Like Pyr cells, each interneuron subtype showed incrementally larger spike rates to higher contrasts in their control SDFs (Figures 21-23). During photostimulation, the example Pvalb+ cell showed relatively larger increases in firing rates over the control SDF at low contrasts, which has been described as a saturating additive process (Figure 21a-e)[106]. This pattern of modulation produced Z-scores that were relatively less positive at high contrast levels (Figure 21i-j), but it was also evident that the amount of facilitation waned over the photostimulation epoch. Directly after cortical illumination and visual stimulation are terminated at the two highest contrast levels, spike rates in the photostimulation SDF decreased faster than the control SDF (Figure 21d-e), which produced a transiently negative Z-score creating a negative pointing rebound effect (neg-rebound; figure 21i-j). A smaller magnitude neg-rebound is shown for the example SOM+ (Figure 22) and VIP+ interneurons (Figure 23).

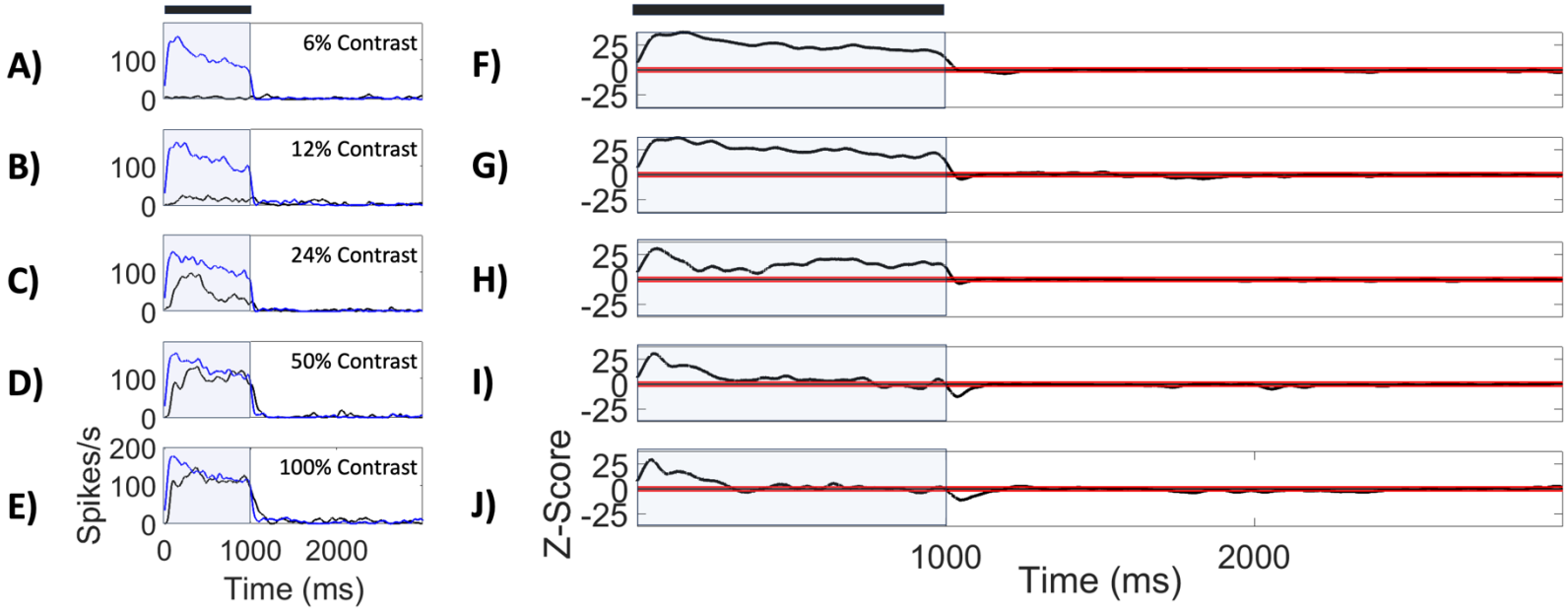

Figure 21: Single photostimulated Pvalb+ cell recorded from a Pvalb-Ai32 mouse.

(A-E) SDFs indicating a single Pvalb+ cell's firing during control (black) and optogenetic conditions (blue), spanning 6-100% contrast levels. The blue shaded area (0-1000 ms) superimposed over the SDF indicates the duration of photostimulation, which temporally overlapped with visual stimulation (dark grey bar). The white area (1001-3000 ms) indicates the post-photostimulation epoch. (F-J) Z-score functions (black lines) derived from SDFs at corresponding contrast levels. The horizontal lines (red) below and above the zero-line indicate a Z-score of ±2. The blue shaded area (0-1000 ms) superimposed over the Z-score function indicates the duration of photostimulation, which temporally overlapped with visual stimulation (dark grey bar).

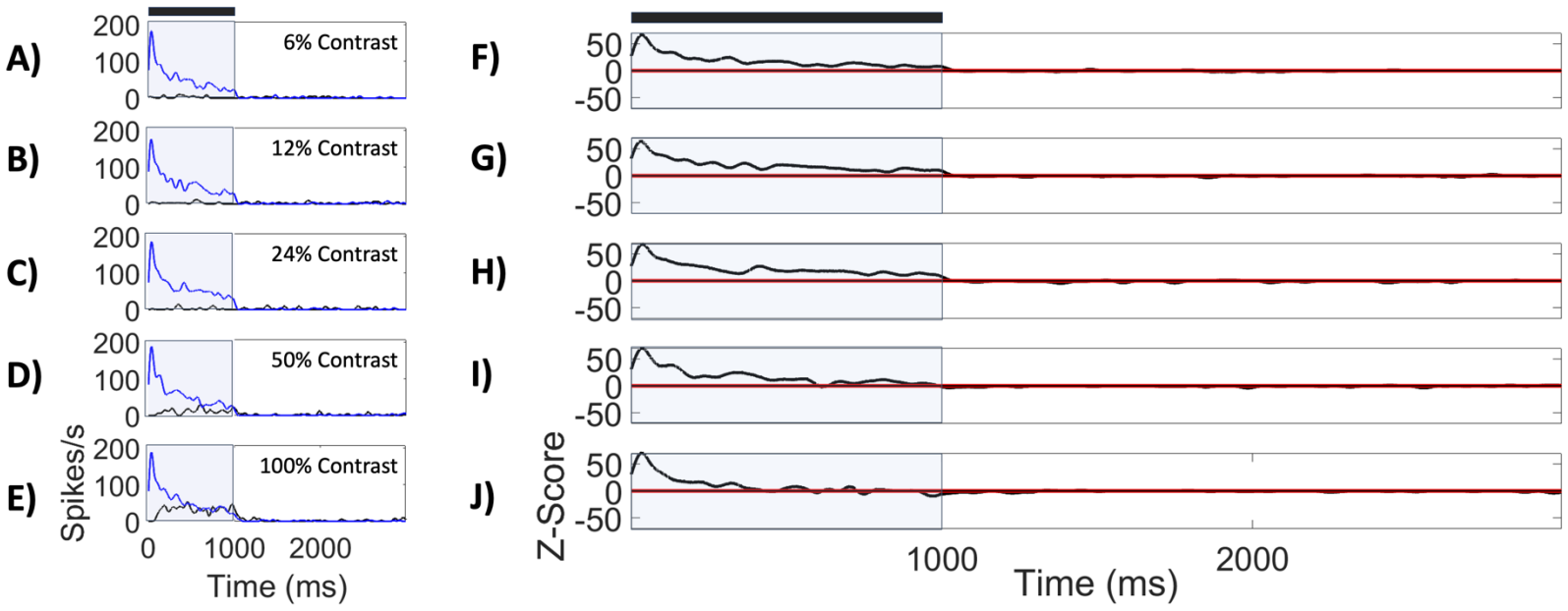

Figure 22: Single photostimulated SOM+ cell recorded from a Som-Ai32 mouse.

(A-E) Same layout as figure 21, but for a photostimulated single SOM+ cell.

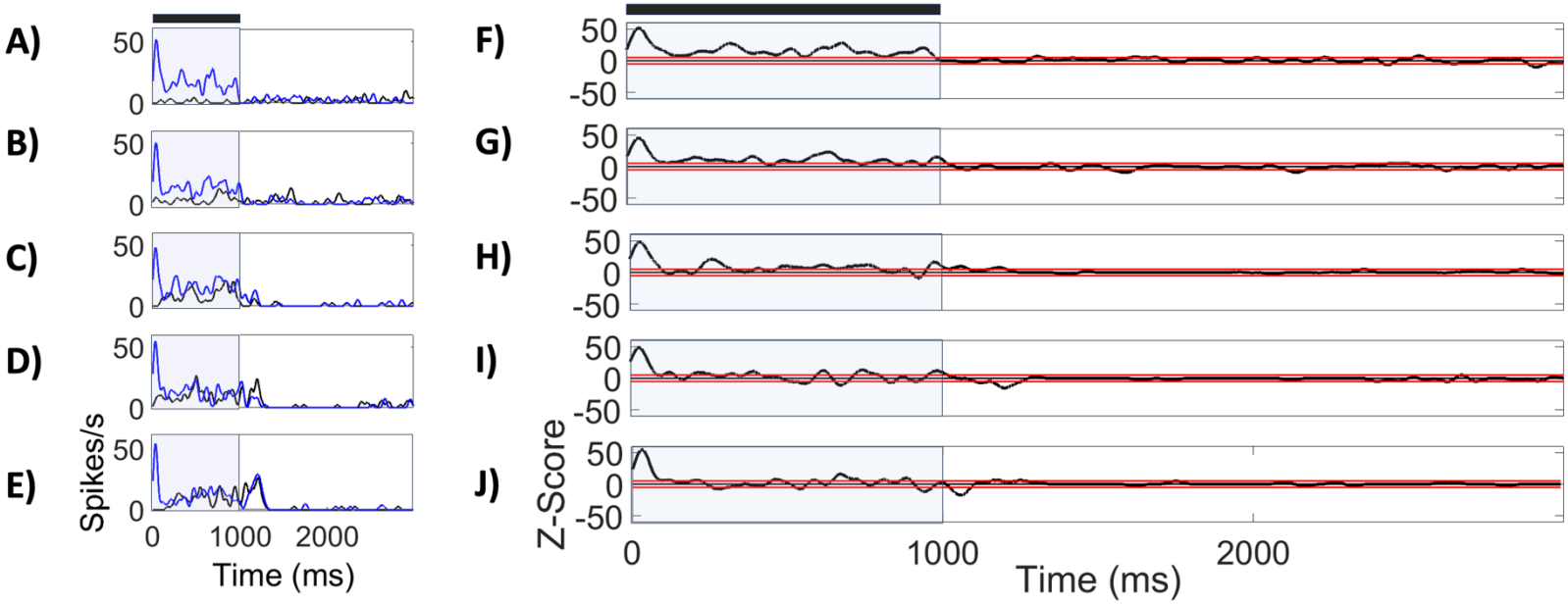

Figure 23: Single photostimulated VIP+ cell recorded from a Vip-Ai32 mouse.

(A-E) Same layout as figure 21, but for a single photostimulated VIP+ cell.

We initially visualized rebound effects in each interneuron group using population average Z-score functions (Figure 24a,c,e). Pvalb+ and SOM+ population data showed similar trends to their example cells across contrast levels (Figure 24a-d), with high contrast Z-score traces during the photostimulation epoch waning faster and more strongly compared to lower contrast levels. In the post-photostimulation epoch, neg-rebounds were produced specifically after 100% contrast stimuli that generated the most afferent drive in V1 (Figure 24a,c). However, the population average interneuron neg-rebounds to 100% contrast appeared sharper and deeper for Pvalb+ compared to SOM+ interneurons (Figure 24a,c). Conversely, VIP+ facilitation seen at high and low contrast levels were more similar, with no average VIP+ Z-score traces exhibiting a neg-rebound (Figure 24e). We quantified the magnitude of rebounds in individual Pvalb+, SOM+, or VIP+ interneurons by calculating the time-averaged Z-score from 1010-1100ms at each contrast, then incorporated population data for each cell-type group into scatter column plots (Figure 24b,d,f). Pvalb+ and SOM+ scatter column plots showed neg-rebound magnitude becoming increasingly negative with stimulus contrast (Figure 24b,d), but this rebound trend was not observed in VIP+ cells (Figure 24f). Time-averaged Z-scores were variable in size across all interneuron datasets, showing positive and negative Z-scores at all contrast levels. We incorporated all interneuron datasets into a mixed model ANOVA comparing the effect of contrast level (within group) and mouse type (between groups) on mean neg-rebound size, which showed a significant main effect for interneuron neg-rebounds differing between contrast levels [$F(2, 8) = 2.73$; $p = 1.6 \times 10\text{-}5$; $N = 88$] but did not significantly differ between mouse types [$F(4, 8) = 2.99$; $p = 0.071$; $N = 88$] and no significant interaction between contrast levels and mouse types [$F(8) = 1.05$; $p = 0.397$; $N = 88$ Figure 24g]. Estimated marginal means for interneuron subtypes across contrasts showed that rebounds in Pvalb+ and SOM+ were quite similar, but VIP+ rebounds were too variable to distinguish from the other 2 subtypes (Figure 24g). Overall, some Pvalb+ and SOM+ interneurons produced strong neg-rebounds after prior photostimulation was paired with the highest contrast stimuli generating the most afferent drive in V1 (Figures 24a-d,g), while rebounds in VIP+ cells were quite inconsistent and weak (Figures 24e-g).

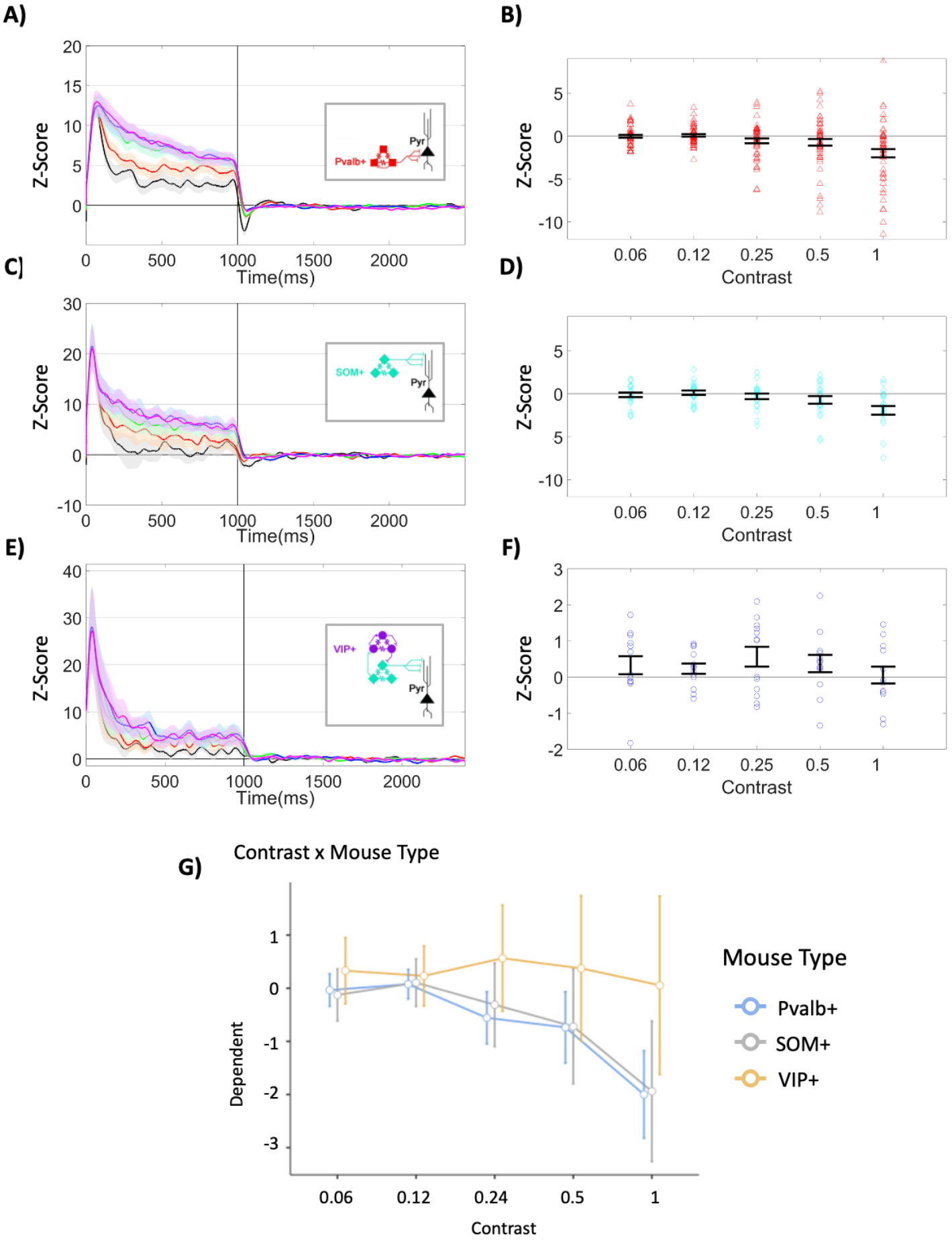
A)
B)
C)
D)
E)
F)
G)
Z-Score
Time(ms)
Pvalb+
SOM+
VIP+
Pyr
Contrast
Contrast x Mouse Type
Dependent
Mouse Type
Pvalb+
SOM+
VIP+
0.06
0.12
0.24
0.25
0.5
1

Figure 24: Average interneuron negative-rebound effects across mouse types.

(A,C,E) Average Z-score traces for Pvalb+, SOM+ and VIP+ interneurons, respectively. Lines show 6% (magenta line), 12% (blue line), 24% (green line), 50% (red line), and 100% contrast levels (black line). Shading around each Z-score trace indicate SEM. Inset wiring diagram indicates the interneuron photostimulated via the cell-type name written. (B,D,F) Time averaged Z-score for individual interneurons across the 5 contrast levels for Pvalb+, SOM+ and VIP+ interneurons, respectively. Error bars indicate SEM. (G) Estimated marginal means for rebound size across contrast levels in each interneuron population. Error bars indicate SEM.

The large dispersion of time-average Z-scores in Figures 24b,d,f and large error bars in Figure 24g indicated neg-rebounds at all contrast levels had highly variable magnitudes, so we used population heatmaps to further examine within- and across-interneuron variability amongst each dataset (Figures 25a,26a,27a). Pvalb+ cells that produced neg-rebounds at 100% contrast sometimes generated neg-rebounds at lower contrast levels (Figures 25a), which produced statistically significant weak or moderate correlations between contrast levels in time-averaged neg-rebound magnitude correlation matrix (Figures 25b). However, Pvalb+ cells producing neg-rebounds at contrast levels < 100% mostly did at either 24% or 50% contrast and not both (Figure 25a), providing evidence for moderate within-neuron variability in rebound magnitude. Conversely, SOM+ and VIP+ interneurons showed weak and inconsistent neg-rebounds at contrast levels < 100% (Figures 26a,27a) and mostly produced weak, not statistically significant correlations between contrast levels (Figures 26b,27b). Across-neuron variability was seen in 100% contrast heatmaps, where for Pvalb+ and SOM+ cells neg-rebounds in the post-photostimulation epoch were visible as a blue streak near the top of each heatmap around 1050ms that were especially prevalent in Pvalb+ data (Figures 25a,26a). However, several Pvalb+ cells at the bottom of Figure 25a generated positive Z-scores indicating inverted rebounds. Conversely, VIP+ cells in their 100% contrast heatmap rarely generated clear neg-rebounds (Figures 27a). Across-neuron variability was further visualized for each interneuron population with quartile average Z-score functions from 100% contrast responses for Pvalb+, SOM+, or VIP+ cells (Figures 25c-f, 26c-f, 27c-f). All interneuron groups produced their largest neg-rebounds in quartile 1 (Figures 25c,26c,27c) but were the deepest and most pronounced in Pvalb+ cells (Figure 25c) and most shallow in VIP+ cells (Figure 27c). Pvalb+ and SOM+ cells produced neg-rebounds in quartile 2 (Figures 25d,26d) and only Pvalb+ cells produced neg-rebounds in quartile 3 (Figures 25e). During the photostimulation epoch, optogenetic activation of Pvalb+ and SOM+ interneurons was quite transient in quartiles 1-2, and showed paradoxical suppression in quartile 1 (Figure 25c,d and 26c,d)[106]. Paradoxical suppression was not visible in any quartile trace for VIP+ cells, and subsequent neg-rebounds and inverted rebounds were about equally common, but quite small (Figure 27c-f). When we correlated facilitation during the photostimulation epoch with neg-rebound magnitude at

100% contrast for each interneuron subtype, we found significant positive correlation for Pvalb+ ($r = 0.59$, $p = 2.8 \times 10^{-6}$) and SOM+ cells ($r = 0.54$, $p = 0.012$) but not VIP+ cells ($r = 0.34$, $p = 0.26$).

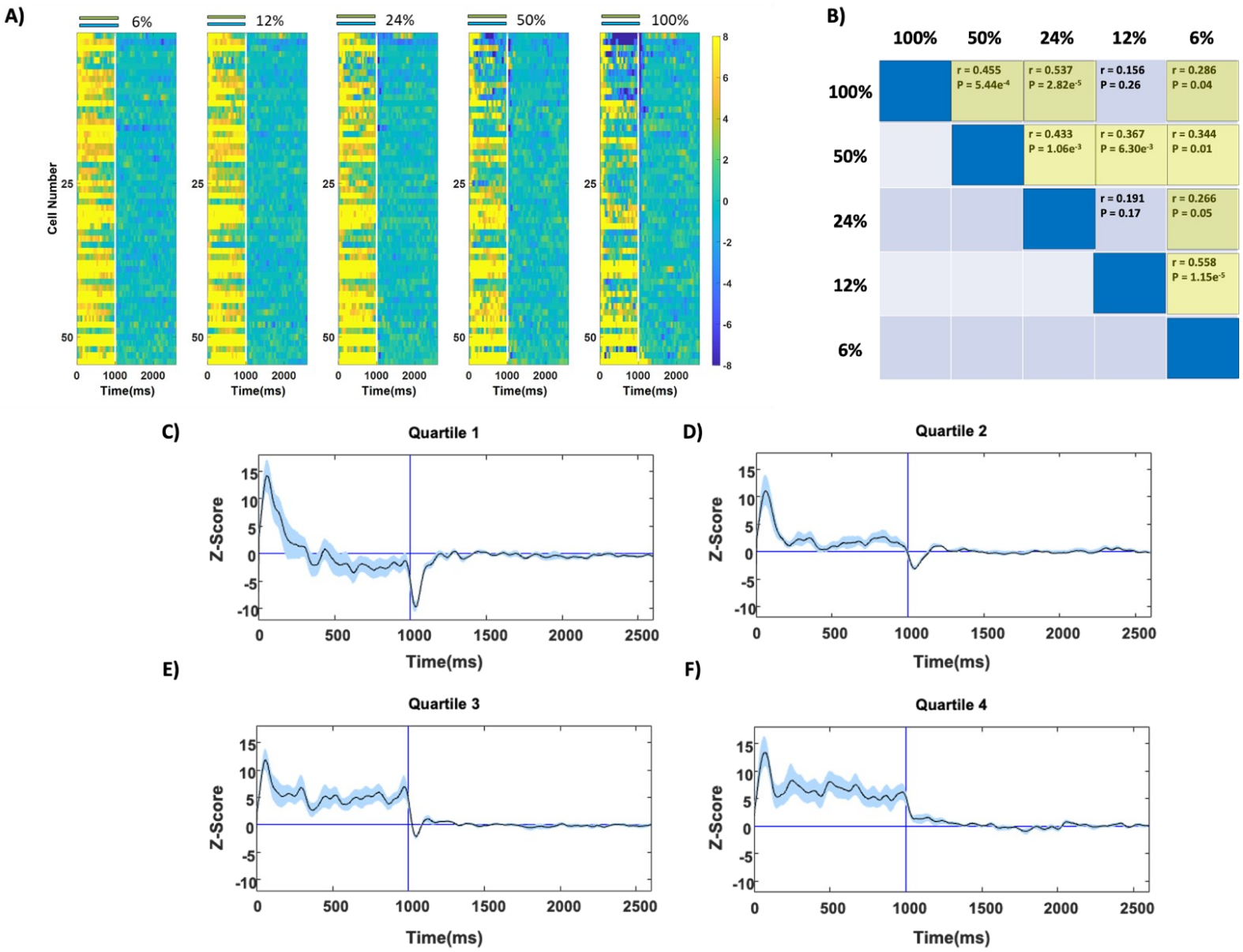

Figure 25: Assessing within- and across-neuron variability of negative-rebound size in Pvalb-Ai32 Pvalb+ interneurons.

(A) Population heatmaps depicting Pvalb+ interneuron Z-scores over time for each stimulus. Pvalb+ cells are sorted by rebound magnitude at 100% contrast, so each Z-score row across all five heatmaps belong to a single cell. Z-scores were represented as yellow and blue to indicate facilitation or suppression relative to spontaneous firing, respectively. (B) Correlation matrix comparing time-averaged neg-rebound magnitude between all contrast levels. (C-F) Quartile data derived from 100% contrast heatmap represented as Z-score functions. Pvalb+ cell activity (black trace) averaged for all interneurons belonging to the first (C), second (D), third (E), and fourth quartiles (F). Blue shading surrounding black trace indicates SEM.

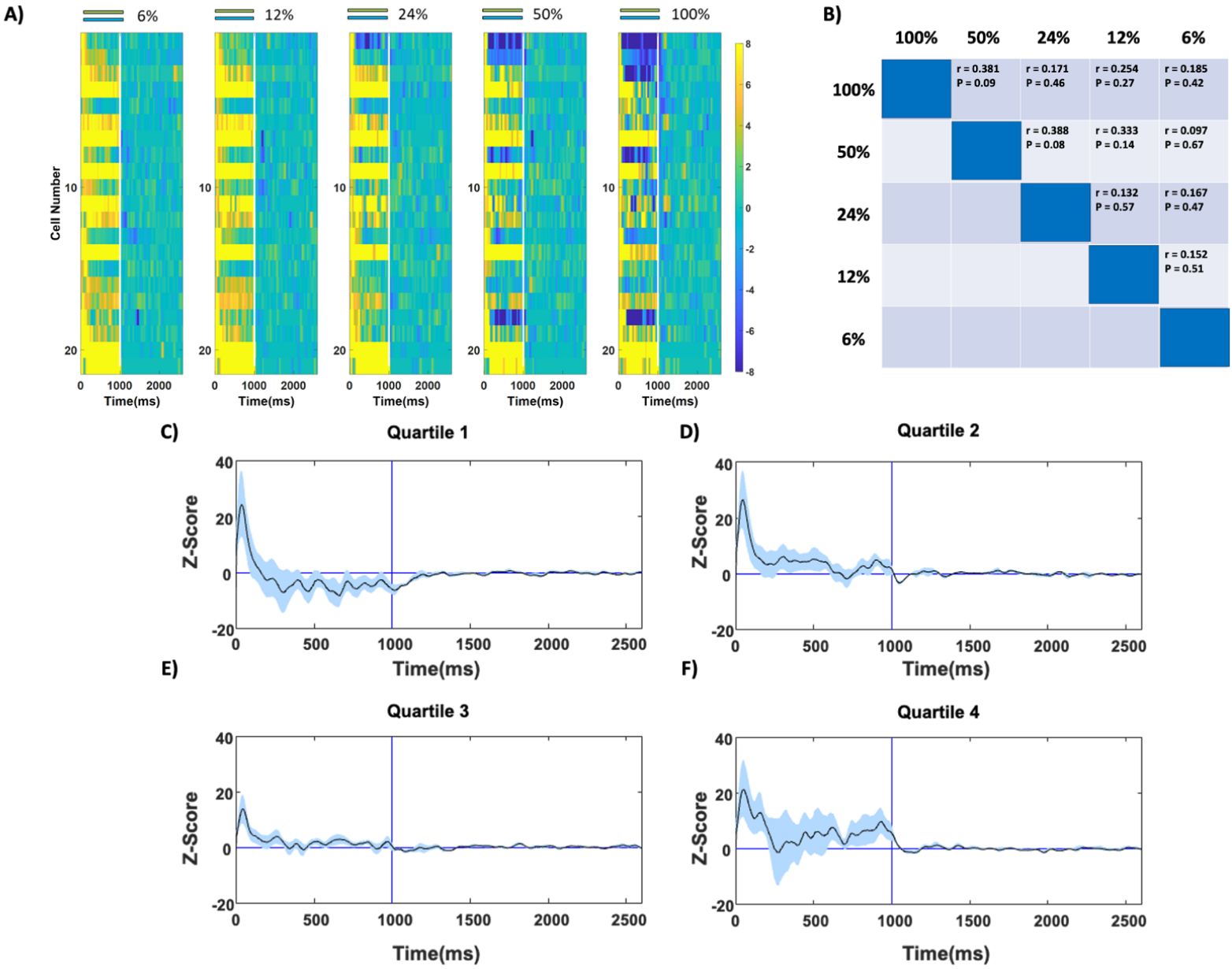

Figure 26: Assessing within- and across-neuron variability of negative-rebound size in Som-Ai32 SOM+ interneurons.

Description for figures 26a-f is identical to figure 25a-f, but for Som-Ai32 SOM+ cells.

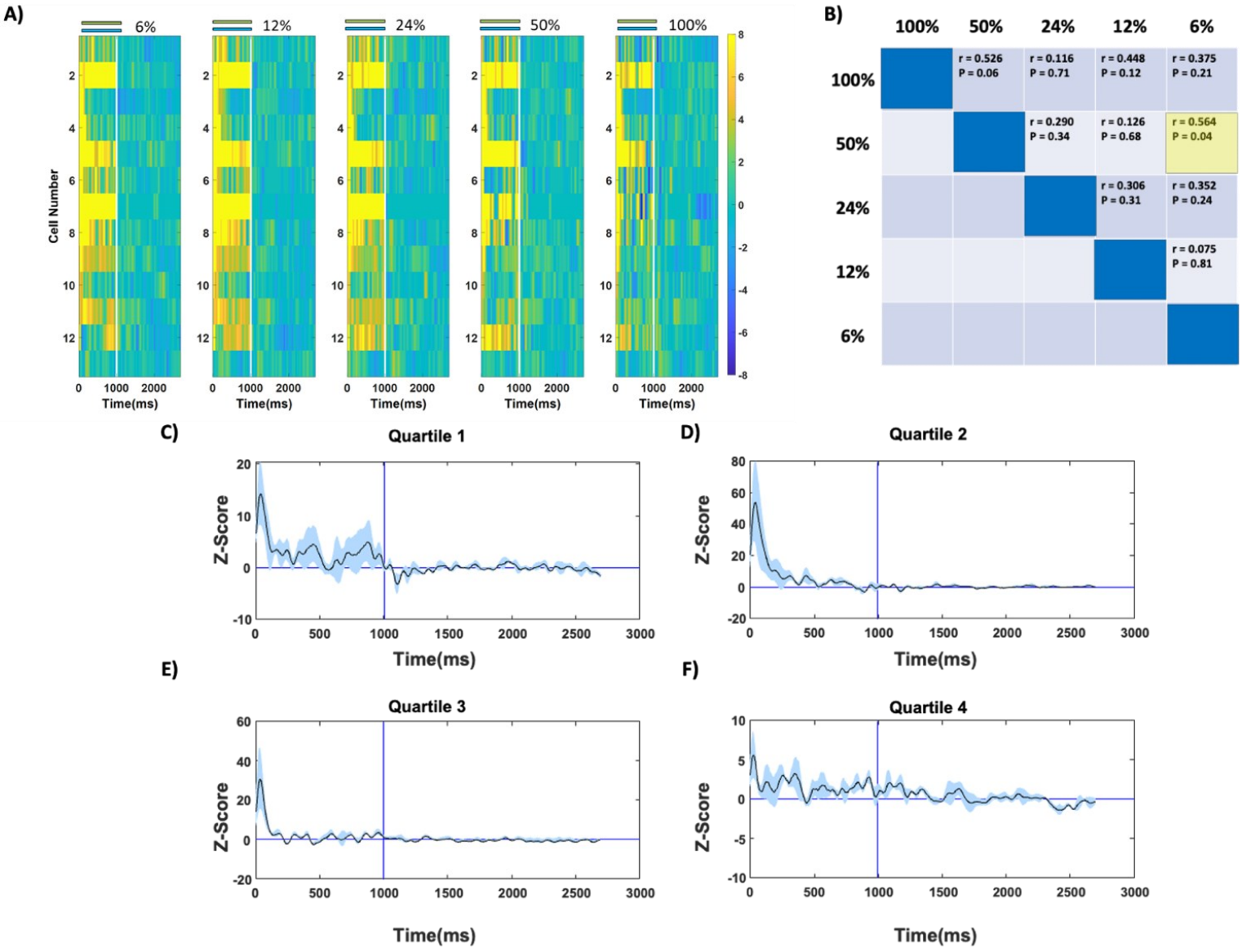

Figure 27: Assessing within- and across-neuron variability of negative-rebound size in Vip-Ai32 VIP+ interneurons.

Description for figures 27a-f is identical to figure 25a-f, but for Vip-Ai32 VIP+ cells.

2.3.1.3 Comparing Pyr and Interneuron Rebound Effect Latencies

The most obvious disparity between rebound effects in our Pyr (Figures 12-20) and interneuron populations (Figures 21-27) was the difference in directionality. However, considering Pyr cells and interneurons are reciprocally connected (Figure 11a)[42], and photomodulation latencies are shorter in *ChR2*-expressing interneurons than Pyr cells (Figure 11e-g), we speculated interneuron neg-rebounds may occur before Pyr cell rebounds. At 100% contrast, Pvalb+ and SOM+ interneurons very rapidly reached negative Z-score values after light offset (Figures 24a,c, 25c-e, 26c-d), whereas suppressed Pyr cells did not reach positive Z-score values until after some delay (Figure 16a,c,e, 17d-f, 18e-f, 19f). To isolate this difference in timing we elected to examine the latency to rebound peak only in a subset of neurons that gave strong rebounds by selecting the top half of each dataset that produced the largest rebound amplitudes to 100% contrast gratings. Independent sample T-Tests indicated that the neg-rebounds produced by Pvalb+ and SOM+ interneurons reached their peak significantly earlier than the rebounds produced by Pyr_{pvalb} [T (104) = 5.98; p = 3.1 × 10-8; N = 106; Figure 28a)] and Pyr_{som} cells [T (49) = 3.39; p = 0.001; N = 51; Figure 28b)]. Despite VIP+ cells not producing large rebound effects (Figure 24e-g, 27) we still examined the difference in latencies between VIP+ neg-rebounds with Pyr_{vip}^{supp} and Pyr_{vip}^{facil} cell rebounds. A Welch's ANOVA indicated there was no significant difference in the timing between these rebound effects in Vip-Ai32 mice [F (2, 13.5) = 0.394; p = 0.682; N = 56; Figure 28c)].

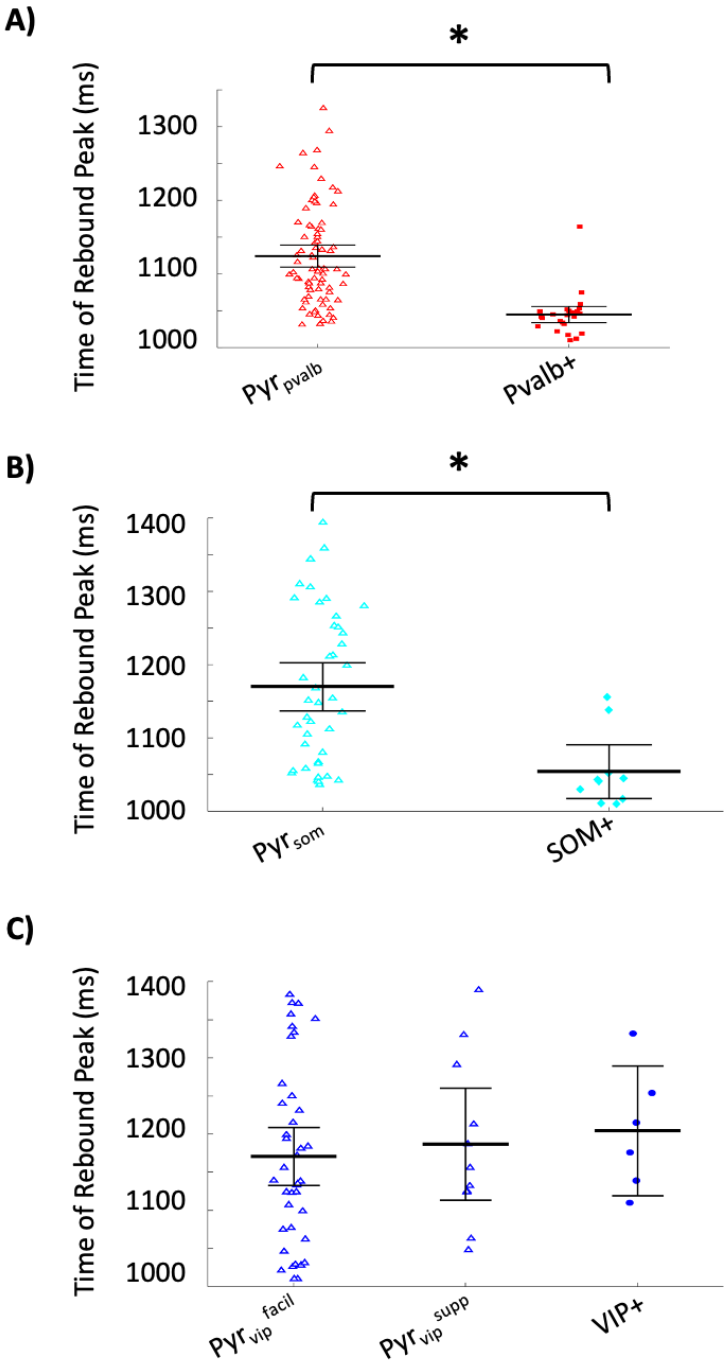

Figure 28: Comparing Pyr cell and interneuron rebound latencies.

Scatter-column plots comparing Pyr cell and interneuron rebound effect latencies in (A) Pvalb-Ai32, (B) Som-Ai32, (C) Vip-Ai32 mice. Latencies were determined by calculating time to rebound peak (ms). Thick horizontal lines indicate population mean, and error bars indicate SEM. Asterisks denote a significant difference.

2.3.2 Experiment 2

Having observed that the contrast level of visual stimuli driving V1 neurons during interneuron photostimulation affects Pyr cell rebound magnitudes after light offset (Figures 12-20), we then sought to determine whether other visual stimuli that differentially drive V1 activity could have a similar effect on rebound size. Therefore, in experiment 2 we paired interneuron photostimulation with vertically oriented black or white bars that were randomly flashed within or outside V1 RFs (Figure 29a). Considering Pyr cell rebounds in experiment 1 were strongest and most abundant from Pvalb+ photostimulation (Figure 16), we decided to conduct these experiments solely in Pvalb-Ai32 mice and collected data from 143 Pyr cells.

We first compared control and photostimulated SDFs at all nine spatial positions for black or white flashed bars. In our example complex cell in Figure 29b we measured responses to flashed white bars across its RF. In the control condition, bars flashed within the RF elicited robust onset responses and sometimes offset responses to the appearance and disappearance of the bar, respectively. Spiking responses were much weaker when bars were flashed closer to the edges of the RF, and bars flashed outside the RF only elicited spontaneous firing (Figure 29b). During photostimulated trials, onset responses were attenuated when the cortex was illuminated, but spike rates in the post-photostimulation epoch were potentiated at bar positions inside the RF (Figure 29b). We converted SDFs into Z-score functions, such that suppression during the photostimulation epoch produced negative Z-scores, and rebounds during the post-photostimulation epoch produced transient positive Z-scores (Figure 29c).

To examine whether afferent drive during the photostimulation epoch affected later rebound size, for each cell we compared the Z-score function produced by the bars flashed inside the RF that generated the strongest visual response with a Z-score function produced by bars flashed outside the RF generating the weakest visual response (Figure 29d). Across the population, we compared Z-score functions inside and outside the RF in response to black bars for 139 Pyr cells and to white bars for 143 Pyr cells. Figure 29e-f plots the population average Z-score functions for white and black bars, respectively. The population showed robust rebounds following light offset (rebound peak ≈ 2 Z-score) for both white and black bars flashed inside the RF (blue trace), but not for bars flashed

outside the RF (black trace; Figure 29e-f). We quantified the difference in rebounds produced by bars flashed inside vs. outside the RF by comparing the time-averaged Z-scores between 700 and 900 ms, which appeared to be the period rebounds were largest. Most Pyr cells had larger time-averaged Z-scores when bars were flashed inside the RF (Figure 29g; grey lines), and this was also reflected by the population means (Figure 29g; black lines). A repeated measures ANOVA (bar location [inside RF vs. outside RF] × stimulus polarity [white bars vs. black bars]) showed a main effect of bar location indicating bars flashed inside RFs produced significantly larger rebounds than bars flashed outside RFs [$F(1,1) = 338.695$; $p = 5.2 \times 10\text{-}38$; $N = 281$)], with no evidence of a difference between black and white bars [$F(1,1) = 0.202$; $p = 0.654$; $N = 281$)] or any interaction between bar location and stimulus polarity [$F(1,1) = 3.524$; $p = 0.063$; $N = 281$)]. These results from experiment 2 corroborated our findings from experiment 1, suggesting that increasing afferent drive during the photostimulation epoch potentiates later rebound size during the post-photostimulation epoch.

When comparing Pyr cell rebounds seen in population average Z-score functions for 100% contrast gratings in experiment 1 (Figure 16a,c,e) or flashed bars in experiment 2 (Figure 29e-f), it appeared that there was a difference in peak rebound latency. Rebound peaks appeared to occur sooner following drifting gratings (Figure 16a,c,e) compared to flashed bars (Figure 29e-f). Therefore, we examined latency to rebound peak for Pyr cells stimulated with 100% gratings, black, or white flashed bars. Once again, to ensure we were measuring the peaks of actual rebounds, we analyzed the top half of each dataset that displayed the largest rebound amplitudes. A Fisher's one-way ANOVA showed rebounds to bars occurred significantly later than rebounds to drifting gratings [$F(2, 218) = 16.2$; $p = 2.7 \times 10\text{-}7$; $N = 221$; Figure 29h). Post hoc comparisons using the Tukey HSD tests indicated white and black bar peak rebound latencies did not significantly differ from each other ($MD = -12.1$; $p = 0.411$; $T = -1.27$; $N = 142$), however grating peak rebound latencies were significantly shorter than peak rebound latencies for both black ($MD = 38.1$; $p = 1.5 \times 10\text{-}4$; $T = 4.14$; $N = 149$) and white bars ($MD = 50.1$; $p = 4.9 \times 10\text{-}7$; $T = 5.41$; $N = 151$). This disparity in rebound timing suggests that the nature of afferent drive can produce subtle differences in rebounds.

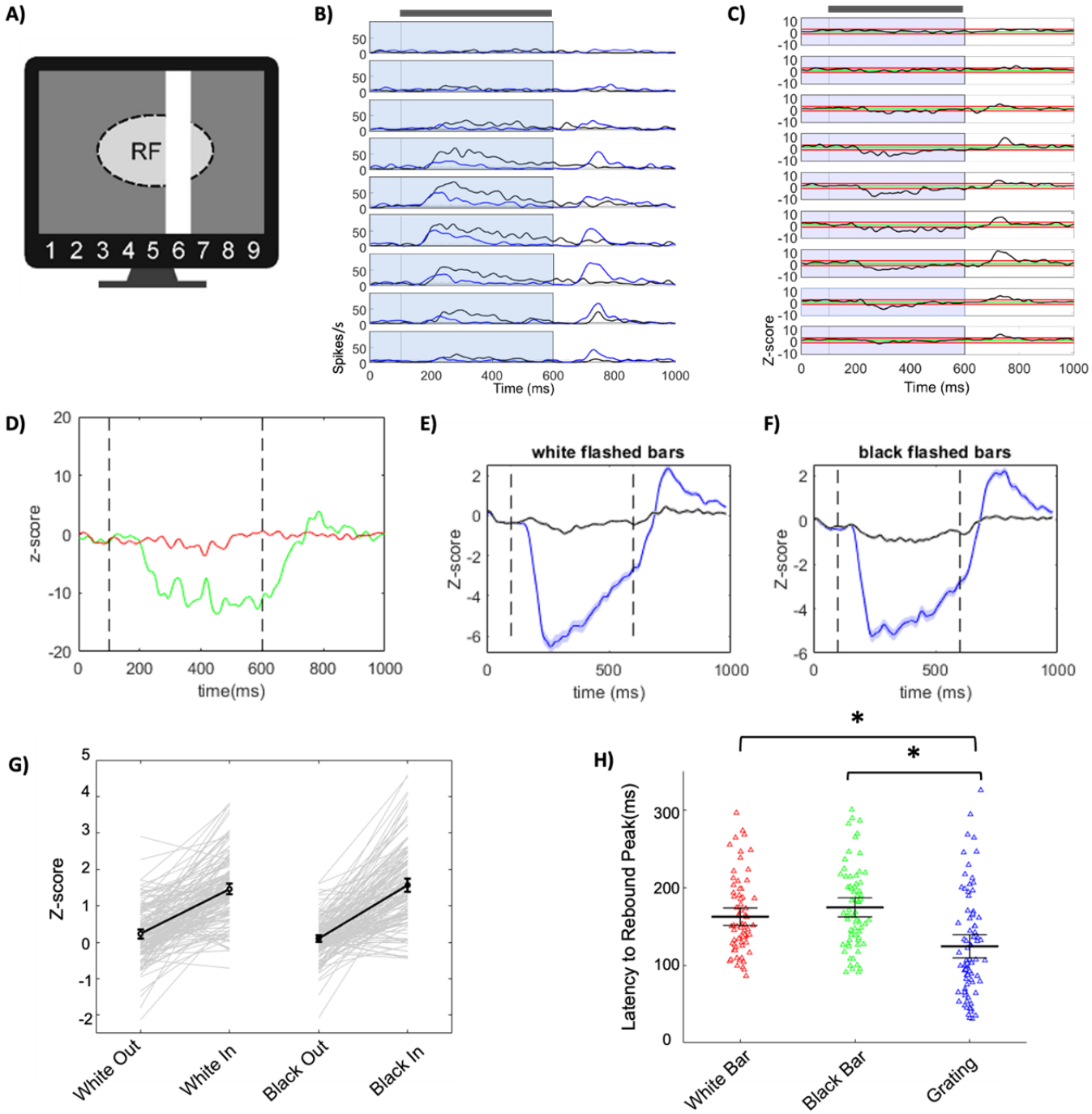
A)
RF
1 2 3 4 5 6 7 8 9
B)
Spikes/s
Time (ms)
C)
Z-score
Time (ms)
D)
z-score
time(ms)
E)
white flashed bars
Z-score
time (ms)
F)
black flashed bars
Z-score
time (ms)
G)
Z-score
White Out
White In
Black Out
Black In
H)
Latency to Rebound Peak(ms)
White Bar
Black Bar
Grating
*
*

Figure 29:Coupling Pvalb+ photostimulation with flashed vertical bar stimuli inside verse outside Pyr cell RFs affects rebound magnitude.

(A) In experiment 2, white or black bars were flashed in positions 1-9, which was coupled with or without Pvalb+ photostimulation. In the example cartoon, a white bar is flashed at position 6 inside the RF (dashed oval). (B) SDFs from an example cell to white bars flashed in spatial locations 1-9 with (blue traces) or without Pvalb+ photostimulation (black traces). Blue shading superimposed over SDF indicates photostimulation timing (0-600ms), whereas the grey bar above the top SDF indicates the timing of the visual stimulus (100-600ms). White area beyond 600ms indicates the post-photostimulation epoch. (C) Z-score functions (black lines) for the example cell from B. The horizontal red lines below and above the green zero-line indicate a Z-score of ±2. (D) Z-score traces indicating the bar position with the strongest (green) and weakest visual response (red) from a single example neuron. (E-F) Average Z-score functions for white (E) and black bars (F). Blue traces indicate the average response to the bar position that elicited the strongest visual response, whereas black traces indicate the average response to bar position that elicited the weakest visual response. Vertical dashed lines indicate when the flashed bar stimulus appeared and disappeared. Shaded regions in E and F indicate SEM. (G) Time-averaged Z-scores (700-900 ms) for white and black bars flashed inside verse outside RFs. Light grey lines indicate show date from individual cells, whereas black line indicates population mean. Circle and error bars in G indicate mean and SEM. (H) Scatter-column plot comparing latency to peak rebound for white bars (red data points), black bars (green data points), and drifting gratings from experiment 1 Pyr cells recorded in Pvalb-Ai32 mice (blue data points). Thick central line and error bars in H indicate mean and SEM.

2.3.3 Experiment 3

A common theme in the design of both experiments 1 and 2 was that the optogenetic photostimulation and visually driven activity both terminated at the same time. We sought to determine whether this co-occurrence was required to produce rebounds, and whether manipulating the level of afferent drive before, during, or after the photostimulation epoch influenced rebound size. We used a factorial design where visually driven neural activity could be high (Hi) or low (Lo) during the photostimulation and post-photostimulation epochs (Figure 30a-d; see *Methods*). For this experiment we again solely collected data in Pvalb-Ai32 mice, and report findings from a population of 134 Pyr and 34 Pvalb+ cells.

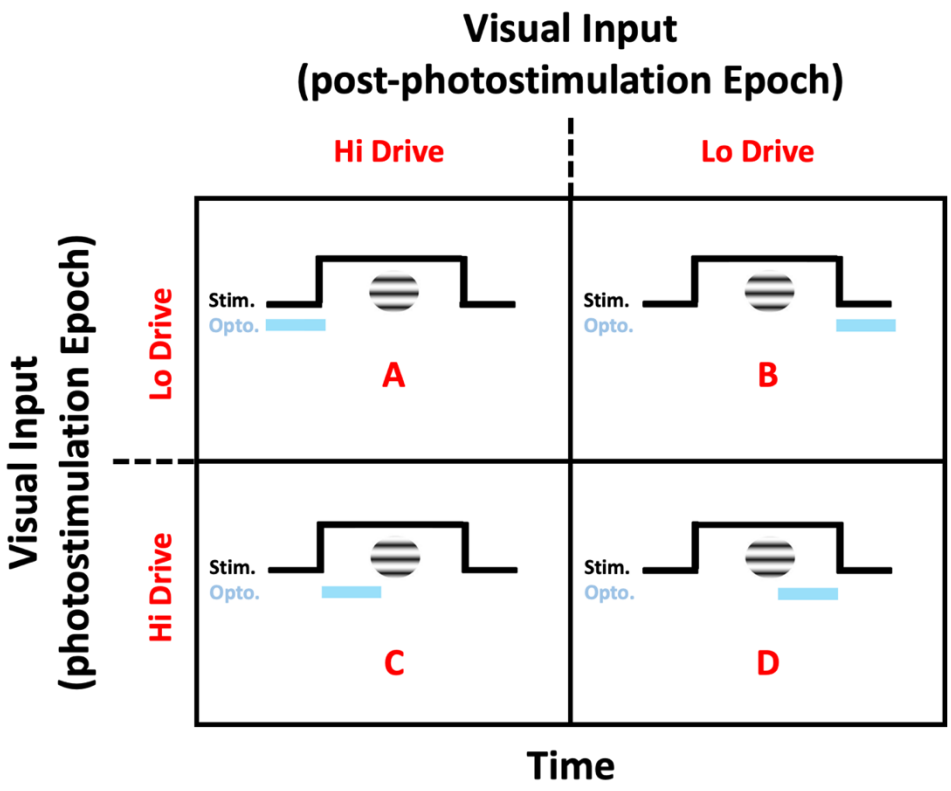

Figure 30:Experiment 3 factorial design.

In this experiment, we coupled high (Hi) or low (Lo) visual drive during the photostimulation epoch with either Hi or Lo visual drive during the post-photostimulation epoch. This produced 4 visual stimulus-photostimulation pairings including (A) LoHi, (B) LoLo, (C) HiHi, and (D) HiLo. Within *A-D*, the step-line surrounding the drifting grating indicates when the visual stimulus was turned on, and the light blue bar underneath indicates when the light for optogenetics was turned on. See *Methods* (*Experiment 3*) for a detailed description of *A-D*.

2.3.3.1 Pyr Cell Rebound Effects.

Experiments 1 and 2 showed converging evidence that rebounds were largest in Pyr_{pvalb} cells following the pairing of strong afferent drive to V1 with photostimulation (Figure 16a-b,17,29), but the effect of afferent drive during the rebound itself was unknown. Therefore, we predicted that conditions where Pvalb+ photostimulation co-occurred with high afferent drive (Figure 30c-d; HiHi and HiLo) should generally produce larger rebounds than conditions where Pvalb+ photostimulation co-occurred with low afferent drive (Figure 30a-b; LoHi and LoLo). However, we were most interested in comparisons between conditions with high vs. low afferent drive during the post-photostimulation epoch. Figures 31a-h shows data from an example Pyr cell with spiking responses in control and photostimulated conditions plotted as SDFs (left column) and Z-score functions (right column) for all 4 conditions. In response to the HiLo condition, which most resembles experiment 1, this Pyr cell showed a small and transient elevation in firing when the visual stimulus and photostimulation simultaneously concluded, which was visualized as a Z-score rebound that was reminiscent of the responses observed in experiment 1 (Figure 31e-f). Rebounds from both HiHi and LoHi conditions with high afferent drive in the post-photostimulation epoch appeared to produce prolonged and complex rebounds (Figure 31a-d). Finally, this cell did not produce measurable rebounds for the LoLo condition, where there was low afferent drive in both photostimulation and post-photostimulation epochs (Figure 31g-h).

We examined all 4 conditions across our population with average Z-score functions (Figure 31i-l). As expected, the population data showed more robust suppression in the photostimulation epoch when it coincided with visual stimulation (HiHi and HiLo), compared to when Pvalb+ activation occurred before (LoHi) or after (LoLo) the visual stimulus. The population average for the LoHi condition showed virtually no change in activity during the post-photostimulation epoch (Figure 31i), potentially because smaller complex rebounds canceled each other out. In comparison, the HiHi condition showed prolonged and complex rebounds after light offset (Figure 31j). Interestingly, population mean HiHi rebounds initially produced small rebounds after light offset that appeared to reach their peak around the time of visual stimulus

offset that occurred 500 ms later. Conversely, mean rebounds in the HiLo condition (Figure 31k) were similar in amplitude to the ones produced for the HiHi pairing but were more transient such that they reached their peak amplitude shortly after visual stimulus offset and faded quickly (Figure 31k). The LoLo condition produced the smallest rebounds (Figure 31l), which were not seen at all in the example cell (Figure 31g-h). To test whether Pyr cell rebounds were significantly impacted by the different levels of afferent drive during both epochs we calculated time-averaged Z-scores between 600 and 1200 ms of the post-photostimulation epoch. A factorial ANOVA (afferent drive in the photostimulation epoch × afferent drive in the post-photostimulation epoch) showed a main effect of afferent drive in the photostimulation epoch indicating rebounds were significantly greater following a period where high visually evoked activity was strongly suppressed by Pvalb+ activation [$F(1, 1) = 9.36$; $p = 0.003$; $N = 134$; Figure 31m]. There was no evidence for a main effect of afferent drive in the post-photostimulation epoch affecting rebound size [$F(1, 1) = 1.56$; $p = 0.213$; $N = 134$; Figure 31m]. However, there was a significant interaction indicating high afferent drive in the photostimulation epoch produced larger rebounds when afferent drive in the post-photostimulation epoch was high too [$F(1, 1) = 4.45$; $p = 0.037$; $N = 134$; Figure 31m]. This interaction appears to mainly be driven by the prolonged rebounds in the HiHi condition (i.e. compare prolonged and transient rebounds in figures 31j and 31k, respectively). The estimated marginal means in Figure 31m showed large error bars especially for HiHi and LoHi conditions (yellow bars) that suggest high variability in rebound size across the population. Pyr cell data in experiment 3 substantiated data in experiments 1-2, demonstrating again that strongly driving V1 during the photostimulation epoch with highly effective visual stimuli increased rebound size after light offset. However, experiment 3 also showed that the co-termination of optogenetic photostimulation and visually driven activity was not required to produce rebounds, and that afferent drive in the post-photostimulation epoch can alter rebound timing and amplitude in complex ways.

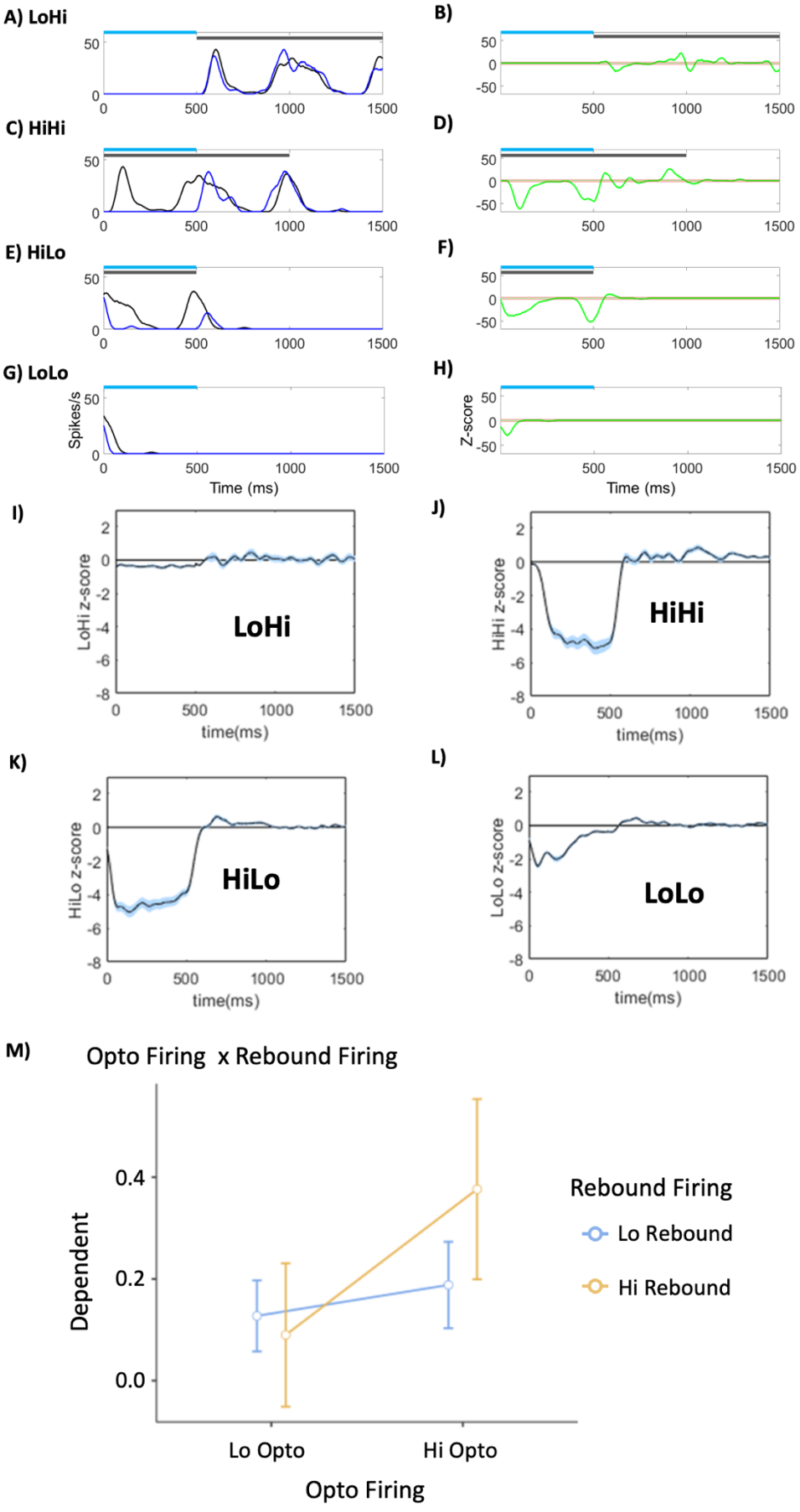
A) LoHi
B)
C) HiHi
D)
E) HiLo
F)
G) LoLo
H)
Spikes/s
Z-score
Time (ms)
I)
J)
LoHi z-score
HiHi z-score
LoHi
HiHi
time(ms)
K)
L)
HiLo z-score
LoLo z-score
HiLo
LoLo
M)
Opto Firing x Rebound Firing
Dependent
Rebound Firing
Lo Rebound
Hi Rebound
Lo Opto
Hi Opto
Opto Firing

Figure 31: Pvalb-Ai32 Pyr cell rebound effects measured with a factorial design.

(A,C,E,G) SDFs from a single neuron in response to LoHi (A), HiHi (C), HiLo (E), LoLo stimulus conditions (G). For each condition, 100% contrast stimuli were coupled with (blue SDFs) or without Pvalb+ photostimulation (black SDFs). The blue and grey bars above each SDF indicates photostimulation and visual stimulus timing, respectively. (B,D,F,H) Z-score functions (green lines) for all 4 stimulus conditions for the same cell. The red horizontal lines below and above the zero-line indicate a Z-score of ±2. (I-L) Population average Z-score functions for each stimulus condition. Blue shading surrounding black trace indicates SEM. (M) Estimated marginal means for rebound size when post-photostimulation afferent drive was Hi (yellow) or Lo (blue).

2.3.3.2 Pvalb+ Rebound Effects

From our observations in Experiment 1 that neg-rebound size for *ChR2*-expressing Pvalb+ interneurons is also affected by afferent drive (Figure 24,25), we predicted that for conditions in Experiment 3 where Pvalb+ photostimulation co-occurred with high afferent drive (Figure 30c-d; HiHi and HiLo) should generally produce larger neg-rebounds than conditions where Pvalb+ photostimulation co-occurred with low afferent drive (Figure 30a-b; LoHi and LoLo). However, like with our Pyr data, we were most interested in comparisons between conditions with high vs. low afferent drive during the post-photostimulation epoch because the influence of afferent drive during the neg-rebound was unknown. Figure 32a-h shows data from an example Pvalb+ interneuron with spiking responses shown as control and photostimulated SDFs (left column) and Z-score functions (right column) for all 4 conditions. This Pvalb+ interneuron showed strong activation from photostimulation (blue SDFs), however when cortical illumination was combined with visual stimulation in the HiHi and HiLo conditions, the difference between control (black lines) and photostimulation (blue lines) SDFs (Figure 32c,e) resulted in slightly wanning facilitation in the Z-score functions (Figure 32d,f). In comparison, the SDFs from LoHi and LoLo conditions that combined low afferent drive with photostimulation showed little activity in the control SDF and strong activation in the photostimulation SDF (Figure 32a,g), which produced Z-scores that did not wane (Figure 32b,h). In response to the HiLo condition, which most resembles experiment 1, this Pvalb+ interneuron showed a small and transient decrease in firing when the visual stimulus and photostimulation simultaneously concluded, which was visualized as a Z-score neg-rebound resembling data from experiment 1 (Figure 32e-f). For the HiHi condition, post-photostimulation epoch firing in the photostimulation SDF quickly decreased below the control SDF (Figure 32c), producing negative Z-scores forming a neg-rebound that peaked well before 600ms (Figure 32d). For the LoHi condition, post-photostimulation epoch firing in the photostimulation SDF slowly decreased below the control SDF (Figure 32a), forming a lower amplitude, complex, and prolonged rebound that peaked ~800ms (Figure 32b). Finally, there was little to no post-photostimulation firing in the LoLo condition in either the control or photostimulation SDFs (Figure 32g), which produced no change in the Z-score function after light offset (Figure 32h).

We examined all 4 conditions across our interneuron population with average Z-score functions (Figure 32i-l). As predicted from experiment 1 and the example cell, the population data showed waning facilitation in the photostimulation epoch when cortical illumination coincided with visual stimulation (HiHi and HiLo), compared to when Pvalb+ activation occurred before (LoHi) or after (LoLo) the visual stimulus. The population average for the LoHi condition showed a rebound that was predominantly negative, but also prolonged, low amplitude, and complex (Figure 32i). In comparison, the HiLo and HiHi conditions both showed sharp negative rebounds after light offset (Figure 32j,k), although the HiHi neg-rebound was larger in amplitude. Finally, the LoLo condition produced virtually no rebounds (Figure 32l).

To quantify whether Pvalb+ neg-rebounds were significantly impacted by the level of afferent drive during both epochs we calculated time-averaged Z-scores between 520 and 900 ms of the post-poststimulation epoch. A factorial ANOVA (afferent drive in the photostimulation epoch × afferent drive in the post-photostimulation epoch) showed main effects for both afferent drive during the photostimulation epoch [$F(1, 1) = 8.809$; $p = 0.006$; $N = 34$] and post-photostimulation epoch [$F(1, 1) = 9.875$; $p = 0.003$; $N = 34$], but no evidence of an interaction [$F(1, 1) = 0.254$; $p = 0.617$; $N = 34$; Figure 32m]. This indicated afferent drive in both the photostimulation and post-photostimulation epochs increased the amplitude of neg-rebounds. Estimated marginal means showed large error bars that suggested high variability in neg-rebound size across the population (Figure 32m). Overall, Pvalb+ cell data in experiment 3 corroborated data from experiment 1 by reinforcing the finding that strongly driving V1 during the photostimulation epoch increases neg-rebound amplitude after light offset, but added a new finding that neg-rebound magnitude is further increased when afferent drive in the post-photostimulation epoch is high. Finally, experiment 3 also shows that the co-termination of optogenetic photostimulation and visually driven activity is not required to produce neg-rebounds in Pvalb+ interneurons.

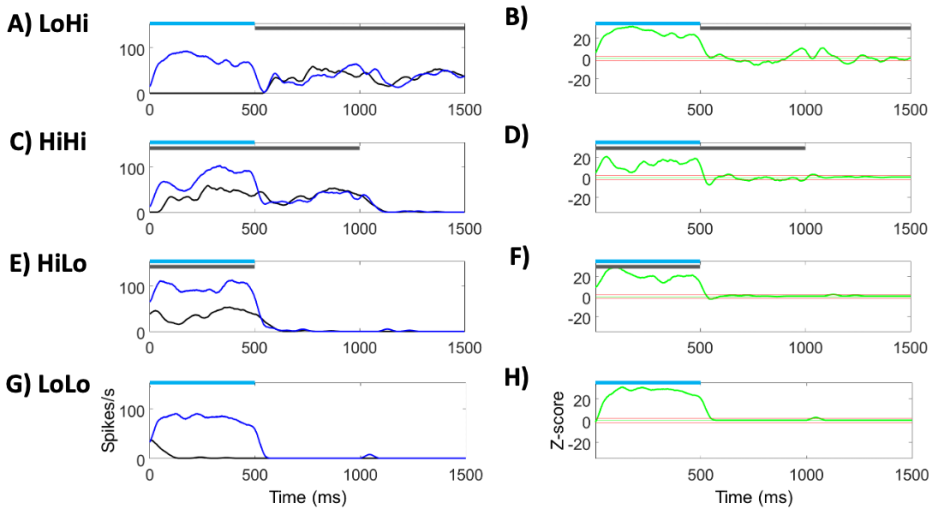
A) LoHi
B)
C) HiHi
D)
E) HiLo
F)
G) LoLo
H)
Spikes/s
Z-score
Time (ms)
Time (ms)

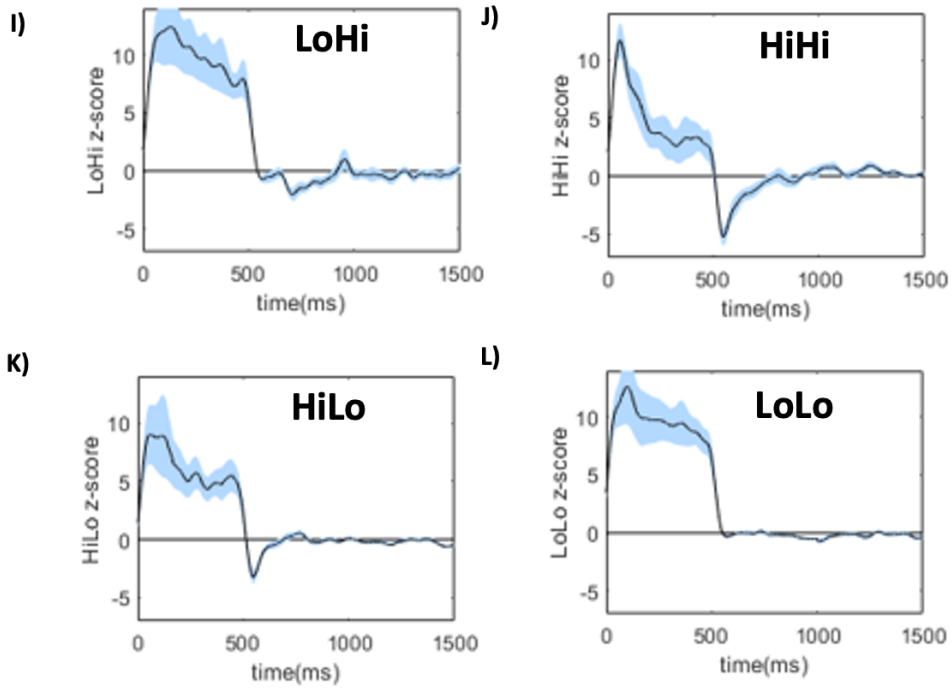
I)
LoHi
LoHi z-score
time(ms)
J)
HiHi
HiHi z-score
time(ms)
K)
HiLo
HiLo z-score
time(ms)
L)
LoLo
LoLo z-score
time(ms)

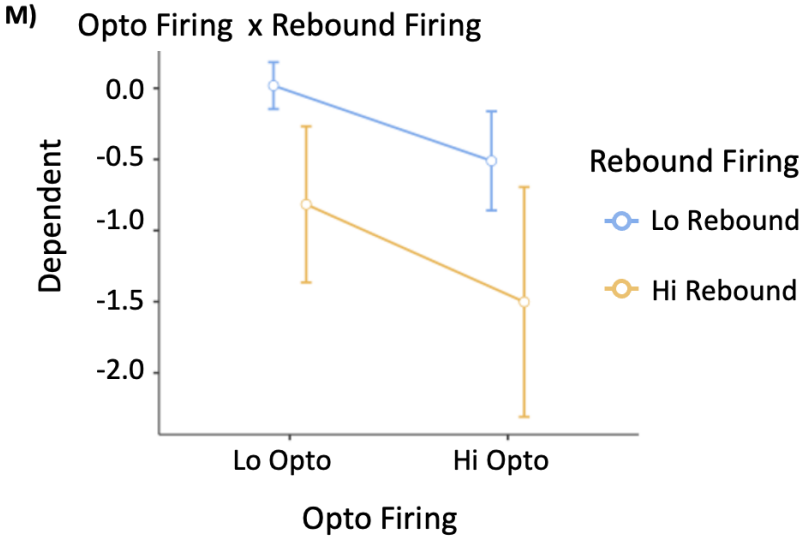
M)
Opto Firing x Rebound Firing
Dependent
Rebound Firing
Lo Rebound
Hi Rebound
Lo Opto
Hi Opto
Opto Firing

Figure 32: Optogenetic activated Pvalb+ cell neg-rebound effects measured with a factorial design.

(A,C,E,G) SDFs from a single Pvalb+ interneurons for LoHi (A), HiHi (C), HiLo (E), LoLo stimulus conditions (G). For each condition, 100% contrast stimuli were coupled with (blue SDFs) or without Pvalb+ photostimulation (black SDFs). The blue and grey bars above each SDF indicates photostimulation and visual stimulus timing, respectively. (B,D,F,H) Z-score functions (green lines) for all 4 conditions for the same interneuron. The red horizontal lines below and above the zero-line indicate a Z-score of ±2. (I-L) Population average Z-score functions for each condition. Blue shading surrounding black trace indicates SEM. (M) Estimated marginal means for neg-rebound size when post-photostimulation afferent drive was Hi (yellow) or Lo (blue).

2.4 Discussion

In this study we investigated whether the circuit features network activity and connectivity affect optogenetic-mediated rebounds in mouse V1. Our results indicate coupling interneuron photostimulation with high visual drive in V1 was most conducive for producing rebound effects in both Pyr cells and *ChR2*-expressing interneurons. However, rebound effects were quite variable across all datasets, being produced in positive and negative directions or not at all. Comparisons across cell-type datasets suggest Pvalb+ photostimulation produced rebound effects more frequently than SOM+ or VIP+ photostimulation. Here, we aim to align these results with past rebound literature and discuss cellular and network mechanisms that may underly rebound effects in mouse V1.

2.4.1 Prevalence of Rebounds

Many optogenetic studies reporting rebounds merely described its presence [143,146,148,152,154,157,158] and methods for limiting them [144,150]. However, optogenetic studies more rigorously examining rebound effects are scarcer [147,151,161]. Here, we base our estimates of rebound prevalence on the stimulus conditions we found were most conducive for producing rebound effects. When we stimulated mouse V1 with 100% contrast stimuli in experiment 1, ≥50% of all Pyr cells from Pvalb-Ai32, Som-Ai32, or Vip-Ai32 mice produced rebounds of varying size and directionality (Figures 17-20) and ~75% *ChR2*-expressing Pvalb+ cells or ~25% of *ChR2*-expressing SOM+ cells produced neg-rebounds (Figure 25-26). This finding was substantiated by experiment 2 population data, showing the majority of Pyr cells produced rebound effects that increased in size from coupling Pvalb+ photostimulation with bars flashed inside opposed to outside RFs (Figure 29e-g). Although it was previously known photostimulating *ChR2*-expressing interneurons can produce strong average rebound effects across many Pyr cells[147], others have not rigorously outlined optogenetic-mediated rebounds across neurons to identify variability in this effect. Future optogenetic studies investigating rebounds should continue to look at prevalence across neurons to better identify the experimental paradigms that produce rebounds more frequently or impact its strength.

2.4.2 Optogenetic Illumination Parameters

By combining visual stimulation and optogenetic photostimulation, we produced rebound effects using light power (light in mW striking cortical surface), irradiance (light in mW striking cortical surface per mm^2), and durations (500-1000ms) that were comparatively weaker and shorter than what has been used in some past optogenetic studies. Past light irradiance used in mouse V1 to produce rebound effects via inhibitory optogenetic proteins (e.g., *Arch,* or red-shifted *NpHR*) vastly exceeded ours (power = 5-35mW/mm^2)[144,157], whereas in higher visual cortices greater light powers and durations were also used to produce rebounds via photostimulating *ChR2*-expressing Pvalb+ cells (power = 0.4-0.5mW; duration = 3500-3800ms)[146]. Additional optogenetic work in non-visual cortices (motor, somatosensory, and hippocampal) that photostimulated *ChR2*-expressing interneurons to produce post-synaptic rebound effects also showed a wide range of light powers, irradiances, and durations can be used to produce rebounds [143,147,151,158]. Several studies used light durations shorter than ours (duration = 30-300ms), however their light power (power = 0.035-3mW) and irradiance (irradiance = 9mW/mm^2) used mostly exceeded ours [143,151,158]. Collectively, it seems rebound effects in mouse cortex do not require the use of excessively strong or long photostimulation powers and durations, respectively, and can still be produced using modest light parameters that do not completely silence neurons [106]. Importantly, Li et al (2019) used many light powers and durations (power = 1.5-7mW; duration = 500-4000ms) to systematically investigate the effect that altering light power and duration can have on rebound effect magnitude. In this study, the lowest light powers and durations used to photostimulate *ChR2*-expressing interneurons during rebound experiments still produced rebounds in post-synaptic neurons, but rebounds were strengthened by increasing both parameters and were strongest by coupling max laser power and duration [147]. This finding aligns with past non-optogenetic work reporting increasing hyperpolarizing pulse amplitude or duration can increase rebound strength [124,170]. One important consideration is that many past optogenetic studies reporting rebound effects were produced *in vitro* [143,148,150,154,158,161] or *in vivo* but did not afferently drive the cortex with any stimulus [147], so greater light powers or irradiances may have been needed to produce strong rebounds. However, because our experimental paradigm included controlling afferent drive in V1 with visual

stimuli, it is conceivable using stronger light power at our set duration could generally increase Pyr cell rebound size regardless of visual stimuli used [147] . Therefore, if we used light power like Li et al's (2019) strongest values (7mW) we may have observed strong Pyr cell rebounds even while using visual stimuli producing no or weak afferent drive in V1 or reduced across-neuron variability of rebound effects while strongly driving V1 neurons with visual stimuli (e.g., 100% contrast, bars flashed inside RF).

2.4.3 Cellular Rebound Mechanisms

In non-optogenetic rebound studies, hyperpolarizing a neuron below -65mV can activate I_h currents, which subsequently activates low-threshold Ca^{2+} currents and drives rebound spiking [118,133,134]. This occurrence of I_h and low-threshold Ca^{2+} currents producing rebound effects has been observed in various neural circuits [122,124–132]. Optogenetic work has also shown a dependence of I_h currents for generating rebound effects *in vivo* by using hyperpolarization-activated cyclic nucleotide-gated (HCN1) channel blockers during photostimulation, which effectively block the generation of I_h currents and rebound spiking [151]. However, our results do not appear consistent with this I_h current pathway driving rebound effects in our experimental paradigm for several reasons. First, in our Pyr cell populations we aimed for mild optogenetic suppression that reduced neuron firing rate by ~30-50% [103,106], so our populations were still adequately depolarized to fire spikes during the photostimulation epoch. Therefore, because these Pyr cells exhibited a membrane potential that was above the spike threshold this should lead to de-activation and inactivation of I_h and low-threshold Ca^{2+} currents, respectively and reduce rebound spiking [118]. One explanation for why membrane hyperpolarization may allow neurons to fire spikes is that voltage-gated Na^+ channels can open at hyperpolarization below resting potential though exhibiting lower opening probabilities [171]. For example, at a membrane potential of -90mv voltage-gated Na^+ channels exhibit ~50% opening probability[171], therefore spikes can still be generated at below resting potential if enough voltage-gated Na^+ channels open, but this should still produce much less spikes.

Second, we show for the first time *ChR2*-expressing interneurons also produce rebound effects after light offset but in the negative direction (neg-rebounds). These neg-rebounds

were generated after *ChR2*-expressing interneurons were optogenetically activated to increase their firing, so photostimulation did not produce the hyperpolarization needed to activate I_h and low-threshold Ca^{2+} currents [118]. Furthermore, neg-rebounds themselves were produced in interneuron Z-score functions due to firing at light offset being more suppressed in experimental than control trials (Figures 21-23), so no rebound spikes were produced in the post-photostimulation epoch presumably because I_h and low-threshold Ca^{2+} currents were not activated in these interneurons [118]. Although *ChR2*-expressing interneuron neg-rebounds were most prevalent following paradoxical suppression, these cells still produced robust optogenetic-driven firing but waned over time and occasionally reached negative Z-score values (Figures 21-27). Therefore, paradoxically suppressed interneuron neg-rebounds were likely not generated via I_h and low-threshold Ca^{2+} currents because these cells still produced strong visual responses during photostimulation that require membrane depolarization. Even if optogenetic activation of *ChR2*-expressing interneurons produced paradoxical suppression that sufficiently hyperpolarized these cells to activate I_h or low-threshold Ca^{2+} currents, this should have led to rebound spikes [118], but rather produced a completely opposite rebound effect in the negative direction. Collectively, these insights suggest a cellular mechanism other than this I_h -mediated pathway driving rebounds should be considered.

In our experiments, optogenetically activating *ChR2*-expressing interneurons to increase GABA neurotransmission could activate post-synaptic metabotropic $GABA_B$ receptors to drive Pyr cell rebound effects. In this scenario, $GABA_B$ mediated suppression would develop slowly due to GABA binding to metabotropic receptors that through a cascade of steps produce membrane hyperpolarization [134,172]. $GABA_B$ activation can deinactivate low-threshold Ca^{2+} channels [134,172], which as previously stated is known to drive rebound depolarization[118,134]. The sequence of neuron hyperpolarization then depolarizing the cell from low-threshold Ca^{2+} currents can occur very fast (<200ms) [123], so the slower timeframe of $GABA_B$ activation driving low-threshold Ca^{2+} spikes may be possible with our photostimulation times (500-1000ms). Past non-optogenetic work in thalamic and subthalamic regions suggest $GABA_B$ receptors can indeed drive rebound spiking [119,173], although these rebounds may be greatest with synergistic activation of $GABA_B$ and ionotropic $GABA_A$ receptors [173]. Considering both $GABA_A$ and $GABA_B$

receptors are expressed in the cortex [174], it is entirely possible V1 Pyr cells may co-express these two receptor types and become co-activated when *ChR2*-expressing GABAergic cells are photostimulated. However, other accounts suggest $GABA_B$ receptors suppress rebound effects that are driven by activation of $GABA_A$ receptors [175]. More importantly, low-threshold Ca^{2+} currents require strong hyperpolarization to deinactivate [134,172], therefore the $GABA_B$ -mediated pathway driving rebound spikes in our data suffers from the same logical issues as the I_h -mediated pathway. Despite optogenetic activation of *ChR2*-expressing interneurons results in GABA neurotransmission and likely $GABA_B$ activation, our neurons were still sufficiently depolarized to fire spikes, so they could not be strongly hyperpolarized to deinactivate low-threshold Ca^{2+} currents [118,134,172].

For photostimulated interneurons themselves, some "fatigue-like" processes [176] that cause the neuron to adapt might contribute to neg-rebound effects in mouse V1. Strong optogenetic activation of *ChR2*-expressing interneurons may "fatigue" these cells, resulting in hyperpolarization of the membrane potential that consequently depresses firing [177,178]. The cellular mechanism underlying this spike frequency adaptation is increased intracellular Na^+ and Ca^{2+} from spiking being used to activate outward K^+ currents that hyperpolarize the cell [177]. Therefore, once optogenetic activation of *ChR2*-expressing interneurons produce strong spiking (Figure 21-27) the increase in intracellular Na^+ and Ca^{2+} activation of outward K^+ currents would hyperpolarize the cell, reducing spiking that continued past light offset would be visible as a neg-rebound (Figure 21-24). Continual optogenetic activation of *ChR2*-expressing interneurons may also "fatigue" these cells to affect GABA neurotransmission due to depletion of the readily releasable pool of synaptic vesicles [179]. At light onset *ChR2*-expressing interneurons fire strongly (Figure 21-27), potentially using up the readily releasable pool that may take some time to fully replenish [179]. This depletion of the readily releasable pool would not affect the spike rate of *ChR2*-expressing interneurons though, but rather reduce neurotransmission at GABAergic synapses. If synaptic vesicles become depleted at the presynaptic active zone near light offset and result in reduced GABA neurotransmission, then after light offset this could promote Pyr cell rebound depolarization by less residual GABA within the synaptic cleft activating fast-acting,

post-synaptic $GABA_A$ receptors.

2.4.4 Network Rebound Mechanisms

Cell-to-cell connections are likely important for producing optogenetic-mediated rebound effects *in vivo*. First, *ChR2*-expressing interneurons themselves might produce neg-rebounds if mouse V1 functions as an inhibition stabilized network (ISN) [63,68]. In ISN models of cortical circuits, local excitation is unstable due to fluctuating afferent input from TC cells and is stabilized within the cortex via feedback inhibition [63]. Therefore, when circuits are strongly activated and generate strong feedback inhibition to reduce local excitation, inhibition must then be regulated too so GABAergic firing paradoxically suppresses from this activation [63,68,70]. It is hypothesized for ISN paradoxical suppression to occur *in vivo* widespread activation of many interneurons is likely needed [69]. In optogenetic studies, photostimulating *ChR2*-expressing GABAergic cells within a local circuit strongly activates them and can produce paradoxical suppression in these same interneurons [106,147]. Therefore, during the end of the photostimulation epoch the only factor maintaining firing in paradoxically suppressed *ChR2*-expressing interneurons may be photostimulation itself. In this case, light offset would drive further decreased firing in paradoxically suppressed *ChR2*-expressing interneurons that would be visible as a neg-rebound effect (Figure 21-24). Second, in our study *ChR2*-expressing Pvalb+ or SOM+ interneurons produced their peak neg-rebounds significantly earlier than the peak positive rebounds observed in corresponding Pyr cells collected from Pvalb-Ai32 or Som-Ai32 mice, respectively. This difference in directionally and latency of rebound effects between *ChR2*-expressing interneurons and post-synaptic Pyr cells may indicate a potential sequence of synaptic events occurring between these neurons after light offset. Once the LED light is turned off and Pvalb+ or SOM+ interneurons generate neg-rebound effects, this may temporarily decrease inhibitory post-synaptic potentials (IPSP) in Pyr cells, driving rebound depolarization and spikes. Interestingly, optogenetic work and accompanying simulations in mouse hippocampus and cortex has shown when interneurons and Pyr cells are reciprocally connected Pyr cells produce rebound spikes when oscillating interneuron activity is at a trough [151]. If *ChR2*-expressing interneuron neg-rebounds in-part drive Pyr cell rebound spiking, then the strength and abundance of rebound spiking across neurons within a local circuit may be determined by the

connection strength between photostimulated interneurons and post-synaptic Pyr cells. Interneurons of the same subtype are electrically connected via gap-junctions (Figure 11a) to synchronize activation of like interneurons and pool inhibitory drive [58–60], so when *ChR2*-expressing interneurons generate neg-rebounds this after-effect is likely transmitted to other like interneurons that are electrically adjoined. Pyr cells receiving strong connections from GABAergic microcircuits generating neg-rebounds may then produce rebound spikes themselves, however other neurons may be weakly connected to these same GABAergic microcircuits and therefore be less affected by neg-rebounds. In our data, across-neuron variability in Pyr cell rebound effect size could in-part be attributed to how strongly connected these Pyr cells were to GABAergic microcircuits generating neg-rebounds.

Network connectivity may also be a primary contributor for driving Pyr cell rebound effects *in vivo* because inputs from various pre-synaptic cell-types, including Pvalb+, SOM+, or VIP+ cells (Figure 11a) could promote or impede post-synaptic rebound effects. Past optogenetic work that photostimulated *ChR2*-expressing interneurons to show the occurrence of rebounds in post-synaptic cells was done in VGAT-*ChR2* mice [143,146,147], which express optogenetic proteins in all GABAergic interneuron cell-types [180], but some also reported post-synaptic rebounds from exclusively photostimulating Pvalb+ or SOM+ cells [147,151,158]. Conversely, photoinhibition of *Arch*-expressing VIP+ cells can also produce rebound effects in polysynaptic Pyr cells and in the *Arch*-expressing VIP+ interneurons themselves [157], and a more recent study that photoinhibited *Arch*-expressing Pvalb+, SOM+, or VIP+ interneurons separately reported differences in rebound effect size and duration across these 3 interneuron groups [161]. However, no study has rigorously compared Pyr cell rebound effects from photostimulating *ChR2*-expressing Pvalb+, SOM+, or VIP+ cells separately or identified if optogenetic activation of *ChR2*-expressing interneurons produce rebound effects in these interneurons themselves. We report photostimulating Pvalb+, SOM+, or VIP+ cells separately can all produce rebound effects in both *ChR2*-expressing interneurons and post-synaptic Pyr cells, though the cell-type being photostimulated can impact its prevalence across neurons. Rebound effects produced by *ChR2*-expressing interneurons or post-synaptic Pyr cells were most abundant in Pvalb-

Ai32 mice despite Pvalb+ and SOM+ interneurons both sending direct inhibitory projections to Pyr cells in mouse V1 [106]. In this circuit, Pvalb+ cells potentially may drive stronger rebound effects than SOM+ cells because of several subtle differences between these interneuron subtypes. It is known Pvalb+ and SOM+ cells differ in their distribution and input across cortical lamina [91,97], their local network connectivity (Figure 11a) [89,90], what regions of Pyr cells their synapses make contact with (Figure 11a)[56,90], the amount of afferent input they receive from thalamocortical (TC) cells [86], and how they summate excitatory inputs [56,94–96]. Together, these differences in mouse V1 connectivity may drive Pvalb+ inhibition to produce a greater unitary inhibitory hit onto Pyr cells than SOM+ inhibition [90,181], which subsequently may produce stronger or more frequent rebound effects to balance priorly strong inhibition (Figure 24a-d). Whereas Pvalb+ and SOM+ interneurons directly inhibit Pyr cells, VIP+ interneurons disinhibit them [106] by directly inhibiting SOM+ cells (Figure 11a)[90,98]. Therefore, it is conceivable why photoinhibiting *Arch*-expressing VIP+ cells can produce rebound effects in polysynaptic Pyr cells [157]; *Arch*-mediated VIP+ suppression should lead to increased SOM+ activity and subsequently suppress Pyr cells [56,89,90], which after light offset may drive Pyr cell rebound spikes. However, we show for the first time photostimulating *ChR2*-expressing VIP+ interneurons can produce rebound spiking in mouse V1 Pyr cells (inverted rebounds). Finding rebound spiking in our Pyr_{vip}^{facil} cells was surprising because typically inhibitory optogenetic photomodulations drives rebound spiking [143,144,146–148,150–152,154,157,158,161], but we observed excitatory optogenetic photomodulations followed by more spiking (Figure 16,20). Additionally, while *ChR2*-expressing Pvalb+ and SOM+ cells generated neg-rebounds that could be quite strong, little to no neg-rebounds were observed in *ChR2*-expressing VIP+ cells. This finding aligns with recent optogenetic work showing photoinhibition of *Arch*-expressing Pvalb+ and SOM+ cells can produce positive rebound effects that are significantly larger in amplitude than what was seen in *Arch*-expressing VIP+ cells [161]. Although photoinhibition of *Arch*-expressing VIP+ cells can indeed produce rebound effects [157], Pvalb+ and SOM+ interneurons may simply produce comparably stronger rebound effects from optogenetics (Figures 21-27) [161].

2.4.5 Visual Stimuli that Drive Rebound Effects

The visual stimulus and optogenetic protocols used in our study were designed to couple interneuron photostimulation with varying levels of afferent input to mouse V1 via visual stimuli (e.g., varying stimulus contrast level or flashing bars within or outside RF). This experimental paradigm was effective at determining afferent drive during photostimulation can affect rebound size and prevalence across neurons after light offset (as seen in experiments 1 and 2) due to how both stimuli activate the local network. For retinotopic stimuli, all recorded neurons roughly share the same RF because all neurons near an electrode recording site are neighboring neurons within retinotopic maps of mouse V1 [77]. Therefore, stimuli presented within or outside a neurons RF, including bars or gratings can produce a predictable response across recorded V1 neurons. One caveat against a more complex retinotopic stimulus like gratings driving similar activity across neurons when presented within the RF is that features of the visual stimulus (e.g., contrast, orientation) affect neuronal firing as well. For contrast stimuli, all cells in the local network are still activated by a similar amount across contrast levels because V1 neurons generally increase their response to higher levels of visual contrast that produces a stereotypical sigmoidal contrast response function (CRF) [43–48]. However, varying grating orientation can produce vastly different responses across mouse V1 neurons due to the "salt-and-pepper" organization of orientation preferences across local neurons that produce no clear pattern in this cortical region [77]. Consequently, mouse V1 is comprised of many poorly orientation-tuned Pyr cells and interneurons due to their nonspecific pooling of local inputs with varying orientation preferences [182–186]. Therefore, when gratings of varying orientation are presented within V1 neuron RFs, sharply tuned neurons differentially respond to various stimulus orientations, while poorly tuned neurons will respond similarly for all stimulus orientations. Unfortunately, poorly tuned Pyr cells may not exhibit sufficiently different firing rates at preferred vs orthogonal orientations to perform the rebound analyses we conducted in experiments 1 and 2, so only well-tuned Pyr cells with strong orientation preferences would be useful within our experimental paradigm. Therefore, despite orientation protocols being heavily used to study photomodulations during the photostimulation epoch [85], we elected to not use this protocol because this stimulus feature heterogeneously activates this network.

Collectively, these insights suggest simple stimuli flashed within the classical RF (e.g., flashed bars) or more complex retinotopic stimuli that can produce predictable responses across a stimulus preference (e.g., contrast) are best for studying how afferent input to mouse V1 affects optogenetic-mediated rebound effects. Furthermore, stimuli that can generate widespread local network activity (e.g., high contrast stimuli, or bars flashed within the RF) are most conducive for producing strong optogenetic-mediated rebound effects across many V1 neurons.

2.4.6 Future Directions

The present study raises a few unanswered questions. First, non-optogenetic research investigating rebounds strongly indicates rebound spikes are driven by I_h and low-threshold Ca^{2+} currents [118,133,134], but this may be because a lot of this data was acquired from *in vitro* preparations. Despite our data not aligning with I_h and low-threshold Ca^{2+} currents driving rebound effects in mouse V1, past *in vivo* optogenetic research has shown a dependence of I_h currents for generating rebound spiking [151]. Future optogenetic research investigating rebounds should more clearly identify the ionic currents neurons use to produce rebound spiking *in vivo* by using intracellular V1 recordings. Second, all our Pyr cell and interneuron datasets exhibited across-neuron variability, even when we coupled photostimulation with visual stimuli producing the most afferent drive to V1 (see quartile data, Figures 17-20, 25-27). A few explanations may in part further explain why rebound effects are not seen across all neurons. As previously mentioned, the connection strength of GABAergic synapses producing neg-rebounds could affect post-synaptic Pyr cell rebound spiking (section 2.4.4, network rebound mechanisms). Stark et al (2013) also showed in their simulation that synaptic depression of interneuron inputs onto Pyr cells can abolish rebound spiking in theta frequencies (3-8 hertz). Furthermore, the relationship between the magnitude of light power or duration with rebound effect size [147] may suggest photostimulating *ChR2*-expressing interneurons with very dim and short-lasting light may not produce strong rebound effects across many post-synaptic neurons. Future optogenetic research could measure how the prevalence of rebound effects across neurons is affected by GABAergic synaptic strength, plasticity, or by optogenetic light parameters. Third, rebound effects in mouse V1 may not be contained here but rather

echoed to upstream or downstream circuits due to V1's feedforward projections within the cortex [42] and feedback connections to the thalamus [29–31]. Interarea rebound effects have been observed in non-optogenetic studies with TC cell rebound spikes being transmitted and driving later cortical rebound effects [138]. Future optogenetic research investigating rebound effects may investigate this interarea network effect whereby rebound spikes generated within a local circuit drive rebound effects in other cortical and subcortical regions. Finally, if feedforward connections from V1 volley rebound spikes to higher order visual cortices, then this may affect mouse visual behavior by altering activity in these cortical regions. Optogenetic-mediated rebound spiking can affect specific motor behaviors in mice [156] and fish [155]. A more recent study showed optogenetic activation of inhibitory inputs from the substania nigra to the superior colliculus produce contralateral orienting movements in mice that can be explained and align well with non-optogenetic rebounds that were measured from brain slices *ex vivo* [159]. Still, the impact optogenetic-mediated rebound effects have on mouse behavior is scant. Future investigations into mouse behavior during visual tasks could explore how rebound effects impact mouse performance by measuring responses during both photostimulation and post-photostimulation epochs. Furthermore, because visual stimulation and optogenetics have precise temporal control, coupling visual tasks with photostimulation or photoinhibition via excitatory or inhibitory optogenetic proteins, respectively may be a good way to look at the timing of behaviors relative to potential rebound effects after light offset.

3. CHAPTER 3: CONCLUSION

When a neuron is strongly hyperpolarized by an inhibitory stimulus later termination of this stimulus can drive subsequent rebound depolarization that generates spikes, a phenomenon known as a post-inhibitory rebound (PIR) effect. Originally, PIRs were mainly studied *in vitro* via inhibitory current injections [118,119,122,124–132]. However, optogenetic work has now reported rebound effects can be produced after light offset *in vitro* and *in vivo* preparations, including in the mouse V1 [143,144,146–148,150–155,157,161]. Most optogenetic work investigating rebound effects merely reported the presence of them, but it is now known manipulating factors external to the photostimulated circuit can alter rebound effects; ramp-like termination of the optogenetic light source can diminish rebounds [144,150] and increasing light power or duration can increase rebound size [147]. However, little is known regarding what intrinsic features of the photostimulated circuits can drive rebound effects in optogenetic experiments. Therefore, we sought to explore whether V1 circuits impact rebound effects by either (i) manipulating network activity during interneuron photostimulation via visual stimuli, or (ii) photostimulating *ChR2*-expressing Pvalb+, SOM+, or VIP+ interneurons separately during visual stimulation of mouse V1. (i) We provide evidence from experiments 1 (varying stimulus contrast) and 2 (flashing bars inside verse outside the classical RF) that coupling interneuron photostimulation with high opposed to low afferent drive increases Pyr cell and *ChR2*-expressing interneuron rebound effect size and frequency in mouse V1. However, rebound effects seen across Pyr cell and interneuron populations showed strong within- and across-neuron variability. Additionally, both Pyr cell and *ChR2*-expressing Pvalb+ rebound effects did not require the co-occurrence of light and visual stimulus offset. (ii) Both Pyr cell and *ChR2*-expressing interneuron rebound effects were larger and more prevalent in Pvalb-Ai32 than Som-Ai32 or Vip-Ai32 mice. Additionally, we show for the first time *ChR2*-expressing interneurons can produce neg-rebound effects and provide evidence they occur in time before Pyr cell rebounds.

Our data provides insight for future optogenetic studies in mouse V1, other mouse cortical circuits, and general understanding of cortical functioning. If rebound effects are not the focus of optogenetic experiments, identifying the scenarios optogenetics might

produce rebound effects *in vivo* may advise researchers how long to wait after light offset for data acquisition or when to use a method such as ramp-like light termination to avoid rebound spiking [144,150]. In mouse V1, knowing these scenarios optogenetics can produce rebound effects may be critical for future studies investigating adaptation with optogenetics that take experimental measurements after light off-set [167]. However, rebound spiking is a critical feature for basic central nervous system functions such as generating oscillatory activity [114–120] . Thalamic circuits that incorporate reciprocally connected excitatory TC cells and GABAergic interneurons produce oscillations via TC rebound spikes recurrently activating the local circuit after bouts of strong GABAergic inhibition [120]. Some evidence suggests these thalamic rebound effects may impact sensory processing [187] and is hypothesized to contribute to neurological disorders such as epilepsy by trigger some forms of epileptic seizures [188]. Seizures are strongly driven by an imbalance between cortical excitation and inhibition [188], therefore a growing body of research has leveraged optogenetics for manipulating GABAergic transmission via photostimualting or photoinhibiting *ChR2*- or *Arch*-expressing interneurons, respectively to show a role for rebound spikes triggering seizures in epileptic mouse models [143,158,160,161]. In non-epileptic cortex, optogenetic-mediated rebound effects may be used within photostimulated circuits to maintain excitatory-inhibitory (E-I) balance [42]. It is known when E-I balance is continually perturbed that compensatory mechanisms within neuronal networks are used to restabilize it, such as plastic modifications of synapses or trafficking ion channels to regulate circuit or neuronal excitability, respectively [189]. However, after strong inhibition is quickly generated within a local circuit (e.g., photostimulating *ChR2*-expressing interneurons) rebound effects could potentially be used as a faster-acting circuit mechanism to regulate E-I balance.

REFERENCE LIST

1. Prasad, S. & Galetta, S. L. Chapter 1 - Anatomy and physiology of the afferent visual system. *Handb Clin Neurol* 102, 3–19 (2011).

2. Lamb, T. D. Why rods and cones? *Eye* 30, 179–185 (2016).

3. Jacobs, G. H. Color vision variations non-human. *Trends in Neuroscience* 9, 320–323 (1986).

4. Taylor, W. R. & Smith, R. G. Transmission of scotopic signals from the rod to rod-bipolar cell in the mammalian retina. *Vision Res* 44, 3269–3276 (2004).

5. Curcio, C. A. *et al.* Human Photoreceptor Topography. *The Journal of Comparative Neurobiology* 292, 497–523 (1990).

6. Euler, T., Haverkamp, S., Schubert, T. & Baden, T. Retinal bipolar cells: Elementary building blocks of vision. *Nat Rev Neurosci* 15, 507–519 (2014).

7. Stell, W. K., Ishida, A. T. & Lightfoot, D. O. Structural Basis for On-and Off-Center Responses in Retinal Bipolar Cells. *Science (1979)* 198, 1269–1271 (1977).

8. Cook, P. B. & McReynolds, J. S. Lateral inhibition in the inner retina is important for spatial tuning of ganglion cells. *Nat Neurosci* 1, 714–719 (1998).

9. Naka, K.-I. & Witkovsky, P. Dogfish ganglion cell discharge resulting from extrinsic polarization of the horizontal cells. *J Physiol* 223, 449–460 (1972).

10. Werblin, F. S. & Dowling, J. E. Organization of the retina of the mudpuppy, Necturus maculosus. II. Intracellular recording. *J Neurophysiol* 32, 339–355 (1969).

11. Kolb, H. & Famiglietti, E. V. Rod and Cone Pathways in the Inner Plexiform Layer of Cat Retina. *Science (1979)* 186, 47–49 (1974).

12. Strettoi, E., Raviola, E. & Dacheux, R. F. Synaptic connections of the narrow-field, bistratified rod amacrine cell (AII) in the rabbit retina. *J Comp Neurol* 325, 152–168 (1992).

13. Kuffler, S. W. Discharge patterns and functional organization of mammalian retina. *J Neurophysiol* 16, 37–68 (1953).

14. Enroth-Cugell, C. & Robson, J. G. The contrast sensitivity of retinal ganglion cells of the cat. *J Physiol* 187, 517–552 (1966).

15. Field, G. D. & Chichilnisky, E. J. Information processing in the primate retina: Circuitry and coding. *Annu Rev Neurosci* 30, 1–30 (2007).

16. Dacey, D. M., Peterson, B. B., Robinson, F. R. & Gamlin, P. D. Fireworks in the primate retina: in vitro photodynamics reveals diverse LGN-projecting ganglion cell types. *Neuron* 37, 15–27 (2003).

17. Callaway, E. M. Structure and function of parallel pathways in the primate early visual system. *Journal of Physiology* vol. 566 13–19 Preprint at https://doi.org/10.1113/jphysiol.2005.088047 (2005).

18. Kaplan, E. & Shapley, R. M. The primate retina contains two types of ganglion cells, with high and low contrast sensitivity. *Proceedings of the National Academy of Sciences* 83, 2755–2757 (1986).

19. Michael, C. R. Retinal afferent arborization patterns, dendritic field orientations, and the segregation of function in the lateral geniculate nucleus of the monkey. *Proceedings of the National Academy of Sciences* 85, 4914–4918 (1988).

20. Wiesel, T. N. & Hubel, D. H. Spatial and chromatic interactions in the lateral geniculate body of the rhesus monkey. *J Neurophysiol* 29, 1115–1156 (1966).

21. Nassi, J. J. & Callaway, E. M. Parallel processing strategies of the primate visual system. *Nat Rev Neurosci* 10, 360–372 (2009).

22. De Moraes, C. G. Anatomy of the visual pathways. in *Journal of Glaucoma* vol. 22 S2–S7 (Wolters Kluwer, 2013).

23. Shapley, R., Kaplan, E. & Soodak, R. Spatial summation and contrast sensitivity of X and Y cells in the lateral geniculate nucleus of the macaque. *Nature* 292, 543–545 (1981).

24. Perry, V. H., Oehler, R. & Cowey, A. Retinal ganglion cells that project to the dorsal lateral geniculate nucleus in the macaque monkey. *Neuroscience* 12, 1101–1123 (1984).

25. Shapley, R. & Hugh Perry, V. Cat and monkey retinal ganglion cells and their visual functional roles. *Trends Neurosci* 9, 229–235 (1986).

26. Connolly, M. & Van Essen, D. The representation of the visual field in parvicellular and magnocellular layers of the lateral geniculate nucleus in the macaque monkey. *J Comp Neurol* 226, 544–564 (1984).

27. Kupfer, C. The Projection of the Macula in the Lateral Geniculate Nucleus of Man* *From the Howe Laboratory of Ophthalmology, Harvard University Medical School, and the Massachusetts Eye and Ear Infirmary. *Am J Ophthalmol* 54, 597–609 (1962).

28. Tootell, R., Switkes, E., Silverman, M. & Hamilton, S. Functional anatomy of macaque striate cortex. II. Retinotopic organization. *The Journal of Neuroscience* 8, 1531–1568 (1988).

29. Gilbert, C. D. Microcircuitry of the visual cortex. *Annu Rev Neurosci* 6, 217–264 (1983).

30. Gilbert, C. D. & Wiesel, T. N. Functional Organization of the Visual Cortex. *Prog Brain Res* 58, 209–218 (1983).

31. Sincich, L. C. & Horton, J. C. The circuitry of V1 and V2: Integration of color, form, and motion. *Annu Rev Neurosci* 28, 303–326 (2005).

32. Hubel, D. H. & Wiesel, T. N. Receptive fields of single neurones in the cat's striate cortex. *Journal of Physiology* 148, 574–591 (1959).

33. Hubel, D. H. & Wiesel, T. N. Receptive fields and functional architecture of monkey striate cortex. *Journal of Physiology* 195, 215–243 (1968).

34. Hubel, D. H. & Wiesel, A. T. N. Receptive fields, binocular interaction and functional architecture in the cat's visual cortex. *Journal of Physiology* 160, 106–154 (1962).

35. Movshon, J. A., Thompson, I. D. & Tolhurst, D. J. Spatial summation in the receptive fields of simple cells in the cat's striate cortex. *Journal of Physiology* 283, 53–77 (1978).

36. Movshon, J. A., Thompson, I. D. & Tolhurst, D. J. Receptive field organization of complex cells in the cat's striate cortex. *Journal of Physiology* 283, 79–99 (1978).

37. Bartfeld, E. & Grinvald, A. Relationships between orientation-preference pinwheels, cytochrome oxidase blobs, and ocular-dominance columns in primate striate cortex. *Proceedings of the National Academy of Sciences* 89, 11905–11909 (1992).

38. Nauhaus, I., Benucci, A., Carandini, M. & Ringach, D. L. Neuronal Selectivity and Local Map Structure in Visual Cortex. *Neuron* 57, 673–679 (2008).

39. Xu, X., Ichida, J., Shostak, Y., Bonds, A. B. & Casagrande, V. A. Are primate lateral geniculate nucleus (LGN) cells really sensitive to orientation or direction? *Vis Neurosci* 19, 97–108 (2002).

40. Priebe, N. J. & Ferster, D. Inhibition, Spike Threshold, and Stimulus Selectivity in Primary Visual Cortex. *Neuron* 57, 482–497 (2008).

41. Kerlin, A. M., Andermann, M. L., Berezovskii, V. K. & Reid, R. C. Broadly Tuned Response Properties of Diverse Inhibitory Neuron Subtypes in Mouse Visual Cortex. *Neuron* 67, 858–871 (2010).

42. Isaacson, J. S. & Scanziani, M. How inhibition shapes cortical activity. *Neuron* 72, 231–243 (2011).

43. Albrecht, D. G. & Hamilton, D. B. Striate Cortex of Monkey and Cat: Contrast Response Function. *J Neurophysiol* 48, 217–237 (1982).

44. Movshon, J. A., Thompson, I. D. & Tolhurst, D. J. Spatial and temporal contrast sensitivity of neurones in areas 17 and 18 of the cat's visual cortex. *Journal of Physiology* 283, 101–120 (1978).

45. Ohzawa, I., Sclar, G. & Freeman, R. Contrast gain control in the cat visual cortex. *Nature* 298, 266–268 (1982).

46. Sclar, G., Ohzawa, I. & Freeman, R. D. Contrast gain control in the kitten's visual system. *J Neurophysiol* 54, 668–675 (1985).

47. Sclar, G., Lennie, P. & DePriest, D. D. Contrast adaptation in striate cortex of macaque. *Vision Res* 29, 747–755 (1989).

48. Sclar, G., Maunsell, J. H. R. & Lennie, P. Coding of image contrast in central visual pathways of the macaque monkey. *Vision Res* 30, 1–10 (1990).

49. Allman, J., Miezin, F. & Mcguinness, E. Stimulus Specific Responses from Beyond the Classical Receptive Field: Neurophysiological Mechanisms for Local-Global Comparisons in Visual Neurons. *Annu Rev Neurosci* 8, 407–430 (1985).

50. Walker, G. A., Ohzawa, I. & Freeman, R. D. Asymmetric Suppression Outside the Classical Receptive Field of the Visual Cortex. *Journal of Neuroscience* 19, 10536–10553 (1999).

51. Douglas, R. J. & Martin, K. A. C. Canonical Cortical Circuits. in *Handbook of Brain Microcircuits* (eds. Shepherd, G. & Grillner, S.) vol. 1 15–21 (Oxford University Press, 2010).

52. Douglas, R. J. & Martin, K. A. C. Neuronal circuits of the neocortex. *Annu Rev Neurosci* 27, 419–451 (2004).

53. Douglas, R. J., Martin, K. A. C. & Whitteridge, D. A Canonical Microcircuit for Neocortex. *Neural Comput* 1, 480–488 (1989).

54. Peters, A. & Payne, B. R. Numerical relationships between geniculocortical afferents and pyramidal cell modules in cat primary visual cortex. *Cerebral cortex* 3, 69–78 (1993).

55. Ahmed, B., Anderson, J. C., Douglas, R. J., Martin, K. A. & Nelson, J. C. Polyneuronal innervation of spiny stellate neurons in cat visual cortex. *J Comp Neurol* 341, 39–49 (1994).

56. Tremblay, R., Lee, S. & Rudy, B. GABAergic Interneurons in the Neocortex: From Cellular Properties to Circuits. *Neuron* 91, 260–292 (2016).

57. DeFelipe, J., Alonso-Nanclares, L. & Arellano, J. I. Microstructure of the neocortex: comparative aspects. *J Neurocytol* 31, 299–316 (2002).

58. Beierlein, M., Gibson, J. R. & Connors, B. W. A network of electrically coupled interneurons drives synchronized inhibition in neocortex. *Nature Neuroscience* 3, 904–910 (2000).

59. Galarreta, M. & Hestrin, S. A network of fast-spiking cells in the neocortex connected by electrical synapses. *Nature* 402, 72–75 (1999).

60. Simon, A., Oláh, S., Molnár, G., Szabadics, J. & Tamás, G. Gap-junctional coupling between neurogliaform cells and various interneuron types in the neocortex. *Journal of Neuroscience* 25, 6278–6285 (2005).

61. Meinecke, D. L. & Peters, A. GABA immunoreactive neurons in rat visual cortex. *J Comp Neurol* 261, 388–404 (1987).

62. Kirmse, K. & Zhang, C. Principles of GABAergic signaling in developing cortical network dynamics. *Cell Reports* vol. 38 Preprint at https://doi.org/10.1016/j.celrep.2022.110568 (2022).

63. Tsodyks, M. V, Skaggs, W. E., Sejnowski, T. J. & Mcnaughton, B. L. Paradoxical Effects of External Modulation of Inhibitory Interneurons. *Journal of Neuroscience* 17, 4382–4388 (1997).

64. Ferguson, B. R. & Gao, W. J. Pv interneurons: critical regulators of E/I balance for prefrontal cortex-dependent behavior and psychiatric disorders. *Front Neural Circuits* 12, 2–13 (2018).

65. Lewis, D. A., Curley, A. A., Glausier, J. R. & Volk, D. W. Cortical parvalbumin interneurons and cognitive dysfunction in schizophrenia. *Trends Neurosci* 35, 57–67 (2012).

66. Marín, O. Interneuron dysfunction in psychiatric disorders. *Nat Rev Neurosci* 13, 107–120 (2012).

67. Selten, M., Bokhoven, H. van & Nadif Kasri, N. Inhibitory control of the excitatory/inhibitory balance in psychiatric disorders. *F1000Res* 7, 1–16 (2018).

68. Ozeki, H., Finn, I. M., Schaffer, E. S., Miller, K. D. & Ferster, D. Inhibitory Stabilization of the Cortical Network Underlies Visual Surround Suppression. *Neuron* 62, 578–592 (2009).

69. Sadeh, S., Silver, R. A., Mrsic-Flogel, T. D. & Muir, D. R. Assessing the Role of Inhibition in Stabilizing Neocortical Networks Requires Large-Scale Perturbation of the Inhibitory Population. *The Journal of Neuroscience* 37, 12050–12067 (2017).

70. Miller, K. D. Canonical computations of cerebral cortex. *Curr Opin Neurobiol* 37, 75–84 (2016).

71. Carandini, M. & Ferster, D. Membrane potential and firing rate in cat primary visual cortex. *Journal of Neuroscience* 20, 470–484 (2000).

72. Rose, D. & Blakemore, C. Effects of bicuculline on functions of inhibition in visual cortex. *Nature* 249, 375–377 (1974).

73. Markram, H. *et al.* Interneurons of the neocortical inhibitory system. *Nat Rev Neurosci* 5, 793–807 (2004).

74. Rudy, B., Fishell, G., Lee, S. H. & Hjerling-Leffler, J. Three groups of interneurons account for nearly 100% of neocortical GABAergic neurons. *Dev Neurobiol* 71, 45–61 (2011).

75. Baker, M. Neuroscience: Through the eyes of a mouse. *Nature* 502, 156–158 (2013).

76. Harris, K. D. & Mrsic-Flogel, T. D. Cortical connectivity and sensory coding. *Nature* 503, 51–58 (2013).

77. Seabrook, T. A., Burbridge, T. J., Crair, M. C. & Huberman, A. D. Architecture, Function, and Assembly of the Mouse Visual System. (2017) doi:10.1146/annurev-neuro-071714.

78. Gao, E., DeAngelis, G. C. & Burkhalter, A. Parallel input channels to mouse primary visual cortex. *Journal of Neuroscience* 30, 5912–5926 (2010).

79. Niell, C. M. & Stryker, M. P. Highly selective receptive fields in mouse visual cortex. *Journal of Neuroscience* 28, 7520–7536 (2008).

80. Stroud, A. C., Ledue, E. E. & Crowder, N. A. Orientation specificity of contrast adaptation in mouse primary visual cortex. *J Neurophysiol* 108, 1381–1391 (2012).

81. LeDue, E. E., King, J. L., Stover, K. R. & Crowder, N. A. Spatiotemporal specificity of contrast adaptation in mouse primary visual cortex. *Front Neural Circuits* 7, 1–11 (2013).

82. Carter, M. E. & De Lecea, L. Optogenetic investigation of neural circuits in vivo. *Trends Mol Med* 17, 197–206 (2011).

83. Boyden, E. S., Zhang, F., Bamberg, E., Nagel, G. & Deisseroth, K. Millisecond-timescale, genetically targeted optical control of neural activity. *Nat Neurosci* 8, 1263–1268 (2005).

84. Guru, A., Post, R. J., Ho, Y. Y. & Warden, M. R. Making sense of optogenetics. *International Journal of Neuropsychopharmacology* vol. 18 1–8 Preprint at https://doi.org/10.1093/ijnp/pyv079 (2015).

85. Wood, K. C., Blackwell, J. M. & Geffen, M. N. Cortical inhibitory interneurons control sensory processing. *Curr Opin Neurobiol* 46, 200–207 (2017).

86. Ji, X. Y. *et al.* Thalamocortical Innervation Pattern in Mouse Auditory and Visual Cortex: Laminar and Cell-Type Specificity. *Cerebral Cortex* 26, 2612–2625 (2016).

87. Adesnik, H. Synaptic Mechanisms of Feature Coding in the Visual Cortex of Awake Mice. *Neuron* 95, 1147-1159.e4 (2017).

88. Niell, C. M. & Scanziani, M. How Cortical Circuits Implement Cortical Computations: Mouse Visual Cortex as a Model. *Annu Rev Neurosci* 44, 517–546 (2021).

89. Karnani, M. M. *et al.* Cooperative Subnetworks of Molecularly Similar Interneurons in Mouse Neocortex. *Neuron* 90, 86–100 (2016).

90. Pfeffer, C. K., Xue, M., He, M., Huang, Z. J. & Scanziani, M. Inhibition of inhibition in visual cortex: The logic of connections between molecularly distinct interneurons. *Nat Neurosci* 16, 1068–1076 (2013).

91. Xu, X., Roby, K. D. & Callaway, E. M. Immunochemical characterization of inhibitory mouse cortical neurons: Three chemically distinct classes of inhibitory cells. *Journal of Comparative Neurology* 518, 389–404 (2010).

92. Gentet, L. J. *et al.* Unique functional properties of somatostatin-expressing GABAergic neurons in mouse barrel cortex. *Nat Neurosci* 15, 607–612 (2012).

93. Royer, S. *et al.* Control of timing, rate and bursts of hippocampal place cells by dendritic and somatic inhibition. *Nat Neurosci* 15, 769–775 (2012).

94. Kapfer, C., Glickfeld, L. L., Atallah, B. V & Scanziani, M. Supralinear increase of recurrent inhibition during sparse activity in the somatosensory cortex. *Nat Neurosci* 10, 743–753 (2007).

95. Silberberg, G. & Markram, H. Disynaptic Inhibition between Neocortical Pyramidal Cells Mediated by Martinotti Cells. *Neuron* 53, 735–746 (2007).

96. Silberberg, G. Polysynaptic subcircuits in the neocortex: spatial and temporal diversity. *Current Opinion in Neurobiology* vol. 18 332–337 Preprint at https://doi.org/10.1016/j.conb.2008.08.009 (2008).

97. Bortone, D. S., Olsen, S. R. & Scanziani, M. Translaminar inhibitory cells recruited by layer 6 corticothalamic neurons suppress visual cortex. *Neuron* 82, 474–485 (2014).

98. Karnani, M. M. *et al.* Opening Holes in the Blanket of Inhibition: Localized Lateral Disinhibition by VIP Interneurons. *J Neurosci* 36, 3471–80 (2016).

99. Atallah, B. V, Bruns, W., Carandini, M. & Scanziani, M. Parvalbumin-Expressing Interneurons Linearly Transform Cortical Responses to Visual Stimuli. *Neuron* 73, 159–170 (2012).

100. Lee, S. H. *et al.* Activation of specific interneurons improves V1 feature selectivity and visual perception. *Nature* 488, 379–383 (2012).

101. Wilson, N. R., Runyan, C. A., Wang, F. L. & Sur, M. Division and subtraction by distinct cortical inhibitory networks in vivo. *Nature* 488, 343–348 (2012).

102. Lee, S.-H., Kwan, A. C. & Dan, Y. Interneuron subtypes and orientation tuning. *Nature* 508, E1-2 (2014).

103. Shapiro, J. T., Gosselin, E. A. R., Michaud, N. M. & Crowder, N. A. Activating parvalbumin-expressing interneurons produces iceberg effects in mouse primary visual cortex neurons. *Neuroscience Letters136804* 786, (2022).

104. Atallah, B. V, Scanziani, M. & Carandini, M. Atallah et al. reply. *Nature* vol. 508 Preprint at https://doi.org/10.1038/nature13129 (2014).

105. El-Boustani, S. & Sur, M. Response-dependent dynamics of cell-specific inhibition in cortical networks in vivo. *Nat Commun* 5, 1–14 (2014).

106. Shapiro, J. T., Michaud, N. M., King, J. L. & Crowder, N. A. Optogenetic Activation of Interneuron Subtypes Modulates Visual Contrast Responses of Mouse V1 Neurons. *Cerebral Cortex* 32, 1110–1124 (2022).

107. Adesnik, H., Bruns, W., Taniguchi, H., Huang, J. Z. & Scanziani, M. A neural circuit for spatial summation in visual cortex. *Nature* 490, 226–230 (2012).

108. Keller, A. J. *et al.* A Disinhibitory Circuit for Contextual Modulation in Primary Visual Cortex. *Neuron* 108, 1181-1193.e8 (2020).

109. Ma, W. *et al.* Visual representations by cortical somatostatin inhibitory neurons--selective but with weak and delayed responses. *J Neurosci* 30, 14371–9 (2010).

110. Xue, M., Atallah, B. V & Scanziani, M. Equalizing excitation-inhibition ratios across visual cortical neurons. *Nature* 511, 596–600 (2014).

111. Fu, Y. *et al.* A cortical circuit for gain control by behavioral state. *Cell* 156, 1139–1152 (2014).

112. Zhang, S. *et al.* Selective attention. Long-range and local circuits for top-down modulation of visual cortex processing. *Science* 345, 660–5 (2014).

113. Jackson, J., Ayzenshtat, I., Karnani, M. M. & Yuste, R. VIP+ interneurons control neocortical activity across brain states. *J Neurophysiol* 115, 3008–3017 (2016).

114. Marder, E. & Bucher, D. Central pattern generators and the control of rhythmic movements. *Current Biology* 11, 986–996 (2001).

115. Bucher, D., Haspel, G., Golowasch, J. & Nadim, F. Central Pattern Generators. in *eLS2* 1–12 (Wiley, 2015). doi:10.1002/9780470015902.a0000032.pub2.

116. Marder, E. & Caiabrese, R. L. Principles of Rhythmic Motor Pattern Generation. *Physiology Review* 76, 687–717 (1996).

117. Satterlie, R. A. Reciprocal Inhibition and Postinhibitory Rebound Produce Reverberation in a Locomotor Pattern Generator. *Science (1979)* 229, 402–404 (1985).

118. Wahl-Schott, C. & Biel, M. HCN channels: Structure, cellular regulation and physiological function. *Cellular and Molecular Life Sciences* vol. 66 470–494 Preprint at https://doi.org/10.1007/s00018-008-8525-0 (2009).

119. Mccormick, D. A. & Bal, T. Sleep and arousal: thalamocortical mechanisms. *Annual Reviews of Neuroscience* 20, 185–215 (1997).

120. Huguenard, J. R. & McCormick, D. A. Thalamic synchrony and dynamic regulation of global forebrain oscillations. *Trends Neurosci* 30, 350–356 (2007).

121. Adhikari, M. H., Quilichini, P. P., Roy, D., Jirsa, V. & Bernard, C. Brain State Dependent Postinhibitory Rebound in Entorhinal Cortex Interneurons. *Journal of Neuroscience* 32, 6501–6510 (2012).

122. Bertrand, S. & Cazalets, J.-R. Postinhibitory rebound during locomotor-like activity in neonatal rat motoneurons in vitro. *J Neurophysiol* 79, 342–351 (1998).

123. Bal, T., von Krosigk, M. & McCormick, D. A. Role of the ferret perigeniculate nucleus in the generation of synchronized oscillations in vitro. *J Physiol* 483, 665–85 (1995).

124. Aizenman, C. D. & Linden, D. J. Regulation of the Rebound Depolarization and Spontaneous Firing Patterns of Deep Nuclear Neurons in Slices of Rat Cerebellum. *J Neurophysiol* 82, 1697–1709 (1999).

125. Ascoli, G. A., Gasparini, S., Medinilla, V. & Migliore, M. Local control of postinhibitory rebound spiking in CA1 pyramidal neuron dendrites. *Journal of Neuroscience* 30, 6434–6442 (2010).

126. Angstadt, J. D., Grassmann, J. L., Theriault, K. M. & Levasseur, S. M. Mechanisms of postinhibitory rebound and its modulation by serotonin in excitatory swim motor neurons of the medicinal leech. *J Comp Physiol A Neuroethol Sens Neural Behav Physiol* 191, 715–732 (2005).

127. Barrio, L. C., Araque, A. & Buño, W. Participation of voltage-gated conductances on the response succeeding inhibitory synaptic potentials in the crayfish slowly adapting stretch receptor neuron. *J Neurophysiol* 72, 1140–1151 (1994).

128. Felix, R. A., Fridberger, A., Leijon, S., Berrebi, A. S. & Magnusson, A. K. Sound rhythms are encoded by postinhibitory rebound spiking in the superior paraolivary nucleus. *Journal of Neuroscience* 31, 12566–12578 (2011).

129. Ferrante, M., Shay, C. F., Tsuno, Y., Chapman, G. W. & Hasselmo, M. E. Post-inhibitory rebound spikes in rat medial entorhinal layer II/III principal cells: In vivo, in vitro, and computational modeling characterization. *Cerebral Cortex* 27, 2111–2125 (2017).

130. Sun, H. & Wu, S. H. Physiological characteristics of postinhibitory rebound depolarization in neurons of the rat's dorsal cortex of the inferior colliculus studied in vitro. *Brain Res* 1226, 70–81 (2008).

131. Sun, H. *et al.* Developmentally Regulated Rebound Depolarization Enhances Spike Timing Precision in Auditory Midbrain Neurons. *Front Cell Neurosci* 14, 1–11 (2020).

132. Zheng, N. & Raman, I. M. Prolonged postinhibitory rebound firing in the cerebellar nuclei mediated by group I metabotropic glutamate receptor potentiation of l-type calcium currents. *Journal of Neuroscience* 31, 10283–10292 (2011).

133. Benarroch, E. E. HCN channels: function and clinical implications. *Neurology* 80, 304–310 (2013).

134. Perez-Reyes, E. Molecular physiology of low-voltage-activated t-type calcium channels. *Physiol Rev* 83, 117–61 (2003).

135. Tadayonnejad, R., Mehaffey, W. H., Anderson, D. & Turner, R. W. Reliability of triggering postinhibitory rebound bursts in deep cerebellar neurons. *Channels* 3, 149–155 (2009).

136. Berman, N. J., Douglas, R. J., Martin, K. A. C. & Whitteridge, D. Mechanisms of inhibition in cat visual cortex. *Journal of Physiology* 440, 697–722 (1991).

137. Douglas, R. J. & Martin, K. A. C. A functional microcircuit for cat visual cortex. *Journal of Physiology* 440, 735–769 (1991).

138. Grenier, F., Timofeev, I. & Steriade, M. Leading role of thalamic over cortical neurons during postinhibitory rebound excitation. *Proceedings of the National Academy of Sciences* 95, 13929–13934 (1998).

139. Alvĩa, K., Walter, J. T., Kohn, A., Ellis-Davies, G. & Khodakhah, K. Questioning the role of rebound firing in the cerebellum. *Nat Neurosci* 11, 1256–1258 (2008).

140. Funayama, K. *et al.* Neocortical rebound depolarization enhances visual perception. *PLoS Biol* 13, 1–25 (2015).

141. Kulesza, R. J., Kadner, A. & Berrebi, A. S. Distinct roles for glycine and GABA in shaping the response properties of neurons in the superior paraolivary nucleus of the rat. *J Neurophysiol* 97, 1610–1620 (2007).

142. Rajaram, E. *et al.* Slow nmda-mediated excitation accelerates offset-response latencies generated via a postinhibitory rebound mechanism. *eNeuro* 6, (2019).

143. Chang, M. *et al.* Brief activation of GABAergic interneurons initiates the transition to ictal events through post-inhibitory rebound excitation. *Neurobiol Dis* 109, 102–116 (2018).

144. Chuong, A. S. *et al.* Noninvasive optical inhibition with a red-shifted microbial rhodopsin. *Nat Neurosci* 17, 1123–1129 (2014).

145. Edgerton, J. R. & Jaeger, D. Optogenetic activation of nigral inhibitory inputs to motor thalamus in the mouse reveals classic inhibition with little potential for rebound activation. *Front Cell Neurosci* 8, (2014).

146. Jin, M. & Glickfeld, L. L. Mouse Higher Visual Areas Provide Both Distributed and Specialized Contributions to Visually Guided Behaviors. *Current Biology* 30, 4682-4692.e7 (2020).

147. Li, N. *et al.* Spatiotemporal constraints on optogenetic inactivation in cortical circuits. *Elife* 8, 1–31 (2019).

148. Madisen, L. *et al.* A toolbox of Cre-dependent optogenetic transgenic mice for light-induced activation and silencing. *Nat Neurosci* 15, 793–802 (2012).

149. Lado, W. E., Xu, X. & Hablitz, J. J. Modulation of epileptiform activity by three subgroups of GABAergic interneurons in mouse somatosensory cortex. *Epilepsy Research* 183, (2022).

150. Mahn, M., Prigge, M., Ron, S., Levy, R. & Yizhar, O. Biophysical constraints of optogenetic inhibition at presynaptic terminals. *Nat Neurosci* 19, 554–556 (2016).

151. Stark, E. *et al.* Inhibition-Induced theta resonance in cortical circuits. *Neuron* 80, 1263–1276 (2013).

152. Tsunematsu, T. *et al.* Acute optogenetic silencing of orexin/hypocretin neurons induces slow-wave sleep in mice. *Journal of Neuroscience* 31, 10529–10539 (2011).

153. Takeuchi, T. *et al.* Locus coeruleus and dopaminergic consolidation of everyday memory. *Nature* 537, 357–362 (2016).

154. Tønnesen, J., Sørensen Andreas T, Deisseroth, K., Lundberg, C. & Kokaia, M. Optogenetic control of epileptiform activity. *Proceedings of the National Academy of Sciences* 106, 12162–12167 (2009).

155. Arrenberg, A. B., Del Bene, F. & Baier, H. Optical control of zebrafish behavior with halorhodopsin. *Proc Natl Acad Sci U S A* 106, 17968–17973 (2009).

156. Witter, L., Canto, C. B., Hoogland, T. M., de Gruijl, J. R. & De Zeeuw, C. I. Strength and timing of motor responses mediated by rebound firing in the cerebellar nuclei after Purkinje cell activation. *Front Neural Circuits* 7, 1–14 (2013).

157. Ayzenshtat, I., Karnani, M. M., Jackson, J. & Yuste, R. Cortical control of spatial resolution by VIP+ interneurons. *Journal of Neuroscience* 36, 11498–11509 (2016).

158. Sessolo, M. *et al.* Parvalbumin-positive inhibitory interneurons oppose propagation but favor generation of focal epileptiform activity. *Journal of Neuroscience* 35, 9544–9557 (2015).

159. Villalobos, C. A. & Basso, M. A. Optogenetic activation of the inhibitory nigro-collicular circuit evokes contralateral orienting movements in mice. *Cell Rep* 39, 1–14 (2022).

160. Magloire, V., Mercier, M. S., Kullmann, D. M. & Pavlov, I. GABAergic Interneurons in Seizures: Investigating Causality With Optogenetics. *The Neuroscientist* 25, 344–358 (2019).

161. Lado, W. E., Xu, X. & Hablitz, J. J. Modulation of epileptiform activity by three subgroups of GABAergic interneurons in mouse somatosensory cortex. *Epilepsy Res* 183, (2022).

162. Mattis, J. *et al.* Principles for applying optogenetic tools derived from direct comparative analysis of microbial opsins. *Nat Methods* 9, 159–172 (2012).

163. Paxinos, G. & Franklin, K. B. J. *Paxinos and Franklin's The Mouse Brain in Stereotaxic Coordinates* . (Academic Press, 2019).

164. Wang, Q. & Burkhalter, A. Area map of mouse visual cortex. *J Comp Neurol* 502, 339–57 (2007).

165. Stujenske, J. M., Spellman, T. & Gordon, J. A. Modeling the Spatiotemporal Dynamics of Light and Heat Propagation for In Vivo Optogenetics. *Cell Rep* 12, 525–34 (2015).

166. Asrican, B. *et al.* Next-generation transgenic mice for optogenetic analysis of neural circuits. *Front Neural Circuits* 7, 160 (2013).

167. King, J. L., Lowe, M. P., Stover, K. R., Wong, A. A. & Crowder, N. A. Adaptive Processes in Thalamus and Cortex Revealed by Silencing of Primary Visual Cortex during Contrast Adaptation. *Current Biology* 26, 1295–300 (2016).

168. Ledue, E. E., Zou, M. Y. & Crowder, N. A. Spatiotemporal tuning in mouse primary visual cortex. *Neurosci Lett* 528, 165–9 (2012).

169. King, J. L., Lowe, M. P. & Crowder, N. A. Contrast adaptation is spatial frequency specific in mouse primary visual cortex. *Neuroscience* 310, 198–205 (2015).

170. Johnson, S. M. & Getting, P. A. Electrophysiological properties of neurons within the nucleus ambiguus of adult guinea pigs. *J Neurophysiol* 66, 744–61 (1991).

171. Catterall, W. A. Cellular and molecular biology of voltage-gated sodium channels. *Physiol Rev* 72, S15-48 (1992).

172. Benarroch, E. E. GABAB receptors: structure, functions, and clinical implications. *Neurology* 78, 578–84 (2012).

173. Hallworth, N. E. & Bevan, M. D. Globus pallidus neurons dynamically regulate the activity pattern of subthalamic nucleus neurons through the frequency-dependent activation of postsynaptic GABAA and GABAB receptors. *Journal of Neuroscience* 25, 6304–6315 (2005).

174. Watanabe, M., Maemura, K., Kanbara, K., Tamayama, T. & Hayasaki, H. GABA and GABA receptors in the central nervous system and other organs. *Int Rev Cytol* 213, 1–47 (2002).

175. Kawaguchi, S. & Hirano, T. Suppression of inhibitory synaptic potentiation by presynaptic activity through postsynaptic GABA(B) receptors in a Purkinje neuron. *Neuron* 27, 339–47 (2000).

176. Carandini, M. Visual cortex: Fatigue and adaptation. *Current Biology* 10, R605-7 (2000).

177. Sanchez-Vives, M. V, Nowak, L. G. & McCormick, D. A. Cellular Mechanisms of Long-Lasting Adaptation in Visual Cortical Neurons In Vitro. *The Journal of Neuroscience* 20, 4286–4299 (2000).

178. Sanchez-Vives, M. V, Nowak, L. G. & McCormick, D. A. Membrane mechanisms underlying contrast adaptation in cat area 17 in vivo. *The Journal of Neuroscience* 20, 4267–85 (2000).

179. Alabi, A. A. & Tsien, R. W. Synaptic Vesicle Pools and Dynamics. *Cold Spring Harb Perspect Biol* 4, a013680–a013680 (2012).

180. Zhao, S. *et al.* Cell type-specific channelrhodopsin-2 transgenic mice for optogenetic dissection of neural circuitry function. *Nat Methods* 8, 745–755 (2011).

181. Safari, M. S., Mirnajafi-Zadeh, J., Hioki, H. & Tsumoto, T. Parvalbumin-expressing interneurons can act solo while somatostatin-expressing interneurons act in chorus in most cases on cortical pyramidal cells. *Sci Rep* 7, (2017).

182. Bock, D. D. *et al.* Network anatomy and in vivo physiology of visual cortical neurons. *Nature* 471, 177–82 (2011).

183. Hofer, S. B. *et al.* Differential connectivity and response dynamics of excitatory and inhibitory neurons in visual cortex. *Nat Neurosci* 14, 1045–52 (2011).

184. Packer, A. M. & Yuste, R. Dense, unspecific connectivity of neocortical parvalbumin-positive interneurons: a canonical microcircuit for inhibition? *The Journal of Neuroscience* 31, 13260–71 (2011).

185. Scholl, B., Pattadkal, J. J., Dilly, G. A., Priebe, N. J. & Zemelman, B. V. Local Integration Accounts for Weak Selectivity of Mouse Neocortical Parvalbumin Interneurons. *Neuron* 87, 424–36 (2015).

186. Wilson, D. E. *et al.* GABAergic Neurons in Ferret Visual Cortex Participate in Functionally Specific Networks. *Neuron* 93, 1058-1065.e4 (2017).

187. Iavarone, E. *et al.* Thalamic control of sensory processing and spindles in a biophysical somatosensory thalamoreticular circuit model of wakefulness and sleep. *Cell Rep* 42, 112200 (2023).

188. McCormick, D. A. & Contreras, D. On the cellular and network bases of epileptic seizures. *Annu Rev Physiol* 63, 815–46 (2001).

189. Turrigiano, G. Too many cooks? Intrinsic and synaptic homeostatic mechanisms in cortical circuit refinement. *Annu Rev Neurosci* 34, 89–103 (2011).